Cell crowding induces TRPV4 inhibition and its relocation to plasma membranes, implicating pro-invasive cell volume reduction mechanotransduction pathway

Xiangning Bu[1], Nathanael Ashby[1], Teresa Vitali[1], Sulgi Lee[1], Ananya Gottumukkala[1,2], Kangsun Yun[1], Sana Tabbara[3,†], Patricia Latham[3], Christine Teal[4], Inhee Chung[1,5*]

Affiliations:

1 Department of Anatomy and Cell Biology, School of Medicine and Health Sciences, George Washington University, Washington, DC, USA

2 Thomas Jefferson High School for Science and Technology, Alexandria, VA, USA

3 Department of Pathology, George Washington Medical Faculty Associates, Washington, DC, USA

4 Department of Surgery, George Washington Medical Faculty Associates, Washington, DC, USA

5 Department of Biomedical Engineering, GW School of Engineering and Applied Science, George Washington University, Washington, DC, USA

† Current address: Department of Pathology, H. Lee Moffitt Cancer Center and Department of Oncologic Sciences, University of South Florida Morsani College of Medicine, Tampa, FL, USA

* Correspondence to: inheec@gwu.edu

Abstract

Cell crowding is a common microenvironmental factor that affects various disease processes, but its impact on cell invasiveness into surrounding tissues is not well understood. This study investigates the biomechanical changes induced by cell crowding, focusing on pro-invasive cell volume reduction in ductal carcinoma in situ (DCIS) cells. DCIS is a non-invasive form of breast cancer characterized by abnormal cell growth confined within the breast duct. While DCIS can undergo invasive transition, it is unclear which DCIS cells are predisposed to this transition. We discovered that cell crowding enhanced the invasiveness of high-grade DCIS cells, which experienced significant cell volume reduction compared to hyperplasia-mimicking or normal cells. Mass spectrometry analyses revealed that cell crowding relocated ion channels, including TRPV4, a calcium-permeant ion channel, to the plasma membrane selectively in high-grade DCIS cells but not in less aggressive or normal cells. Cell crowding inhibited TRPV4 activity in high-grade DCIS cells, decreasing intracellular calcium levels and reducing cell volume. This inhibition also triggered the relocation of TRPV4 to the plasma membrane, effectively priming the inactive channel for activation and mitigating the calcium loss caused by crowding-induced inhibition. Analyses of patient-derived breast cancer tissues validated that TRPV4 is selectively associated with the plasma membrane in high-grade DCIS but not in lower-grade DCIS or less aggressive pathologies. The extent of plasma membrane TRPV4 association scaled with cell volume reduction and increased cell invasiveness and motility, suggesting its utility as an active pro-invasive mechanotransduction pathway indicator. Additionally, hyperosmotic conditions and pharmacologic TRPV4 inhibition mimicked the pro-invasive volume reduction observed under cell crowding, while TRPV4 activation reversed this effect by inducing cell volume increase. Silencing the TRPV4 gene via shRNA diminished the mechanotransduction capability of high-grade DCIS cells, as demonstrated by reduced intracellular calcium depletion, attenuated cell volume reduction, and decreased motility. In summary, this study uncovers a previously unrecognized pro-invasive mechanotransduction pathway initiated by cell crowding, which is specific to high-

grade DCIS cells, revealing a potential biomarker for identifying DCIS patients at high risk of invasive transition.

Introduction

The complex interplay between cellular mechanics and invasive behaviors is crucial to understanding various physiological and pathological processes, such as wound healing[1] and disease progression[2,3]. Numerous studies show that these processes are mediated by mechanotransduction, whereby cells translate mechanical stimuli into cellular activity[2,4-6]. While mechanotransduction is traditionally studied concerning fluid stress[7,8], matrix stiffness[4,9], and other biomechanical changes such as osmotic stress[10,11], the role of cell crowding, characterized by increased cell density and spatial constraints, is relatively less explored. A recent report shows that cell crowding plays a role in facilitating wound closure and repair by enhancing cell proliferation[12]. As tissues develop, repair, or undergo pathological transformation, cell crowding becomes common[13,14]. This challenges individual cells, forcing them to perceive and respond to the mechanical constraints of a crowded environment. Our study used human breast cell line model systems to describe a novel mechanotransduction pathway triggered by cell crowding that induces invasiveness into surrounding tissues. Interestingly, this pathway exhibited unique selectivity, as it specifically associated with a type of non-invasive cancer pathology and was not present in lower-grade or less aggressive pathologies. This suggests that not all cells possess the ability to translate mechanical stimuli, such as cell crowding, into cell invasiveness.

To assess the role of cell crowding in cell invasiveness, we chose in vitro cell lines linked to different pathological states that reflect cell crowding conditions in vivo, including atypical ductal hyperplasia (ADH)[15] and ductal carcinoma in situ (DCIS)[16-18]. ADH is an intraductal clonal epithelial cell proliferative lesion[18] and represents an intermediate step between normal breast tissue and in situ carcinomas[19-21]. ADH is associated with high risk as it is reported that an ADH

diagnosis is associated with a five-fold increased risk of breast cancer[15]. DCIS is non-invasive form of cancer characterized by proliferating malignant epithelial cells[16-18]. Unlike ADH, DCIS is considered a precursor to invasive breast cancer[22]. However, the mechanism of how DCIS transitions to invasive cancer is not well understood and therefore, there is currently no reliable and robust method to differentiate which DCIS cells are at high risk of becoming invasive[23,24].

Both ADH and DCIS conditions can potentially expose cells to crowding in vivo. However, how ADH and DCIS cells respond to such changes in cell density remains unknown. Our study revealed that cell crowding selectively triggered a pro-invasive mechanotransduction program in a specific type of DCIS cell line associated with high-grade comedo-type pathology[25,26]. The mechanotransduction program induced by cell crowding involved the inhibition of ion channels, such as transient receptor potential vanilloid 4 (TRPV4)[27], a calcium-permeable ion channel, as identified from our mass spectrometry assay. This inhibition prompted the relocation of TRPV4 and other ion channels to the plasma membrane, leading to decreased intracellular calcium levels, subsequent induction of reduced cell volume and cortical stiffening, thereby promoting cell invasiveness and motility.

Results

Cell Crowding Enhances Invasiveness in High-Grade DCIS Cells. Cell crowding reflects a common condition in tumor microenvironments for ADH and DCIS, arising from aberrant cell proliferation within spatially constrained intraductal spaces. We examined the influence of this prevalent environmental factor on the invasiveness of these cells in vitro. To conduct this investigation, we assembled a panel of cell lines derived from the normal breast epithelial cell line MCF10A, including its H-RAS mutation-driven derivatives associated with various pathologies[28]: MCF10AT1, MCF10DCIS.com, and invasive cells MCF10CA1a. MCF10AT1 resembles ADH[15], MCF10DCIS.com mimics high-grade DCIS[26], and MCF10CA1a represents a malignant invasive

cancer that was observed to form metastatic lesions in a mouse xenograft[29]. The current classification of DCIS relies on histological factors such as cell growth patterns and cytonuclear features[30,31]. Comedo-DCIS is a histologic subtype, which is characterized by apoptotic cell death, representing a high-grade DCIS with higher invasive potential than those of lower-grades[25]. MCF10DCIS.com forms comedo-type DCIS lesions that can spontaneously transition to invasive cancer when xenografted[26].

To compare cell invasiveness under normal cell density and cell crowding conditions in vitro, we opted for a modified 2D matrix degradation assay. This approach allowed us to quantify overall cell invasiveness by normalizing it with the total cell number, thereby accounting for differences in cell densities. We chose this method over transwell, 3D Matrigel, or spheroid assays, where quantifying cell invasiveness as a function of cell density is challenging. By modifying an existing collagen-crosslinked polyacrylamide hydrogel matrix-based invasion assay[32-34], we could determine the invasive cell fraction out of the total cell population by fluorescence imaging of the invasion gel bed and cell nuclei through a low magnification (4X) imaging (**Fig. 1A**; for a detailed procedure, see **Suppl. Fig. 1**) when cells were at normal density versus under cell crowding conditions.

We observed alterations in live cell morphology and invasiveness as they progressed from normal density (ND: 40-70%) to full confluence (100%) and beyond. Our goal was to determine a distinct time window, termed overconfluence (OC), where cell crowding-induced changes level off. The OC time window was achieved as cells cultured for an additional 5-10 days after reaching 100% confluence, with the growth medium replaced twice per day to prevent acidification. We confirmed that the cells remained largely viable under crowding conditions, with minimal cell death (~1.58%) similar to that observed in ND cells (~0.85%). (**Suppl. Fig. 2A-B**). The schematic of the timeline to achieve the OC conditions, and low-magnification (4X) bright-field images at different time

points from the ND to OC conditions are shown in **Suppl. Fig. 3A-B**. The time-dependent equilibration of cell invasiveness after the cells reached confluence is demonstrated in **Suppl. Fig. 3C-D** using our quantifiable collagen-crosslinked polyacrylamide hydrogel matrix-based invasion assay. Cell crowding mechanosensing significantly increased the invasive cell fraction of MCF10DCIS.com cells from ~24% (ND cells) to 59% (OC cells). The enhanced invasiveness of MCF10DCIS.com cells under cell crowding was largely reversible. When OC cells were reseeded at normal density for invasion assays, their invasive cell fraction decreased to approximately 15%, slightly lower ($p = 0.012$) than the initial value of around 24% (**Suppl. Fig. 3C, 3E**). In contrast, other cell types such as normal breast epithelial cells MCF10A and MCF10AT1, which mimic ADH conditions in vivo, did not display invasiveness in ND conditions or enhanced invasiveness in OC conditions, suggesting insensitivity to cell crowding (**Fig. 1B-C**).

The invasive cell fraction of ND MCF10CA1a cells was already ~80%, and the additional increase in invasiveness due to cell crowding was not readily discernible, with a slight increase to ~82% under crowded conditions. These data suggest a striking and selective mechanosensing effect of cell crowding on cell invasiveness in MCF10DCIS.com cells. To ensure that acidification did not affect the invasiveness of MCF10DCIS.com cells despite the frequent replacement of the cell growth medium, we incubated ND cells for two days with acidified medium from cultures of OC MCF10DCIS.com cells. We observed that medium acidity did not alter cell invasiveness (**Suppl. Fig. 3F**), reinforcing that the increased invasiveness under OC conditions was induced by cell crowding.

Cell crowding reduces cell volume and stiffens MCF10DCIS.com cells

As cells became crowded, we observed a reduction in cell size. Previous reports indicate an inverse relationship between cell volume and cortical stiffness[35,36], leading us to hypothesize that reduced cell volume would be accompanied by increased cortical stiffness. Research on glioma

cell invasion underscores the critical role of hydrodynamic cell volume changes in penetration into surroundings[37,38], suggesting that significant cell volume reduction facilitates cell invasion. Additionally, increased cortical stiffness is known to help cells overcome the physical barriers of the dense extracellular matrix[39,40]. We thus investigated whether cell crowding selectively induces pro-invasive cell volume reduction and cell stiffening in MCF10DCIS.com cells, thereby priming them for invasion.

To measure the cell volume of individual cells, we used confocal microscopy with a 60X oil immersion objective to obtain z-stack images of live or fixed cells stably expressing red fluorescent protein (RFP)[41]. Using a nanoindenter attached to the confocal microscope (**Suppl. Fig. 4A**), we extracted Young's modulus of live individual cells to assess changes in cortical stiffness. Cell crowding significantly reduced cell volume (**Fig. 2A, B**) and increased cortical stiffness (**Fig. 2C**) in both MCF10DCIS.com and MCF10A cells. However, the changes in volume and stiffness between ND and OC conditions were more pronounced in MCF10DCIS.com cells (**Suppl. Fig. 4B, C**). The cell crowding-induced alterations in cell volume and stiffness were negligible in MCF10AT1 cells (**Fig. 2A-C**). In MCF10CA1a cells, cell crowding led to an increase in stiffness, but a decrease in volume was not evident. This was expected because the cell volume was already too small to be accurately measured with the available resolution (**Fig. 2A-C**). The notable plasticity in cell volume and stiffness changes observed in MCF10DCIS.com cells in response to cell crowding potentially underscores the critical link between this plasticity and mechanosensitive increases in cell invasiveness. We assessed cell volume changes only as an effector event of cell crowding, without measuring cell stiffness, because cell volume reflects the mechanical properties of the entire cell, while Young’s modulus can vary depending on the location of indentations in the plasma membrane[42,43]. The observed cell volume changes by cell crowding (**Fig. 2A**) depended on the ND cell volume, as OC cell volumes under crowding conditions were comparable across all cells. Consequently, the ND cell volume and the volume

changes from ND to OC conditions exhibited an approximately linear relationship (R^2 ~ 0.97; **Suppl. Fig. 4D**). This finding suggests that the ND cell volume could serve as an indicator of relative cell volume plasticity.

To validate the pro-invasive nature of cell volume reduction in MCF10DCIS.com cells, we examined the effect of hyperosmotic cell volume reduction in ND cells using polyethylene glycol (PEG) 300 for 15 minutes. The cell volume reduction effects of this treatment were previously described[36,44]. PEG 300 effectively reduced ND MCF10DCIS.com cell volume in a dose-dependent manner, showing a greater reduction with 148.8 mOsmol/kg PEG 300 than with 74.4 mOsmol/kg PEG 300 (**Fig. 2D**). To assess the impact of PEG-induced cell volume reduction on cell invasiveness, we used collagen-crosslinked polyacrylamide hydrogel matrix-based invasion assay and exposed cells to 74.4 mOsmol/kg PEG 300 for 2 days. While treatment with 148.8 mOsmol/kg PEG 300 significantly reduced cell viability, cells treated with 74.4 mOsmol/kg PEG 300 remained viable for 2 days. Monitoring changes in cell invasiveness revealed that exposure of ND MCF10DCIS.com cells to 74.4 mOsmol/kg PEG 300 increased cell invasiveness (**Fig. 2E**), confirming the causal relationship between cell volume reduction and increased cell invasiveness.

Cell crowding induces TRPV4 relocation to plasma membrane in MCF10DCIS.com cells

Cell volume regulation typically depends on osmotic gradients that direct the movement of water across cell membranes[45]. This process is facilitated by ion flux modulation, which is controlled by ion channels and ion transporters located on the plasma membrane[46-49]. Notably, cells capable of achieving minimal cell volumes have been shown to successfully invade neighboring tissues[38]. Based on this, we speculated that the high cell volume plasticity observed in MCF10DCIS.com cells underlies their ability to penetrate the surrounding tissues. To achieve such efficient cell volume changes, cell crowding-induced mechanotransduction in MCF10DCIS.com cells may involve modulation of the number of ion channels or transporters on the plasma membrane.

To compare the plasma membrane-associated proteins between ND and OC conditions, we employed mass spectrometry and profiled those proteins using the streptavidin-pulled surface-biotinylated cell lysates. **Fig. 3A** shows the relative protein densities on the plasma membrane under ND (blue bars) and OC (red bars) conditions in MCF10DCIS.com cells. The figure highlights the top 25 proteins that exhibit over a 5-fold increase in expression on the plasma membrane in the OC condition compared to the ND condition (triangle plots). The gene names of these 25 proteins are presented in **Fig. 3A** (**Suppl. Table 1** provides the corresponding protein names along with the corresponding fold increases). Notably, TRPV4, a member of the transient receptor potential family of ion channels known for its mechanosensitive properties[50,51], showed a remarkable 153-fold increase in plasma membrane association in response to cell crowding, as illustrated in **Fig. 3A**. Additionally, we observed an increase in plasma membrane association of other ion channels, such as SCN11A (the alpha subunit of the voltage-gated sodium channel Nav1.9) with ~42-fold enrichment, and KCNN4 (the small-conductance calcium-activated potassium channel 3 SK3) showing ~6-fold increase, as shown in **Fig. 3A**. To evaluate the relative plasma membrane association of proteins under OC versus ND conditions, we performed a comparable mass spectrometry analysis of cell-surface biotinylated cell lysates for MCF10A, MCF10AT1, and MCF10CA1a cells. The top 25 gene/protein names showing increased plasma membrane associations in these cells are listed in **Suppl. Table 2**. Unlike in MCF10DCIS.com cases, there was no cell-crowding-induced relocation of ion channels and ion transporters to the plasma membrane in MCF10A and MCF10AT1 cells. However, in MCF10CA1a cells, ion transporters such as ATP2B4 showed a ~37-fold greater plasma membrane association under crowding conditions. This suggests that plasma membrane relocations of these ion channels and ion transporters in response to cell crowding selectively occurred in MCF10DCIS.com cells and, to an extent, in invasive ductal cancer MCF10CA1a cells.

TRPV4 plays a pivotal role in facilitating the passage of calcium ions (Ca2+) and is integral in detecting various forms of mechanical stresses, including temperature fluctuations and osmotic pressure[52,53]. Activation of TRPV4 channels elevates intracellular calcium levels, leading to cell volume increase via osmotic water influx[52,54]. Nav1.9 primarily contributes to the generation and propagation of action potentials in sensory neurons and is associated with various pain disorders[55-57]. SK3 channels are activated by elevated intracellular calcium levels and serve diverse physiological functions[58,59]. However, unlike TRPV4, Nav1.9 and SK3 channels are not generally classified as mechanosensors. Consequently, we focused on TRPV4, the mechanosensor channel displaying the most significant increase in the plasma membrane association under cell crowding conditions, to further investigate its role in promoting pro-invasive cell volume reduction in MCF10DCIS.com cells.

To confirm the selective plasma membrane association of TRPV4 in OC MCF10DCIS.com cells suggested by mass spectrometry results, we conducted immunoblots on surface-biotinylated lysates from all four cell types under both conditions. **Fig. 3B and Suppl. Fig. 5A** showed a notable association of TRPV4 with the plasma membrane in OC MCF10DCIS.com cells, which was significantly lower in ND cells. This association was not observed in MCF10A and MCF10AT1 cells under any conditions. Interestingly, in MCF10CA1a cells, TRPV4 associated with the plasma membrane under both conditions, with a slight increase in OC conditions. This increase suggests that these cells may also possess mechanosensing abilities, enabling them to respond to cell crowding. Additionally, immunoblots from whole-cell lysates showed consistent TRPV4 expression levels across different cell types and densities (**Fig. 3C**, **Suppl. Fig. 5B**), indicating that cell crowding influences ion channel trafficking without altering overall expression. This evidence strongly suggests that the relocation of TRPV4 to the plasma membrane is a mechanosensitive response to cell crowding.

To investigate the redistribution of TRPV4 in response to cell crowding, we performed IF imaging with confocal microscopy across all four cell types under both ND and OC conditions. The binding specificity of the TRPV4 antibody was confirmed through IF imaging (**Suppl. Fig. 6A**) and immunoblotting (**Suppl. Fig. 6B**) of MCF10DCIS.com cells treated with TRPV4 shRNA. As expected from the mass spectrometry results, TRPV4 (red) showed only modest localization to the plasma membrane in ND MCF10DCIS.com cells (**Fig. 3D**). In contrast, it was prominently associated with the plasma membrane in OC MCF10DCIS.com cells (**Fig. 3D**). In MCF10CA1a cells, TRPV4 was also associated with plasma membrane under ND conditions, but cell crowding also increased the association significantly as shown in MCF10DCIS.com cells. Plasma membrane associations were verified using the plasma membrane marker DiIC18(3), which we previously used to visualize the plasma membrane[60]. IF images showed that TRPV4 successfully colocalized with DiIC18(3) in OC MCF10DCIS.com and OC MCF10CA1a cells (**Suppl. Fig. 7A).** However, the non-interacting protein transferrin receptor (TfR; green) remained similarly distributed in the OC cells compared to the ND cells, indicating that the protein trafficking changes induced by cell crowding are specific to TRPV4 (**Fig. 3D**).

To investigate whether other ion channels identified through mass spectrometry and a well-known mechanosensory channel PIEZO1[61,62], exhibit similar behavior, we conducted IF imaging on ND and OC MCF10DCIS.com cells targeting KCNN4 and PIEZO1. Unfortunately, due to the absence of specific antibodies, we were unable to examine SCN11. In ND MCF10DCIS.com cells, KCNN4 was observed to be mostly cytosolic, while PIEZO1 was mildly but slightly more associated with the plasma membrane than TRPV4 under ND conditions. However, under OC conditions, both PIEZO1 and KCNN4 also relocated to the plasma membrane, albeit to a lesser extent than TRPV4 (**Suppl. Fig. 7B**). The varying degrees of plasma membrane association of PIEZO1 and KCNN4 are quantified using line analysis, as summarized in **Supple. Fig. 7C**.

As expected, in ND MCF10A, MCF10AT1, and MCF10DCIS.com cells, TRPV4 was modestly present at the plasma membrane but was predominantly intracellular, with notable enrichment in the nuclei (**Fig. 3D**). However, in OC MCF10DCIS.com cells, approximately 80% of TRPV4 was located in the plasma membrane based on line analysis (**Fig. 3E**). In contrast, in OC MCF10A and OC MCF10AT1 cells, TRPV4 remained mostly cytosolic but migrated out of the nuclei (**Fig. 3D**). TRPV4 association with the plasma membrane was observed in both ND and OC MCF10CA1a cells, with an observable increase under OC conditions, further confirming the immunoprecipitation results shown in **Fig. 3B**. Plasma membrane-associated TRPV4 was quantified using line analysis and plotted in **Fig. 3E**. Refer to **Suppl. Fig. 8A** for plots of the relative TRPV4 associations with the plasma membrane, cytosol, and nucleus between ND and OC conditions in all four cell types. These IF imaging results underscore the mechanosensitive plasma membrane relocation of ion channels in MCF10DCIS.com, and to an extent, in MCF10CA1a cells, contrasting with the observed insensitivity of MCF10A and MCF10AT1 cells to cell crowding.

To assess the relationship between cell crowding-induced cell volume reduction and plasma membrane relocation of TRPV4, we investigated whether hyperosmotic conditions, which reduce cell volume without cell crowding, would also result in TRPV4 relocation. We subjected ND cells to the same PEG 300 condition (74.4 mOsm/kg PEG for 15 minutes) used in **Fig. 2D** to induce cell volume reduction. In ND MCF10DCIS.com cells, such hyperosmotic cell volume reduction prompted significant plasma membrane relocation of TRPV4, a response not observed in MCF10A and MCF10AT1 cells, but seen in MCF10CA1a cells (**Fig. 3F**). Quantitative line analysis confirmed these findings by assessing the relative TRPV4 association with the plasma membrane (**Fig. 3G**; **Suppl. Fig. 8B** for plots of the relative TRPV4 association with the plasma membrane, cytosol, or nucleus). We confirmed that the seeming plasma membrane-associated TRPV4 under the hyperosmotic condition was indeed localized at the plasma membrane by using an extracellular domain antibody against TRPV4 in live MCF10DCIS.com cells, both untreated and

treated with 74.4 mOsm/Kg PEG 300. As expected, significant antibody binding was observed only in PEG 300-treated cells, where intracellular TRPV4 had relocated to the plasma membrane unlike in untreated live cells (**Suppl. Fig. 9A-B**). This finding underscores the relationship between mechanosensitive cell volume reduction and plasma membrane relocation of TRPV4, highlighting that both cell crowding and hyperosmotic stress lead to the same effect, particularly pronounced in MCF10DCIS.com cells.

We investigated whether TRPV4 relocation to the plasma membrane induced by cell crowding is reversible, as suggested by its impact on invasiveness (**Suppl. Fig. 3F**). To test this, previously OC MCF10DCIS.com cells were reseeded under ND conditions. We then assessed TRPV4 localization via immunofluorescence (IF) imaging to determine if most channels returned to the cytoplasm with only a modest localization at the plasma membrane, and could be relocated to the plasma membrane under mechanical stress, such as hyperosmotic conditions. Consistent with their initial ND state, reseeded ND MCF10DCIS.com cells displayed intracellular TRPV4 distribution (**Suppl. Fig. 10A**). Upon exposure to hyperosmotic stress (74.4 mOsm/Kg PEG300), TRPV4 was again relocated to the plasma membrane (**Suppl. Fig. 10B**). These findings, quantified through line analysis (**Suppl. Fig. 10C**), demonstrate that the mechanosensing response of MCF10DCIS.com cells is reversible.

Patient tissue analysis shows selective plasma membrane association of TRPV4 in high-grade DCIS cells

MCF10DCIS.com cells represent a basal cell model for high-grade DCIS cells driven by HRAS mutation[26,63]. However, the majority of patient-derived DCIS cells originate from the luminal cell population and lack the HRAS mutation[63]. Moreover, there are limited options for patient-derived DCIS cell line models that have not linked to well-defined pathology[64,65]. Thus, to seek generality of our finding about the selective association between plasma membrane relocation and high-

grade DCIS pathology, we examined 39 breast cancer patient tissue blocks to assess the selectivity in vivo. We designed an early-stage retrospective study by selecting various breast tissue pathologies that range from benign to invasive cancer. Those pathologies include usual ductal hyperplasia, papilloma, columnar changes, ADH, low- to high-grade DCIS, and invasive ductal carcinoma (IDC). We also incorporated normal regions for comparison. Hematoxylin and eosin (H&E) staining was used to visualize tissue sections from each patient, excluding samples with prior cancer diagnoses or drug treatments. In total, 97 regions of interest (ROIs) from H&E-stained sections of 39 patient tissue blocks were selected. Two pathologists independently assessed TRPV4 distribution patterns at the single-cell level in corresponding ROIs in the immunohistochemistry (IHC) images (**Fig. 3H**). A detailed methodology is described in the Methods section and more example images are shown in **Suppl. Fig. 11**. High-grade DCIS cells, as depicted in **Fig. 3H**, clearly demonstrated plasma membrane-associated TRPV4, a feature absent in lower-grade DCIS cells (intermediate- and low-grade). This distinction sets them apart not only from cells with ADH and benign pathologies but also from lower-grade DCIS cells. As demonstrated by the IF images in **Fig. 3D** for MCF10CA1a (invasive cell mimic), IDC cells exhibited notable plasma membrane TRPV4, suggesting that they possess a similar pro-invasive mechanotransduction capability to high-grade DCIS cells.

We found that the sensitivity and specificity for plasma membrane TRPV4 in high-grade DCIS cells were 0.75 ± 0.19 (15/20) and 0.98 ± 0.03 (61/62) respectively (95% confidence interval) (**Fig. 3I**). It is important to note that the specificity calculation excluded IDC cases. Notably, even in less aggressive pathologies, a significant amount of TRPV4 was localized in the nuclei, as shown for MCF10A and MCF10AT1 cells in the IF images in **Fig. 3D**. This underscores our interpretation from the in vitro results in **Fig. 3A-D** that increased plasma membrane association of TRPV4 in high-grade DCIS cells results from changes in protein localization through trafficking alterations, rather than differences in expression levels. These initial in vivo results clearly demonstrate the

selective and specific association of TRPV4 with the plasma membrane in high-grade DCIS cells. Notably, this association is absent in lower-grade DCIS, ADH, benign, and normal cells, thereby confirming our in vitro findings using MCF10A cell derivatives. These results suggest a potentially critical role for TRPV4 in the progression of high-grade DCIS.

Cell crowding inhibits ion channels and triggers their plasma membrane relocations

A calcium-permeant ion channel like TRPV4 is known to influence intracellular calcium dynamics[54]. While activation of TRPV4 typically elevates calcium levels and this potentially increases cell volume[66-68], the impact of its inhibition is less clear, given the multifaceted nature of calcium signaling in cell volume control[69]. This complexity is compounded by compensatory cellular mechanisms and the involvement of other ion channels in response to altered calcium homeostasis[46]. Considering these factors, we hypothesized that cell crowding might inhibit calcium-permeant ion channels that are constitutively active at the plasma membrane, including TRPV4, which would then lower intracellular calcium levels and subsequently reduce cell volume via osmotic water movement. To test this, we employed the Fluo-4 calcium assay[70] to compare relative intracellular calcium levels of MCF10DCIS.com cells between ND and confluent (Con) conditions through 4X confocal microscopy imaging with 488 nm excitation. For this calcium assay, we opted for confluent conditions instead of OC conditions to collect the Fluo-4 signal from confluent monolayers of MCF10DCIS cells, which demonstrates comparable cell-crowding induced TRPV4 relocation to the plasma membrane (**Suppl. Fig. 12A**) as observed in the OC condition. This choice was made because more than one layer of cells was occasionally observed in OC conditions, which would yield overestimation of crowding-dependent intracellular calcium levels. The intracellular Fluo-4 signal under Con conditions was significantly lower than that under ND conditions, as shown in the fluorescence images of ND versus Con cells in **Fig. 4A**. Time-dependent Fluo-4 images were acquired over 25 minutes. For ND cell images, the average Fluo-4 intensity values were calculated from 10-15 selected cells (highlighted in the white box in **Fig.**

4A). For Con cell images, intensity values were derived from all cells within the entire 50 μm by 50 μm field of view, as depicted in **Fig. 4A**. After background subtraction, the intensity values were plotted in **Fig. 4B**. The temporal Fluo-4 intensity profiles from both ND and Con cells remained largely constant over the measured 20-minute period. However, Con cells exhibited significantly lower Fluo-4 intensity compared to ND cells, indicating reduced intracellular calcium levels. Lower Fluo-4 intensity in Con cells than in ND cells was not due to limited Fluo-4 reagent in Con samples. Within cell clusters, cells experiencing crowding exhibited notably lower Fluo-4 levels compared to those at the periphery (**Suppl. Fig. 12B**), suggesting that cell crowding had resulted in a decrease in intracellular calcium levels, likely due to the mechanosensitive inhibition of calcium-permeable channels like TRPV4.

To investigate whether TRPV4 inhibition was involved in decreased intracellular calcium levels and subsequent relocation of TRPV4 to the plasma membrane, we employed TRPV4-specific pharmacological agents to alter TRPV4 activity and modulate calcium concentrations in ND MCF10DCIS.com cells without applying cell crowding conditions. To inhibit TRPV4 activity, we used TRPV4 inhibitor (GSK2193874; GSK219)[71] at 0.2 and 1 nM, which we confirmed to have insignificant effects on cell viability in both ND and OC conditions for two days (**Suppl. Fig. 13A**). GSK219 treatments immediately caused a modest dip in the Fluo-4 signal, or intracellular calcium level, followed by a recovery, indicating cellular homeostatic activity. **Fig. 4D** shows Fluo-4 images taken before and at the signal dip after applying 1 nM GSK219, where the dip in the Fluo-4 signal is not visually apparent. However, the temporal profile of Fluo-4 intensity in **Fig. 4E**, which corresponds to the time points marked in **Fig. 4D** (t_1: baseline and t_2: dip), clearly shows the dip at t_2, indicated by ΔCa (the vertical dashed line between the dip and baseline). This modest Fluo-4 dip at t_2 represents the inhibition of activity by GSK219 on a small population of constitutively active TRPV4 channels at the plasma membrane under ND conditions.

In Con cells, 1 nM GSK219 caused a smaller dip in Fluo-4 intensity compared to the one observed in ND cells, with no subsequent changes. This is likely due to fewer constitutively active TRPV4

at the plasma membrane in Con cells than in ND cells. **Fig. 4F** shows Fluo-4 images at the baseline and the dip, and **Fig. 4G** presents the temporal Fluo-4 intensity profile, highlighting the two time points. Indeed, the dip in Fluo-4 intensity induced by GSK219 was smaller for Con MCF10DCIS.com cells (mean ΔCa ~ -39 ± 9) than for ND cells (mean ΔCa ~ -49 ± 18), as illustrated in **Fig. 4H**. The dose-dependent (0.2 nM and 1 nM GSK219, labeled 219L and 219H) and cell density-dependent (ND and Con) Fluo-4 signal dips are summarized by the ΔCa values plotted in **Fig. 4H**, showing that the most significant TRPV4 inhibition occurred in ND MCF10DCIS.com cells treated with 1 nM GSK219. These findings suggest that a substantial portion of TRPV4 channels relocated to the plasma membrane under cell crowding was inactive, and some constitutively activeTRPV4 channels already present in the membrane became inactive as a result of cell crowding.

Administering a TRPV4 activator (GSK1016790A; GSK101)[72,73] immediately caused a notably greater spike in Fluo-4 signal in Con cells than in ND cells, evidencing that a large number of TRPV4 channels at the plasma membrane were inactive in Con cells. In Con cells, 0.2 pM GSK101 led to a large Fluo-4 signal spike with ΔCa ~ +2,348 ± 597, while in ND cells, ΔCa was just ~ +324 ± 130. This difference is depicted in the Fluo-4 images (**Fig. 4I** for ND and **Fig. 4K** for Con) and the time-dependent Fluo-4 intensity plots (**Fig. 4J** for ND and **Fig. 4L** for Con). The dose (101L and 101H representing 0.05 pM and 0.2 pM GSK101) and cell-density (ND and Con) dependent Fluo-4 signal spikes are summarized in the ΔCa values, as shown in **Fig. 4M**. The results show the significant GSK101 dose-responsive activation of previously inactive TRPV4 in Con MCF10DCIS.com cells, confirming that a large number of inactive TRPV4 channels at the plasma membrane were primed for activation in Con cell.

Based on the differing effects of GSK219 and GSK101 on immediate intracellular calcium responses, along with lower calcium levels in Con cells compared to ND cells, we hypothesized that cell crowding induces TRPV4 inhibition, leading to reduced intracellular calcium levels, which in turn triggers the relocation of TRPV4 to the plasma membrane as a compensatory mechanism. To test this hypothesis, we examined TRPV4 localization changes in response to GSK219 or

GSK101 in a dose-dependent manner in both ND and OC MCF10DCIS.com cells using IF imaging (**Fig. 4N** for higher GSK101/219 concentrations; **Suppl. Fig. 13B** for both concentrations). Indeed, treating ND cells with the TRPV4 inhibitor GSK219 for 1 hour resulted in significant dose-dependent TRPV4 relocation to the plasma membrane (~53 ± 7% at 0.2 nM and ~62 ± 7% at 1 nM), compared to control ND cells (~15 ± 6%), as shown by line analysis (**Fig. 4P**). These results indicate that TRPV4 inhibition induces its strategic relocation to the plasma membrane, priming it for rapid activation to counteract the effects of channel inhibition.

Confirming our observation of moderate Fluo-4 spikes induced by GSK101 in ND MCF10DCIS.com cells, which implies a small number of constitutively active TRPV4 channels (**Fig. 4J**), the plasma membrane-associated TRPV4 levels in ND cells remained largely unchanged following GSK101 treatment (**Fig. 4N, 4P**). However, in Con cells, where a large number of inactive TRPV4 channels are likely located at the plasma membrane, GSK101 treatment notably reduced plasma membrane-associated TRPV4 in a dose-dependent manner through internalization (**Fig. 4O, 4Q**), consistent with previous findings[65]. These data suggest that plasma membrane TRPV4 levels were largely regulated by the channel activity status. Specifically, channel activation led to the internalization of TRPV4, while channel inhibition promoted the relocation of TRPV4 to the plasma membrane. This relationship was approximately linear as shown in **Fig. 4R**, where the intracellular calcium differences compared to that of ND cells were negatively associated with plasma membrane fraction of TRPV4 (R^2 ~ 0.69).

Contrary to our expectation, GSK219 treatment in Con cells slightly reduced TRPV4 levels at the plasma membrane (**Fig. 4O, 4Q**). Moreover, higher doses of GSK219 increased nuclear TRPV4 levels in Con cells without affecting cytoplasmic levels (**Suppl. Fig. 13B**). These findings suggest that further TRPV4 inhibition under crowding conditions triggers a distinct trafficking alteration. Recent studies have implicated nuclear TRPV4 in regulating nuclear Ca^{2+} homeostasis and Ca^{2+}-regulated transcription[74]. In light of this study and our findings, TRPV4 may relocate to the nucleus as a compensatory mechanism to maintain nuclear calcium regulation. This relocation could

reflect an adaptive response to preserve calcium-dependent transcriptional programs or other nuclear processes essential for cell survival under mechanical stress.

Given the role of TRPV4 in osmoregulation[53,75] and its significant relocation to the plasma membrane under hyperosmotic conditions (~55% plasma membrane association by line analysis; **Fig. 3E, 4P**) in ND MCF10DCIS.com cells (~15% plasma membrane association by line analysis), we explored the potential involvement of TRPV4 inhibition during this relocation. Using the Fluo-4 assay, we observed an initial calcium spike following 74.4 mOsm/kg PEG 300 in ND MCF10DCIS.com cells due to osmotic water outflow, which was followed by a homeostatic relaxation aimed at restoring calcium levels (**Suppl. Fig. 14A**). This relaxation likely involved the inhibition of ion channels like TRPV4 and other ion transporters, followed by their relocations to the plasma membrane. Indeed, we confirmed the relocation of other ion channels that responded to cell crowding, including KCNN4 and PIEZO1, to the plasma membrane following the same PEG 300 treatment (**Suppl. Fig. 14B** for IF images and line analysis results). The data suggest that the increased association of TRPV4 with the plasma membrane under hyperosmotic stress may reflect an adaptive inhibition response to water outflow.

To investigate the role of TRPV4 in mechanotransduction, we used shRNA to silence TRPV4 gene expression, resulting in a ~50% reduction in TRPV4 protein levels (**Suppl. Fig. 6B**). We then assessed the effects of TRPV4 silencing on intracellular calcium levels in ND and Con conditions, as well as the immediate calcium response to hyperosmotic stress induced by 74.4 mOsm/Kg PEG 300. In ND cells, hyperosmotic stress triggered a significant calcium spike, as shown in the Fluo-4 image (middle; **Fig. 4S**) and time trace (blue; **Fig. 4T**). In contrast, TRPV4 silencing in ND cells led to a lower intracellular calcium level (left; **Fig. 4U**) and a reduced calcium spike in response to hyperosmotic stress (middle; **Fig. 4U**, and semi-transparent blue; **Fig. 4V**). Furthermore, the effect of TRPV4 silencing on intracellular calcium levels was less pronounced in Con cells (semi-transparent red; **Fig. 4V**) compared to the ND counterpart (semi-transparent blue; **Fig. 4V**). The relative intracellular calcium levels are summarized in **Fig. 4W**.

Notably, TRPV4 silencing significantly reduced the immediate calcium spike as summarized in **Fig. 4X**. This calcium spike was attributed to increased calcium concentration due to hyperosmotically reduced cell volume (**Suppl. Fig. 14A**). Thus, TRPV4 may play a critical role in mechanotransduction, enabling cells to sufficiently reduce their volume in response to mechanical stress (large volume plasticity). To further investigate this, we examined the effect of TRPV4 silencing on ND MCF10DCIS.com cell volume reduction in response to hyperosmotic stress. We indeed found that control ND cells underwent a 48% volume reduction in response to 74.4 mOsm/Kg PEG 300, whereas TRPV4-silenced cells only reduced their volume by 27% (**Fig. 4Y**). Notably, this reduced cell volume reduction in TRPV4-silenced cells is consistent with the idea that cell volume reduction-induced increased calcium concentration contributes to the calcium spike, reinforcing the concept that TRPV4 augments the ability of cells to mechanotransduce.

Cell crowding-induced inactive TRPV4 relocation to the plasma membrane indicates channel inhibition-mediated volume reduction and enhanced invasiveness and motility

To elucidate the relationships between TRPV4 inhibition, cell volume reduction, and invasiveness increase under cell crowding, we investigated the effects of TRPV4 inhibitors on these processes. We examined the effects of 2-day treatments with GSK101 and GSK219 on the cell volumes of ND and OC MCF10DCIS.com cells. This duration was chosen to correlate the treatments with changes in cell volume and invasiveness, as observed in response to cell crowding

Under ND conditions, activating TRPV4 with GSK101 (0.05 or 0.2 pM for 2 days), which led to only modest calcium spikes and largely unaltered TRPV4 distribution (**Fig. 4N**; **Suppl. Fig. 13B**), did not significantly change cell volume (**Fig. 5A**). Conversely, TRPV4 inhibition by GSK219 treatment (1 nM for 2 days) that induced greater calcium changes (dips rather than spikes) and a significant plasma membrane relocation of TRPV4, led to a noticeable cell volume reduction (**Fig. 5A**). 0.2 nM GSK219 treatment had a negligible impact on ND cell volume (**Fig. 5A**). The GSK219 effect in ND MCF10DCIS.com cell volume was similar to that observed under hyperosmotic conditions by 74.7 mOsm/Kg PEG 300 (**Fig. 5A**).

Under OC conditions, GSK101 triggered significant, dose-dependent calcium spikes, leading to corresponding increases in cell volume (**Fig. 5B**). In contrast, GSK219 had a minimal impact on intracellular calcium levels and did not alter TRPV4 distribution at the plasma membrane, resulting in a slight reduction in cell volume at 1 nM (**Fig. 5B**). Similarly, PEG 300 induced a small change in cell volume, comparable to the 1 nM GSK219 treatment (**Fig. 5B**). As expected, we observed a significant negative linear correlation between plasma membrane-associated TRPV4 (% PM TRPV4) and cell volume (R^2 ~ 0.59) (**Fig. 5C**). These findings (**Fig. 5A-B**) demonstrate that increased TRPV4 inhibition and subsequent intracellular calcium reduction in response to cell crowding are associated with decreased cell volume in MCF10DCIS.com cells.

We investigated the connections between TRPV4 activity, plasma membrane association, cell volume changes, and cell invasiveness. Using a collagen-crosslinked polyacrylamide hydrogel matrix-based invasion assay, we evaluated changes in invasiveness after 2-day treatments with GSK101 or GSK219. In ND MCF10DCIS.com cells, 0.2 pM GSK101 mildly suppressed cell invasiveness, while 0.05 pM GSK101 had no effect (**Fig. 5D**). In contrast, GSK219 increased the invasive cell fraction in a dose-dependent manner under ND conditions, mirroring changes in Fluo-4 signals and plasma membrane-associated TRPV4 (**Fig. 5D**). Under OC conditions, GSK101 increased cell volume and suppressed cell invasiveness dose-dependently (**Fig. 5E**). Conversely, GSK219 and PEG 300, which slightly reduced cell volume, increased cell invasiveness (**Fig. 5E**). Representative invasion images are shown in Suppl. Fig. 15A. These results establish a clear relationship between TRPV4 activity, plasma membrane-associated TRPV4, cell volume, and cell invasiveness. Notably, we observed a significant positive linear correlation between plasma membrane-associated TRPV4 and cell invasiveness (**Fig. 5F**; R^2 ~ 0.69) and a negative association between cell volume and cell invasiveness (**Fig. 5G**; R^2 ~ 0.89).

Cell invasiveness refers to the ability of cells to penetrate and move within their surrounding tissues or environments. As expected from the increased cortical stiffness of OC MCF10DCIS.com cells (**Fig. 2C**), we observed that OC MCF10DCIS.com cells underwent cytoskeletal rearrangements, including the increased formation of stress fibers (**Suppl. Fig. 15B**), which likely enhanced cell motility[75]. To assess how TRPV4 inhibition and activation, which reduced and increased cell volume, respectively, affected the motility of ND MCF10DCIS.com cells and the role of these motility changes on cell invasiveness, we conducted single-cell tracking experiments similar to single molecule tracking methods[60,76-80]. We utilized wheat germ agglutinin (WGA) as a nuclear marker, which stained the cell nucleus within 1 hour of incubation with cells. We then analyzed the diffusivity (*D*) and directionality (*v*) of single cell movements. We tracked overall single-cell trajectories for 3 hr with 1 min intervals, marking cell displacement over each interval in different colors, ranging from navy for the slowest to red for the fastest (**Fig. 5H**). Consistent with the trend in cell invasiveness, TRPV4 activation with 1 pM GSK101 significantly reduced single-cell movements, while inhibition with 0.2 nM GSK219 and 74.4 mOsm/kg PEG 300 notably increased these movements. Using the single-cell motility assay, we assessed TRPV4's role in increasing cell invasiveness through a mechanotransduction mechanism involving cell-volume reduction. Reducing TRPV4 expression (~50%) via shRNA diminished the cell volume reduction effect of mechanosensing. We predicted that shRNA would also attenuate the increased cell motility effect of mechanosensing in MCF10DCIS.com cells. Indeed, while shRNA (sh-ctrl; **Fig. 5H, 5I**) did not alter MCF10DCIS.com cell motility, it disabled mechanotransduction capability of the cells as there was no increase in *D* and *v* induced by hyperosmotic stress using 74.4 mOsm/Kg PEG 300 (sh-PEG; **Fig. 5H, 5I**). This result reinforces the critical role of TRPV4 in increasing cell invasiveness through mechanosensing activity inhibition-induced cell volume reduction.

Interestingly, while GSK219 and hyperosmotic conditions promoted increased cell movement (*D*; **Fig. 5I**), they also reduced cell directionality (*v*; **Fig. 5I**). This reduction in directionality suggests that while the cells become more mobile, their movements are less targeted, potentially indicating a more random or exploratory behavior under mechanical stress. Remarkably, cell movement increased in proportion to the amount of TRPV4 at the plasma membrane (**Fig. 5K**; $R^2 \sim 0.73$) and decreased with increased cell volume (**Fig. 5L**; $R^2 \sim 0.89$). Cell movement and invasiveness showed a strong linear correlation (**Fig. 5M**; $R^2 \sim 0.85$), suggesting that these behaviors are governed by the same underlying mechanisms. Thus, our motility assay can inform cell invasiveness at the single-cell level.

Mechanosensitive TRPV4 relocation to plasma membrane indicates enhanced invasiveness

We investigated whether the mechanosensitive relocation of TRPV4 to the plasma membrane can reliably predict a cell's ability to undergo pro-invasive mechanosensitive cell volume reduction. To achieve this, we used changes in cell motility as markers for overall shifts in cell invasiveness, given the strong correlation observed between cell motility and invasiveness (**Fig. 5M**). Our hypothesis is that cells with such mechanotransduction capability, like MCF10DCIS.com cells, should show increased plasma membrane association of TRPV4 when inhibited with GSK219 or under hyperosmotic conditions, evidenced by increased cell motility (*D*) while demonstrating the opposite effect with GSK101 treatment.

For comparison, we employed three uncharacterized cell types: MDA-MB-231, a triple-negative invasive breast cancer cell line, and two recently developed patient-derived DCIS cell lines, ETCC-06 and ETCC-10[64,65], which have not yet been histologically classified by grade. These cells were compared with positive control groups, including MCF10DCIS.com and MCF10CA1a,

which were observed to possess pro-invasive mechanotransduction capability (**Fig. 5D**, **6A-6C**). MCF10AT1 served as a negative control, as it lacks this capability (**Fig. 6D-6F**).

MCF10CA1a cells showed plasma membrane relocation of TRPV4 in response to TRPV4 inhibition (1 nM GSK219; ND 219H), PEG 300 (74.4 mOsm/kg; ND PEG300), and OC conditions. In contrast, treatment with 0.2 pM GSK101 did not affect TRPV4 plasma membrane association (**Supplementary Fig. 16** and **Fig. 6A**, showing IF images for TRPV4 (red) and DAPI (cyan)). This response was similar to that observed in MCF10DCIS.com cells under OC conditions. The plasma membrane associations of TRPV4 were quantified by line analysis, showing an increase under mechanical stresses (PEG and OC) and TRPV4 inhibition with GSK219, as plotted in **Fig. 6B.** As expected, based on the differences in plasma membrane TRPV4 association, MCF10CA1a cells exhibited increased motility (*D*) in response to TRPV4 inhibition (GSK219) and hyperosmotic conditions (PEG). Additionally, their movement became more directional (*v*) with TRPV4 activation (GSK101), similar to the observations in MCF10DCIS.com cells **(Fig. 5I, 5J)**.

In contrast, the negative control MCF10AT1 cells did not exhibit TRPV4 inhibition-dependent plasma membrane relocation of TRPV4, as shown by IF images (**Suppl. Fig. 14, Fig. 6D**) and line analysis results (**Fig. 6E**). In these cells, TRPV4 inhibition (GSK219) decreased diffusivity (*D*), while PEG 300 had no effect. Moreover, movement directionality (*v*) remained unchanged under all treatment conditions (**Fig. 6F**).

The three test group cells, MDA-MB-231 (**Fig. 6G, 6H**), ETCC-06 (**Fig. 6J, 6K**), and ETCC-10 (**Fig. 6M, 6N**), failed to relocate TRPV4 to the plasma membrane in response to mechanical stresses (PEG and OC), as shown by IF images and quantification. This suggests that these cells lack the pro-invasive mechanosensitive cell volume reduction capability observed in

MCF10DCIS.com cells. Consistently, none of these cells showed increased motility (*D*) under hyperosmotic conditions or TRPV4 inhibition (**Fig. 6I, 6L, 6O**).

We plotted these results to show cell diffusivity (*D*) scaling with varying plasma membrane associations of TRPV4, where MCF10DCIS.com (green hexagon) and MCF10CA1a (red hexagon) exhibited a positive scaling (**Fig. 6P**). However, the changes in plasma membrane TRPV4 occurred over a narrower range (31 – 79%) for MCF10CA1a compared to MCF10DCIS.com cells (16 - 75%), reflecting the larger mechanosensitive cell volume plasticity of MCF10DCIS.com cells. In contrast, MDA-MB-231, ETCC-6, and ETCC-10 cells did not show this scaling (**Fig. 6Q**). Like MCF10AT1 cells, plasma membrane TRPV4 associations in these cells remained at similar percentages (**Fig. 6Q**).

This dichotomy in the presence of a pro-invasive mechanotransduction program is evident in the plots of diffusivity (*D*) increase versus plasma membrane TRPV4 relocation (**Fig. 6R**), where only MCF10CA1a and MCF10DCIS.com cells show a significant increase in both parameters. Furthermore, the relationship between plasma membrane-associated TRPV4 and *D* increase with GSK219 versus GSK101 can be used to assess the presence of a pro-invasive, mechanosensitive cell volume reduction program. Most non-mechanotransducing cells remained close to the baseline value of 1, while mechanotransducing cells showed a significant increase in *D* with GSK219 treatment.

Discussion

Our study explored how cell crowding, a common condition in diseases and development, impacts cell invasiveness. We employed novel assays to quantify cell invasion and single-cell motility in cells with breast tissue pathologies, including DCIS and ADH, which experience cell crowding due to abnormal proliferation in confined ducts. Our results revealed a novel mechanotransduction

pathway activated by crowding in high-grade DCIS cells, establishing a direct link between crowding and invasiveness. This pathway highlights the intricate interplay between mechanical stimuli, ion channel activation, trafficking changes, cell volume reduction, stiffening, and invasiveness (**Fig. 7**). It distinguishes high-grade DCIS cells from normal, hyperplastic, or lower-grade DCIS cells, supporting previous findings that minimal cell volume reduction enables efficient invasion[38].

The correlation between cell volume reduction and increased invasiveness highlights the specialized mechanotransduction abilities of high-grade DCIS cells. Using mass spectrometry, we identified TRPV4 as a crucial component of this pathway, providing insights into how non-invasive breast cancer cells may evolve into invasive phenotypes. By employing Fluo-4 assays and TRPV4 activators and inhibitors, we found that cell crowding triggered TRPV4 inhibition, leading to reduced intracellular calcium and subsequent cell volume reduction in MCF10DCIS.com cells. Notably, TRPV4 inhibition prompted its relocation to the plasma membrane, priming it for activation under suitable signaling conditions, thereby maintaining cellular homeostasis. TRPV4 inhibition by cell crowding increased invasiveness and motility, while TRPV4 activation had the opposite effect. Reducing TRPV4 protein expression by 50% via shRNA diminished the calcium decrease and volume reduction under mechanical stress, such as cell crowding and hyperosmotic conditions. Consequently, these cells did not exhibit increased motility under hyperosmotic conditions, demonstrating TRPV4's critical role in pro-invasive cell mechanotransduction via cell volume reduction. Invasive MCF10CA1a cells also demonstrated the modest mechanotransduction capability. In contrast, other invasive breast cancer cell lines, such as MDA-MB-231 cells, exhibited opposing responses to TRPV4 inhibition and activation, highlighting the heterogeneity of TRPV4 roles in invasive cancer progression[81-83].

Our discovery of the selective mechanotransduction pathway in high-grade DCIS cells was further validated by analyzing patient-derived breast cancer tissues. We found that TRPV4 was predominantly associated with the plasma membrane in high-grade DCIS lesions, but not in lower-grade DCIS or less aggressive pathologies. This selective relocation reinforces TRPV4's crucial role in the pro-invasive mechanotransduction pathway unique to high-grade DCIS cells. The association of TRPV4 with the plasma membrane may serve as a valuable biomarker for identifying high-grade DCIS lesions.

Our data indicate that ion channels beyond TRPV4 may contribute to pro-invasive mechanotransduction. Notably, SCN11A and KCNN4 showed increased plasma membrane association under cell crowding conditions, suggesting their roles in modulating ion flux and cell volume and thus contributing to the mechanotransduction response. Although Piezo1 is known to respond to mechanical stimuli[62], its lesser plasma membrane relocation compared to TRPV4 under cell crowding and hyperosmotic conditions suggests a lesser role in promoting invasiveness in this case. Further comparisons are needed to determine the dominant ion channel driving mechanotransduction in high-grade DCIS cells. However, it is evident that cell crowding-induced pro-invasive cell volume reduction pathway involves the coordinated action of multiple ion channels[27,84].

We made the intriguing discovery that hyperosmotic conditions, which reduced` cell volume through osmotic water outflow, mimic the effects of cell crowding by inducing similar pro-invasive cell volume reduction. Treatment with hyperosmotic agents like PEG 300 led to TRPV4 relocation to the plasma membrane and increased cell invasiveness, highlighting TRPV4's mechanosensing role in response to external mechanical stimuli. This suggests that the convergence of mechanical stresses, including cell crowding and hyperosmotic stress, is a crucial trigger for pro-invasive cell volume reduction pathways, leading to a unified mechanotransduction signaling cascade.

The study's insights have far-reaching implications, unlocking new research paths in cancer and biological sciences. By elucidating mechanosensitive responses to cell crowding, we can shed light on tissue development, wound healing, and physiological processes involving cell density changes. The parallels between cell crowding and hyperosmotic conditions in driving pro-invasive behaviors warrant further investigation into the intricate mechanisms of cytoskeleton reorganization, ion channel and transporter relocation, and enhanced cell invasiveness and motility. Importantly, our findings elucidate the mechanotransduction capability of high-grade DCIS cells that differentiate them from less aggressive cells. This understanding paves the way for developing diagnostic and prognostic strategies that leverage the selective intracellular localization patterns of TRPV4 and other mechanosensitive ion channels, ultimately guiding clinical decisions for patients with high-risk DCIS and other cancers.

Materials and methods

Cell culture and treatments

MCF10A cells were purchased from ATCC, and MCF10AT1, MCF10DCIS.com, and MCF10CA1a cells were procured from the Barbara Ann Karmanos Cancer Institute after establishing material transfer. These cells were authenticated prior to purchase, and cells with a low passage number (< 15) were used for experiments. We confirmed that the cells were mycoplasma-free using PCR analysis. MCF10A and MCF10AT1 cells were maintained in DMEM/F12 supplemented with 5% horse serum, 20 ng/mL EGF, 0.5 µg/mL hydrocortisone, 10 µg/mL insulin, and 1% penicillin and streptomycin. MCF10A cells were also supplemented with 100 ng/mL cholera toxin. MCF10DCIS.com and MCF10CA1a cells were cultured in DMEM/F12 supplemented with 5% horse serum and 1% penicillin and streptomycin. cells were cultured in 5% CO_2 at 37 °C. For

TRPV4 activator and inhibitor, we used GSK 1016790A (GSK101; Tocris 64T33) and GSK 2193874 (GSK219; Tocris 5106).

For volume measurements, parental cells were mixed with those expressing RFP at a 9:1 ratio to distinguish individual cells. Cells were treated with 2% (74.4 mOsmol/kg) or 4% PEG-300 (148.8 mOsmol/kg; v/v; Millipore Sigma 8074845000) in culture medium for 15 min, 2% PEG-300 for 48 h, or GSK1016790A (Tocris; 0.05 and 0.2 pM) or GSK2193874 (Tocris; 0.2 and 1 nM) for 48 h.

TRPV4 knockdown by shRNA

Cells in growth medium without penicillin and streptomycin were transfected with the hTRPV4 shRNA plasmid (1 and 2 µg; Santa Cruz sc-61726-SH) and Lipofectamine3000 in opti-MEM. At 6 h after transfection, the medium was replaced, and cells were cultured for 30 h before processing for western blot and immunofluorescence analyses.

Immunofluorescence

The cells were fixed with 4% paraformaldehyde (Fisher Scientific) for 20 min, followed by permeabilization with 0.1% saponin (Fisher Scientific) for 5 min at room temperature (RT). After permeabilization, the cells were washed three times in PBS and blocked in 0.1% saponin + 10% BSA in PBS at RT for 1 h. Cells were incubated with primary antibodies overnight at 4 °C in 0.1% saponin in PBS. The primary antibodies used were TRPV4 (Abcam 39260; 1:500 dilution), TfR (ThermoFisher Scientific 13-6800; 1:500 dilution), Piezo1 (Alomone APC-087; 1:500), and KCNN4 (Alomone ALM-051; 1:500). Cells were washed three times in PBS, incubated with fluorescent-tagged anti-rabbit-Alexa 550 or anti-mouse-Alexa 488 secondary antibodies (Thermo Fisher Scientific) and DAPI for 1 h at RT, and imaged by confocal microscopy. For plasma membrane staining, $DiIC_{18}(3)$ (`1,1'-Dioctadecyl-3,3,3',3'-Tetramethylindocarbocyanine Perchlorate; $DiIC_{18}(3)$; Thermo Fisher Scientific, Cat # D282) was diluted in warm PBS to 5 uM.

Media was removed from the cells, then the 5 uM $DiIC_{18}(3)$ in PBS was added. The dish was transferred to the incubator (37 C, 5% CO2) for 10 minutes. Following the 10 min incubation, the $DiIC_{18}(3)$ in PBS was removed and the cells were washed 2x with complete cell growth media. The cells were then fixed with 2% PFA in PBS

Confocal imaging and image processing

2D images were acquired using a Yokogawa spinning-disk confocal microscope (Andor Technology) installed in a Nikon Eclipse TE2000 inverted microscope using a 60x/1.49NA Plan Apo objective (Nikon). The samples were illuminated using 430, 488, 561, and 647 nm solid-state lasers (Andor Technology). Images were acquired using an iXon back-illuminated EMCCD camera (Andor Technology). For volume measurements, 3D confocal images were acquired using z-step sizes calculated based on Nyquist conditions. Images were processed using the ImageJ (NIH) or Imaris (Bitplane) software. For live cell imaging, cells were maintained in 5% CO_2 at 37 °C in a stage-top incubator (Oko-lab).

Western blotting

ND cells (40–60% cell density) were lysed in SDS sample buffer, and OC cells were lysed in cytoskeleton buffer (10 mM Tris pH 7.4,100 mM NaCl, 1 mM EDTA, 1 mM EGTA, 1% Triton X-100, 10% glycerol, 0.1% SDS, 0.5% deoxycholate). SDS sample buffer (Bio-Rad) supplemented with reducing reagent was added to lysates and boiled at 100°C for 10 min. The samples were separated on 4–15% SDS-PAGE gels and transferred to nitrocellulose membranes (Bio-Rad). Membranes were blocked in TBST (TBS + 0.1% Tween-20) containing 5% non-fat milk and then incubated with primary TRPV4 antibody (ThermoFisher Scientific PA541066; 1:1000) and GAPDH (Santa Cruz sc-32233; 1:2000) overnight at 4 °C. Membranes were washed three times in TBST (5 min each) and then incubated with horseradish peroxidase (HRP)-conjugated anti-rabbit (ThermoFisher Scientific A28177) or anti-mouse (ThermoFisher Scientific A28177)

secondary antibodies for 30 min at RT. Blots were visualized using West Femto maximum sensitivity chemiluminescent substrate (Thermo Fisher Scientific).

Lentiviral infection and stable cell generation

To produce lentiviruses encoding RFP, HEK-293 cells were transfected with the lentiviral vector plasmid DNA using Lenti-X Packaging Single Shots (Takara). pCSII-EF-miRFP670v1-hGem(1/110) was a gift from Vladislav Verkhusha (Addgene plasmid # 80006 ; http://n2t.net/addgene:80006 ; RRID:Addgene_80006). Supernatants containing lentiviral pseudoparticles were harvested 24 and 48 h post-transfection. harvested lentiviral particles were immediately stored at −80 °C. To establish stable cell lines, 70% confluent cells at one day post-seeding were infected with lentivirus in the presence of 8 μg/mL polybrene (Thermo Fisher Scientific). Two days after transduction, 1 μg/mL puromycin (Thermo Fisher Scientific) was added to the medium to select for stably transduced cells. The samples were visualized daily to ensure that the untransduced cells in the wells were not viable. Once the polyclonal populations had sufficiently expanded, cell stocks were prepared and harvested for protein expression assays.

Cell invasion assay

For cell invasion assays, 8-well chamber slides (Nunc Lab-Tek) were coated with 50 μg/mL poly-L-lysine (Thermo Fisher Scientific) for 30 min and washed with PBS. The slides were fixed with 0.5% glutaraldehyde (Thermo Fisher Scientific) for 20 min and washed. Gelatin was conjugated with fluorescein by mixing 200 μL fluorescein-gelatin (1 mg/mL; ThemoFisher Scientific) with 800 μL unlabeled gelatin (4 mg/mL), followed by incubation for 5 min at 60 °C. The gelatine mix was allowed to cool at RT for 5 min and then applied, and the slides were incubated for 15 min. Slides were washed with PBS and disinfected with 70% ethanol for 30 min. Following three PBS washes, the residual reactive groups were quenched with growth medium by incubating at room temperature for 30 min in the dark. Cells were seeded in a fresh growth medium and incubated

undisturbed on a horizontal surface at RT for 30 min to encourage cell distribution. Chamber slides were incubated with 5% CO_2 at 37 °C. To detect cell invasion, cells were fixed with 4% formaldehyde and stained with DAPI (Thermo Fisher Scientific), and imaging was performed using a x4/0.2 NA Plan Apo objective (Nikon). Cell invasion was determined by quantifying the sites of the degraded matrix, which were visible as dark areas in the bright-green fluorescent gelatin matrix. The area of gelatin digestion and the number of cells were calculated using the ImageJ software.

Nanoindenter assay for measuring cortical stiffness

Stiffness measurements were performed on live cells in 5% CO2 at 37 °C, maintained in a stage-top chamber (Oko-lab) using a nanoindenter (Optics11 Chiaro) attached to the confocal microscope. Nanoindentation was performed at the cell surface of single cells with an indentation probe with a spring constant (0.24 N/m) and tip diameter (10 μm). The Hertzian contact model was used to fit the data to extract Young's modulus in the elastic regime.

Surface biotinylation and pull-down assay

ND cells that were 40%–70% confluent and OC cells were detached and washed twice with PBS. The cells were resuspended at a concentration of 25×10^6 cells/mL in PBS containing 2 mM sulfo-NHS-biotin (Invitrogen). The reaction mixture was then incubated at RT for 60 min. Cells were washed three times with 1 M Tris pH 8.0 to quench and remove the excess biotin reagent. Cell pellets were lysed in 1.0 mL of cold lysis buffer (50 mM HEPES pH 7.2, 150 mM NaCl, 1.0% Triton X-100, 1.0% CHAPS, 100x protease and phosphatase inhibitors). Lysates were incubated on ice for 30 min, transferred to tubes, and centrifuged (10,000 × *g* for 5 min) to remove insoluble material. Supernatants were collected, and protein concentrations were measured using the bicinchoninic acid assay (Pierce). We washed 50 μL resin (ThermoFisher Scientific) with immobilized streptavidin twice with binding buffer (0.1 M phosphate, 0.15 M NaCl pH 7.2) and

centrifuged at 5000 x *g* for 1 min. Biotin-labelled cell lysate (1 mg) was added to the resin and incubated with rotation for 1 h at RT. The resin was washed by resuspending in binding buffer, centrifuging to pellet the resin, and removing the supernatant by aspiration. The wash was repeated four times. Samples were boiled in SDS-PAGE sample buffer with DTT and separated by electrophoresis.

Mass spectrometry

Peptide mixtures from each sample were analyzed by LC-MS/MS using a nano-LC system (Easy nLC1000) connected to a Q Exactive HF mass spectrometer (Thermo Fisher Scientific). The platform was configured with a nano-electrospray ion source (Easy-Spray, ThermoFisher Scientific), an Acclaim PepMap 100 C18 nanoViper trap column (3 μm particle size, 75 μm ID × 20 mm length), and an EASY-Spray C18 analytical column (2 μm particle size, 75 μm ID × 500 mm length). Peptides were eluted at a flow rate of 300 nL/min using linear gradients of 5–25% acetonitrile (in aqueous phase and 0.1% formic acid) for 40 min, followed by 45% for 10 min, and static flow at 90% for 10 min. Mass spectrometry data were collected in a data-dependent manner, switching between one full-scan MS mode (m/z:380–1400; resolution: 60 K; AGC:3e6; maximum ion time:20 ms), and 10 MS/MS scans (resolution: 15 K; AGC:1e5; maximum ion time:120 ms; nCE:27) of the top 10 target ions. Ions were sequenced once and dynamically excluded from the list for 20 s. The datasets were searched using MaxQuant at default parameters against the UniProt Human Proteome database.

Line analysis

IF images of ion channels (TRPV4, PIEZO1, or KCNN4), $DiIC_{18}(3)$, and DAPI were opened in ImageJ. These images were concatenated so that a line crossing a cell in all three images could be used to measure approximate percentage protein localization in the plasma membrane, cytosol, or nucleus. Background was subtracted from all images. $DiIC_{18}(3)$ signal was used as a

guide for plasma membrane location (between 50% of the peak intensity) and DAPI signal (between 50% of the peak intensity) for nuclear locations. The cytosol location was defined as the region between the 50% peak intensity points of the $DiIC_{18}(3)$ and DAPI signals. The ion channel signal in each window along the line was then averaged. The percentage of protein localization in the plasma membrane, cytosol, or nucleus for a cell was calculated by dividing the average intensity of each location by the sum of intensities in all three locations.

Live cell detection of plasma membrane associated TRPV4

Cells were seeded in a LabTek II 8-well Chambered Coverglass dish (Thermo Fisher 155409) at a density of 10,000 cells per well and allowed to adhere and grow for 2 days. Afterward, the cells were incubated on ice for 1 hour with 1:300 Anti-TRPV4 (extracellular) rabbit primary antibody (Alomone ACC-124) in either complete media or 74 mOsm/Kg PEG 300 in complete media. Following the incubation, the cells were washed twice with the respective media (complete media or 74 mOsm/Kg PEG 300 in complete media) while remaining on ice. Subsequently, the cells were stained for 1 hour at 22 °C with 1:5,000 Donkey anti-Rabbit IgG H+L Highly Cross-Adsorbed Secondary Antibody, Alexa Fluor™ 647 (Thermo Fisher A31573) in the same respective media. After the staining period, the cells were imaged.

Pipeline for analyses of patient histologic samples

1. Specimen collection: A retrospective clinical study was designed to collect patient tissue blocks. A pathologist chose 39 patient breast formalin-fixed paraffin-embedded (FFPE) tissue specimens of a combination of the following pathologies (benign, ADH, IDC, low-, intermediate-, or high-grade DCIS, and IDC), along with normal tissue for each patient. Specimens associated with a past cancer diagnosis and drug treatment history were excluded.

2. Sample preparation for histopathologic evaluation: For each FFPE block, two serial dissections were carried out. Tissue sections on unlabeled slides were stained with hematoxylin and eosin (H&E) and subjected to immunohistochemical (IHC) staining using TRPV4 antibodies (Abcam 39260; 1:100 dilution). Whole-slide images were captured using the Olympus VS200 whole-slide imaging system. To validate the binding specificity of the antibody, both negative and positive control samples were prepared.

3. Two sequential annotations: A breast surgical pathologist annotated the pathology stages within specified regions of interest (ROIs) on wholeslide H&E images, based on cell morphological features. Two pathologists independently evaluated the same ROIs in the corresponding IHC images. They annotated the protein distribution using a three-tier classification:

Case 1: Absence of TRPV4.

Case 2: Intracellular TRPV4 localization.

Case 3: Presence of TRPV4 in the plasma membrane, with or without intracellular TRPV4.

The independent annotations concerning protein localization by the two pathologists were then subjected to statistical tests for selectivity and specificity. Any IHC ROIs with classification disagreements between the pathologists were designated as equivocal cases.

Calcium reporter assay

This assay was completed using the Fluo-4 Direct™ Calcium Assay Kit (Thermo Fisher F10471), including the assay buffer (Thermo Fisher), 2X Fluo-4 calcium assay reagent (Thermo Fisher), and preweighed, water-soluble probenecid (Thermo Fisher P36400; 2.5 mM). The 2X Fluo-4 calcium assay reagent was first prepared by adding 10 mL of the Fluo-4 calcium assay buffer and 200 μL of 250 mM probenecid to the desiccated calcium assay reagent at room temperature

(21 °C). This mixture was then vortexed and allowed to sit for 15 minutes. While waiting for the 2X Fluo-4 calcium assay reagent to finish being prepared, the media from the well of a LabTek II Chambered Coverglass with Cover #1.5 Borosilicate Sterile 8-well plate (Thermo Fisher 155409) was removed and replaced with 200 µL of complete media. Once the 2X Fluo-4 calcium assay reagent was fully prepared, 200 µL of the reagent was added to the well with 200 µL of complete media. The 8-well plate was then placed at 37 °C and 5% CO_2 for 30 minutes. Following 30 minutes at 37 °C and 5% CO_2, the 8-well plate was removed from the incubator and placed at room temperature for 30 minutes. After incubation in the reagent for 30 minutes at room temperature, the 8-well plate was imaged using the confocal microscope with a 488 nm laser for 30 minutes with 30-second intervals between images and an exposure time of 200 ms. If the sample was treated, the sample was imaged for 35 minutes with 30-second intervals, with the treatment being added after 5 minutes had elapsed. Added treatments all had a final volume of 200 µL and were composed of: 1 nM GSK 2 in 1:1 media:2X Fluo-4 calcium assay reagent, 0.2 nM GSK 2 in 1:1 media:2X Fluo-4 calcium assay reagent, 0.2 pM GSK 1 in 1:1 media:2X Fluo-4 calcium assay reagent, 1:1:1 water:media:2X Fluo-4 calcium assay reagent, and 0.3 Osm/L PEG 300 in 1:1 media:2X Fluo-4 calcium assay reagent.

Cell motility assay

Cells were first seeded in MatTek 35 mm dishes with No. 1.5 coverslip, 14 mm glass diameter, and Poly-D-Lysine coated glass bottoms (MatTek P35GC-1.5-14-C). Once the cells adhered, they were stained with 10 µg/mL WGA-488 (Thermo Fisher W11261) for 10 minutes at room temperature. Following the staining, the cells were washed with complete media twice and then incubated at 37 °C and 5% CO_2 for 1 hour. During this one-hour incubation, the cells received the

following treatments: 0.2 pM GSK 101 in complete media for 1 hour, 0.05 pM GSK 101 in complete media for 1 hour, 1 nM GSK 219 in complete media for 1 hour, 0.2 nM GSK 219 in complete media for 1 hour, 74.4 mOsm/Kg PEG 300 in complete media for 15 minutes, and 1:1 hypoosmotic solution in complete media for 15 minutes. After the incubation, the sample was placed in an OkoLab chamber at 37 °C and 5% CO_2 for imaging. Imaging was completed using a confocal microscope with a 488 nm laser for 3 hours with 1-minute intervals.

Cell viability assay

MCF10DCIS.com cells were plated in a LabTek II 8-well Chambered Coverglass dish (Thermo Fisher 155409) at a seeding density of 10,000 cells per well. Once the cells in the well reached the desired number of days post-confluence, they were stained using Propidium Iodide Ready Flow Reagent (Thermo Fisher R37169). Specifically, 1 drop of propidium iodide (PI) was added to 500 µL of cell growth medium per well and incubated for 15 minutes at room temperature (22°C). After staining, the cells were washed twice with complete growth medium. Next, the cells were stained with 1 µg/mL WGA-488 (Thermo Fisher w11261) in complete growth medium for 15 minutes at 37°C in a 5% CO_2 atmosphere. Following the incubation with WGA-488, the cells were washed three times with complete growth medium and then incubated for 2 hours at 37°C in 5% CO_2 to allow WGA migration into the nuclei. Finally, the cells were imaged using confocal microscopy at 4X magnification, with laser excitation at 488 nm for WGA-488 and 560 nm for propidium iodide.

Data availability

Data available on reasonable request from the corresponding author (I. Chung).

Acknowledgments

I. Chung is supported by the Elsa Pardee Foundation Award, the Clinical and Translational Science Institute at Children's National Fund, the George Washington Cross-Disciplinary Research Fund, the George Washington Cancer Center, and the Katzen Cancer Research Pilot Award. We thank M. Sliwkowski, M. Sagola, and Genentech, Inc. for kindly arranging the transfer of an optical microscope and for previous scientific discussions. We are also grateful to A. Schwartz and S. Weiss for their helpful feedback on the manuscript, I. Teng for initial assistance with invasion assays, and P.F.G. Rodriguez for assistance in setting up the nanoindenter. P. Aswini provided valuable help with MS data analysis, and S. Simmens offered helpful statistical consultation. N. Suh contributed discussions on MCF10A cell derivatives, and K. Schill from DigitalScope assisted with IHC image data management. We also acknowledge H. Yoo for summarizing in vivo data and A. Yohannes, H. Yoo, J. John, S. Rachidi, S. Ravulapalli, and R. Yu for their efforts in cell management and raw image processing.

Author Contributions:

I.C. conceived and supervised the project, secured funding, designed experiments, methods, and analyses, and wrote the manuscript with comments from all authors. X.B. optimized the conditions for the invasion assays and conducted analyses, and performed immunoprecipitation, cell volume measurement, and biochemical assays. N.A. conducted immunofluorescence imaging, calcium imaging, and cell motility assay. T.V. performed invasion assays and analyses, cell volume measurements, biochemical assays, and immunofluorescence imaging. S.L. performed the stiffness and volume measurements, biochemical assays, and mass spectrometry. A.G. and N.A. performed the line analysis of IF images. X.B. and K.Y. generated stable cell lines expressing the fluorescent proteins. S.T. and P.L. annotated the hematoxylin and eosin-stained and immunohistochemical images. P.L. and C.T. collected the retrospective patient tissue blocks.

Competing Interest:

The authors declare no competing non-financial interests but the following competing financial interests: A patent related to the findings described in this manuscript has been granted by the USPTO.

Corresponding authors

Correspondence to Inhee Chung.

References

1 Kuehlmann, B., Bonham, C. A., Zucal, I., Prantl, L. & Gurtner, G. C. Mechanotransduction in Wound Healing and Fibrosis. *J Clin Med* **9** (2020). https://doi.org/10.3390/jcm9051423

2 Broders-Bondon, F., Nguyen Ho-Bouldoires, T. H., Fernandez-Sanchez, M. E. & Farge, E. Mechanotransduction in tumor progression: The dark side of the force. *J Cell Biol* **217**, 1571-1587 (2018). https://doi.org/10.1083/jcb.201701039

3 Hall, C. M., Moeendarbary, E. & Sheridan, G. K. Mechanobiology of the brain in ageing and Alzheimer's disease. *Eur J Neurosci* **53**, 3851-3878 (2021). https://doi.org/10.1111/ejn.14766

4 Moore, S. W., Roca-Cusachs, P. & Sheetz, M. P. Stretchy proteins on stretchy substrates: the important elements of integrin-mediated rigidity sensing. *Dev Cell* **19**, 194-206 (2010). https://doi.org/10.1016/j.devcel.2010.07.018

5 Jansen, K. A., Atherton, P. & Ballestrem, C. Mechanotransduction at the cell-matrix interface. *Seminars in Cell & Developmental Biology* **71**, 75-83 (2017). https://doi.org/10.1016/j.semcdb.2017.07.027

6 Jaalouk, D. E. & Lammerding, J. Mechanotransduction gone awry. *Nat Rev Mol Cell Biol* **10**, 63-73 (2009). https://doi.org/10.1038/nrm2597

7 Stylianopoulos, T. *et al.* Coevolution of solid stress and interstitial fluid pressure in tumors during progression: implications for vascular collapse. *Cancer Res* **73**, 3833-3841 (2013). https://doi.org/10.1158/0008-5472.CAN-12-4521

8 Polacheck, W. J., German, A. E., Mammoto, A., Ingber, D. E. & Kamm, R. D. Mechanotransduction of fluid stresses governs 3D cell migration. *Proc Natl Acad Sci U S A* **111**, 2447-2452 (2014).https://doi.org/10.1073/pnas.1316848111

9 Galbraith, C. G., Yamada, K. M. & Sheetz, M. P. The relationship between force and focal complex development. *Journal of Cell Biology* **159**, 695-705 (2002). https://doi.org/10.1083/jcb.200204153

10 Burg, M. B., Ferraris, J. D. & Dmitrieva, N. I. Cellular response to hyperosmotic stresses. *Physiol Rev* **87**, 1441-1474 (2007). https://doi.org/10.1152/physrev.00056.2006

11 Finan, J. D. & Guilak, F. The effects of osmotic stress on the structure and function of the cell nucleus. *J Cell Biochem* **109**, 460-467 (2010). https://doi.org/10.1002/jcb.22437

12 Franco, J. J., Atieh, Y., Bryan, C. D., Kwan, K. M. & Eisenhoffer, G. T. Cellular crowding influences extrusion and proliferation to facilitate epithelial tissue repair. *Mol Biol Cell* **30**, 1890-1899 (2019). https://doi.org/10.1091/mbc.E18-05-0295

13 Neurohr, G. E. & Amon, A. Relevance and Regulation of Cell Density. *Trends Cell Biol* **30**, 213-225 (2020). https://doi.org/10.1016/j.tcb.2019.12.006

14 Fan, Y. & Meyer, T. Molecular control of cell density-mediated exit to quiescence. *Cell Rep* **36**, 109436 (2021). https://doi.org/10.1016/j.celrep.2021.109436
15 Kader, T., Hill, P., Rakha, E. A., Campbell, I. G. & Gorringe, K. L. Atypical ductal hyperplasia: update on diagnosis, management, and molecular landscape. *Breast Cancer Res* **20**, 39 (2018). https://doi.org/10.1186/s13058-018-0967-1
16 Bocker, W. Preneoplasia of the breast. *Verh Dtsch Ges Pathol* **81**, 502-513 (1997).
17 Gudjonsson, T., Adriance, M. C., Sternlicht, M. D., Petersen, O. W. & Bissell, M. J. Myoepithelial cells: Their origin and function in breast morphogenesis and neoplasia. *J Mammary Gland Biol* **10**, 261-272 (2005). https://doi.org/10.1007/s10911-005-9586-4
18 Pinder, S. E. & Ellis, I. O. The diagnosis and management of pre-invasive breast disease: ductal carcinoma in situ (DCIS) and atypical ductal hyperplasia (ADH)--current definitions and classification. *Breast Cancer Res* **5**, 254-257 (2003). https://doi.org/10.1186/bcr623
19 Dawson, P. J., Wolman, S. R., Tait, L., Heppner, G. H. & Miller, F. R. MCF10AT: a model for the evolution of cancer from proliferative breast disease. *Am J Pathol* **148**, 313-319 (1996).
20 Miller, F. R. Xenograft models of premalignant breast disease. *J Mammary Gland Biol Neoplasia* **5**, 379-391 (2000). https://doi.org/10.1023/a:1009577811584
21 Dupont, W. D. & Page, D. L. Risk-Factors for Breast Cancer in Women with Proliferative Breast Disease. *New Engl J Med* **312**, 146-151 (1985). https://doi.org/10.1056/Nejm198501173120303
22 van Seijen, M. *et al.* Ductal carcinoma in situ: to treat or not to treat, that is the question. *Br J Cancer* **121**, 285-292 (2019). https://doi.org/10.1038/s41416-019-0478-6
23 Pang, J. M., Gorringe, K. L. & Fox, S. B. Ductal carcinoma in situ - update on risk assessment and management. *Histopathology* **68**, 96-109 (2016). https://doi.org/10.1111/his.12796
24 Zhou, E. H. *et al.* Universal behavior of the osmotically compressed cell and its analogy to the colloidal glass transition. *P Natl Acad Sci USA* **106**, 10632-10637 (2009). https://doi.org/10.1073/pnas.0901462106
25 Shekhar, M. P. *et al.* Comedo-ductal carcinoma in situ: A paradoxical role for programmed cell death. *Cancer Biol Ther* **7**, 1774-1782 (2008). https://doi.org/10.4161/cbt.7.11.6781
26 Miller, F. R., Santner, S. J., Tait, L. & Dawson, P. J. MCF10DCIS.com xenograft model of human comedo ductal carcinoma in situ. *J Natl Cancer Inst* **92**, 1185-1186 (2000). https://doi.org/10.1093/jnci/92.14.1185a
27 White, J. P. *et al.* TRPV4: Molecular Conductor of a Diverse Orchestra. *Physiol Rev* **96**, 911-973 (2016). https://doi.org/10.1152/physrev.00016.2015
28 So, J. Y., Lee, H. J., Kramata, P., Minden, A. & Suh, N. Differential Expression of Key Signaling Proteins in MCF10 Cell Lines, a Human Breast Cancer Progression Model. *Mol Cell Pharmacol* **4**, 31-40 (2012).
29 Santner, S. J. *et al.* Malignant MCF10CA1 cell lines derived from premalignant human breast epithelial MCF10AT cells. *Breast Cancer Res Treat* **65**, 101-110 (2001). https://doi.org/10.1023/a:1006461422273
30 Holland, R. *et al.* Ductal carcinoma in situ: a proposal for a new classification. *Semin Diagn Pathol* **11**, 167-180 (1994).
31 Allred, D. C. Ductal carcinoma in situ: terminology, classification, and natural history. *J Natl Cancer Inst Monogr* **2010**, 134-138 (2010). https://doi.org/10.1093/jncimonographs/lgq035
32 Denisin, A. K. & Pruitt, B. L. Tuning the Range of Polyacrylamide Gel Stiffness for Mechanobiology Applications. *Acs Appl Mater Inter* **8**, 21893-21902 (2016). https://doi.org/10.1021/acsami.5b09344

33 Fischer, R. S., Myers, K. A., Gardel, M. L. & Waterman, C. M. Stiffness-controlled three-dimensional extracellular matrices for high-resolution imaging of cell behavior. *Nat Protoc* **7**, 2056-2066 (2012). https://doi.org/10.1038/nprot.2012.127
34 Lee, J. Y. *et al.* YAP-independent mechanotransduction drives breast cancer progression. *Nat Commun* **10**, 1848 (2019). https://doi.org/10.1038/s41467-019-09755-0
35 Tzur, A., Kafri, R., LeBleu, V. S., Lahav, G. & Kirschner, M. W. Cell Growth and Size Homeostasis in Proliferating Animal Cells. *Science* **325**, 167-171 (2009). https://doi.org/10.1126/science.1174294
36 Guo, M. *et al.* Cell volume change through water efflux impacts cell stiffness and stem cell fate. *Proc Natl Acad Sci U S A* **114**, E8618-E8627 (2017). https://doi.org/10.1073/pnas.1705179114
37 Cuddapah, V. A., Robel, S., Watkins, S. & Sontheimer, H. A neurocentric perspective on glioma invasion. *Nat Rev Neurosci* **15**, 455-465 (2014). https://doi.org/10.1038/nrn3765
38 Watkins, S. & Sontheimer, H. Hydrodynamic cellular volume changes enable glioma cell invasion. *J Neurosci* **31**, 17250-17259 (2011). https://doi.org/10.1523/JNEUROSCI.3938-11.2011
39 Angstadt, S., Zhu, Q., Jaffee, E. M., Robinson, D. N. & Anders, R. A. Pancreatic Ductal Adenocarcinoma Cortical Mechanics and Clinical Implications. *Front Oncol* **12**, 809179 (2022). https://doi.org/10.3389/fonc.2022.809179
40 Barai, A., Mukherjee, A., Das, A., Saxena, N. & Sen, S. alpha-Actinin-4 drives invasiveness by regulating myosin IIB expression and myosin IIA localization. *J Cell Sci* **134** (2021). https://doi.org/10.1242/jcs.258581
41 Shcherbakova, D. M. *et al.* Bright monomeric near-infrared fluorescent proteins as tags and biosensors for multiscale imaging. *Nature Communications* **7** (2016). https://doi.org/10.1038/ncomms12405
42 Radmacher, M. Measuring the elastic properties of living cells by the atomic force microscope. *Methods Cell Biol* **68**, 67-90 (2002). https://doi.org/10.1016/s0091-679x(02)68005-7
43 Guilak, F., Tedrow, J. R. & Burgkart, R. Viscoelastic properties of the cell nucleus. *Biochem Biophys Res Commun* **269**, 781-786 (2000). https://doi.org/10.1006/bbrc.2000.2360
44 Sachs, F. & Sivaselvan, M. V. Cell volume control in three dimensions: Water movement without solute movement. *J Gen Physiol* **145**, 373-380 (2015). https://doi.org/10.1085/jgp.201411297
45 Jiang, H. & Sun, S. X. Cellular pressure and volume regulation and implications for cell mechanics. *Biophys J* **105**, 609-619 (2013). https://doi.org/10.1016/j.bpj.2013.06.021
46 Jentsch, T. J. VRACs and other ion channels and transporters in the regulation of cell volume and beyond. *Nat Rev Mol Cell Biol* **17**, 293-307 (2016). https://doi.org/10.1038/nrm.2016.29
47 Matthews, B. D., Thodeti, C. K. & Ingber, D. E. Activation of mechanosensitive ion channels by forces transmitted through integrins and the cytoskeleton. *Curr Top Membr* **58**, 59-85 (2007). https://doi.org/10.1016/S1063-5823(06)58003-2
48 Wiggins, P. & Phillips, R. Membrane-protein interactions in mechanosensitive channels. *Biophysical Journal* **88**, 880-902 (2005). https://doi.org/10.1529/biophysj.104.047431
49 Zhang, W. *et al.* Ankyrin Repeats Convey Force to Gate the NOMPC Mechanotransduction Channel. *Cell* **162**, 1391-1403 (2015). https://doi.org/10.1016/j.cell.2015.08.024
50 Ranade, S. S., Syeda, R. & Patapoutian, A. Mechanically Activated Ion Channels. *Neuron* **87**, 1162-1179 (2015). https://doi.org/10.1016/j.neuron.2015.08.032
51 Michalick, L. & Kuebler, W. M. TRPV4-A Missing Link Between Mechanosensation and Immunity. *Front Immunol* **11**, 413 (2020). https://doi.org/10.3389/fimmu.2020.00413

52 Rosenbaum, T. *et al.* TRPV4: A Physio and Pathophysiologically Significant Ion Channel. *Int J Mol Sci* **21** (2020). https://doi.org/10.3390/ijms21113837
53 Lee, H. P., Stowers, R. & Chaudhuri, O. Volume expansion and TRPV4 activation regulate stem cell fate in three-dimensional microenvironments. *Nat Commun* **10**, 529 (2019). https://doi.org/10.1038/s41467-019-08465-x
54 Becker, D., Blase, C., Bereiter-Hahn, J. & Jendrach, M. TRPV4 exhibits a functional role in cell-volume regulation. *J Cell Sci* **118**, 2435-2440 (2005). https://doi.org/10.1242/jcs.02372
55 Dib-Hajj, S. D., Black, J. A. & Waxman, S. G. NaV1.9: a sodium channel linked to human pain. *Nat Rev Neurosci* **16**, 511-519 (2015). https://doi.org/10.1038/nrn3977
56 Bennett, D. L., Clark, A. J., Huang, J., Waxman, S. G. & Dib-Hajj, S. D. The Role of Voltage-Gated Sodium Channels in Pain Signaling. *Physiol Rev* **99**, 1079-1151 (2019). https://doi.org/10.1152/physrev.00052.2017
57 Huang, J. *et al.* A Novel Gain-of-Function Nav1.9 Mutation in a Child With Episodic Pain. *Front Neurosci* **13**, 918 (2019). https://doi.org/10.3389/fnins.2019.00918
58 Gu, M. X., Zhu, Y. R., Yin, X. R. & Zhang, D. M. Small-conductance Ca- activated K channels: insights into their roles in cardiovascular disease. *Exp Mol Med* **50** (2018). https://doi.org/10.1038/s12276-018-0043-z
69 Stocker, M. Ca-activated K channels: Molecular determinants and function of the SK family. *Nature Reviews Neuroscience* **5**, 758-770 (2004). https://doi.org/10.1038/nrn1516
60 Chung, I. *et al.* High cell-surface density of HER2 deforms cell membranes. *Nat Commun* **7**, 12742 (2016). https://doi.org/10.1038/ncomms12742
61 Syeda, R. *et al.* Piezo1 Channels Are Inherently Mechanosensitive. *Cell Reports* **17**, 1739-1746 (2016). https://doi.org/10.1016/j.celrep.2016.10.033
62 Coste, B. *et al.* Piezo1 and Piezo2 are essential components of distinct mechanically activated cation channels. *Science* **330**, 55-60 (2010). https://doi.org/10.1126/science.1193270
63 Butner, J. D. *et al.* Dedifferentiation-mediated stem cell niche maintenance in early-stage ductal carcinoma in situ progression: insights from a multiscale modeling study. *Cell Death Dis* **13**, 485 (2022). https://doi.org/10.1038/s41419-022-04939-x
64 Samson, J., Derlipanska, M., Zaheed, O. & Dean, K. Molecular and cellular characterization of two patient-derived ductal carcinoma in situ (DCIS) cell lines, ETCC-006 and ETCC-010. *BMC Cancer* **21**, 790 (2021). https://doi.org/10.1186/s12885-021-08511-2
65 Yong, J. W. *et al.* Characterization of ductal carcinoma in situ cell lines established from breast tumor of a Singapore Chinese patient. *Cancer Cell Int* **14**, 94 (2014). https://doi.org/10.1186/s12935-014-0094-8
66 Ransom, C. B. & Sontheimer, H. Biophysical and pharmacological characterization of inwardly rectifying K+ currents in rat spinal cord astrocytes. *J Neurophysiol* **73**, 333-346 (1995). https://doi.org/10.1152/jn.1995.73.1.333
67 Hoffmann, E. K., Lambert, I. H. & Pedersen, S. F. Physiology of cell volume regulation in vertebrates. *Physiol Rev* **89**, 193-277 (2009). https://doi.org/10.1152/physrev.00037.2007
68 Stutzin, A. & Hoffmann, E. K. Swelling-activated ion channels: functional regulation in cell-swelling, proliferation and apoptosis. *Acta Physiol (Oxf)* **187**, 27-42 (2006). https://doi.org/10.1111/j.1748-1716.2006.01537.x
69 Clapham, D. E. Calcium signaling. *Cell* **131**, 1047-1058 (2007). https://doi.org/10.1016/j.cell.2007.11.028
70 Gee, K. R. *et al.* Chemical and physiological characterization of fluo-4 Ca-indicator dyes. *Cell Calcium* **27**, 97-106 (2000). https://doi.org/10.1054/ceca.1999.0095

71 Cheung, M. *et al.* Discovery of GSK2193874: An Orally Active, Potent, and Selective Blocker of Transient Receptor Potential Vanilloid 4. *ACS Med Chem Lett* **8**, 549-554 (2017). https://doi.org/10.1021/acsmedchemlett.7b00094
72 Baratchi, S. *et al.* The TRPV4 Agonist GSK1016790A Regulates the Membrane Expression of TRPV4 Channels. *Front Pharmacol* **10** (2019). https://doi.org/10.3389/fphar.2019.00006
73 Sullivan, M. N., Francis, M., Pitts, N. L., Taylor, M. S. & Earley, S. Optical recording reveals novel properties of GSK1016790A-induced vanilloid transient receptor potential channel TRPV4 activity in primary human endothelial cells. *Mol Pharmacol* **82**, 464-472 (2012). https://doi.org/10.1124/mol.112.078584
74 Espadas-Alvarez, H. *et al.* TRPV4 activity regulates nuclear Ca(2+) and transcriptional functions of beta-catenin in a renal epithelial cell model. *J Cell Physiol* **236**, 3599-3614, doi:10.1002/jcp.30096 (2021).
75 Liedtke, W. & Friedman, J. M. Abnormal osmotic regulation in trpv4-/- mice. *Proc Natl Acad Sci U S A* **100**, 13698-13703 (2003). https://doi.org/10.1073/pnas.1735416100
76 Bai, S. W. *et al.* The role of transient receptor potential channels in metastasis. *Biomed Pharmacother* **158** (2023). https://doi.org/10.1016/j.biopha.2022.114074
77 Lee, W. H. *et al.* TRPV4 plays a role in breast cancer cell migration via Ca(2+)-dependent activation of AKT and downregulation of E-cadherin cell cortex protein. *Oncogenesis* **6**, e338 (2017). https://doi.org/10.1038/oncsis.2017.39
78 Prevarskaya, N., Skryma, R. & Shuba, Y. Ion channels and the hallmarks of cancer. *Trends Mol Med* **16**, 107-121 (2010). https://doi.org/10.1016/j.molmed.2010.01.005
79 Martinac, B. & Poole, K. Mechanically activated ion channels. *Int J Biochem Cell Biol* **97**, 104-107 (2018). https://doi.org/10.1016/j.biocel.2018.02.011
80 Tojkander, S., Gateva, G. & Lappalainen, P. Actin stress fibers--assembly, dynamics and biological roles. *J Cell Sci* **125**, 1855-1864 (2012).https://doi.org/10.1242/jcs.098087
81 Bien-Ly, N. *et al.* Transferrin receptor (TfR) trafficking determines brain uptake of TfR antibody affinity variants. *Journal of Experimental Medicine* **211**, 233-244 (2014). https://doi.org/10.1084/jem.20131660
82 Chung, I. Optical measurement of receptor tyrosine kinase oligomerization on live cells. *Biochim Biophys Acta* **1859**, 1436-1444 (2017). https://doi.org/10.1016/j.bbamem.2017.03.026
83 Chung, I. *et al.* Spatial control of EGF receptor activation by reversible dimerization on living cells. *Nature* **464**, 783-787 (2010). https://doi.org/10.1038/nature08827
84 Chung, I. & Mellman, I. Receptor Tyrosine Kinases Methods and Protocols. *Methods in Molecular Biology* **1233**, 190 (2014). https://doi.org:10.1007/978-1-4939-1789-1
85 Chung, I. & Mellman, I. Single-molecule optical methods analyzing receptor tyrosine kinase activation in living cells. *Methods Mol Biol* **1233**, 35-44 (2015). https://doi.org/10.1007/978-1-4939-1789-1_4
86 Bai, S. W. *et al.* The role of transient receptor potential channels in metastasis. *Biomed Pharmacother* **158** (2023). https://doi.org/10.1016/j.biopha.2022.114074
87 Lee, W. H. *et al.* TRPV4 plays a role in breast cancer cell migration via Ca(2+)-dependent activation of AKT and downregulation of E-cadherin cell cortex protein. *Oncogenesis* **6**, e338 (2017). https://doi.org/10.1038/oncsis.2017.39
88 Prevarskaya, N., Skryma, R. & Shuba, Y. Ion channels and the hallmarks of cancer. *Trends Mol Med* **16**, 107-121 (2010). https://doi.org/10.1016/j.molmed.2010.01.005
89 Martinac, B. & Poole, K. Mechanically activated ion channels. *Int J Biochem Cell Biol* **97**, 104-107 (2018). https://doi.org/10.1016/j.biocel.2018.02.011

Figures

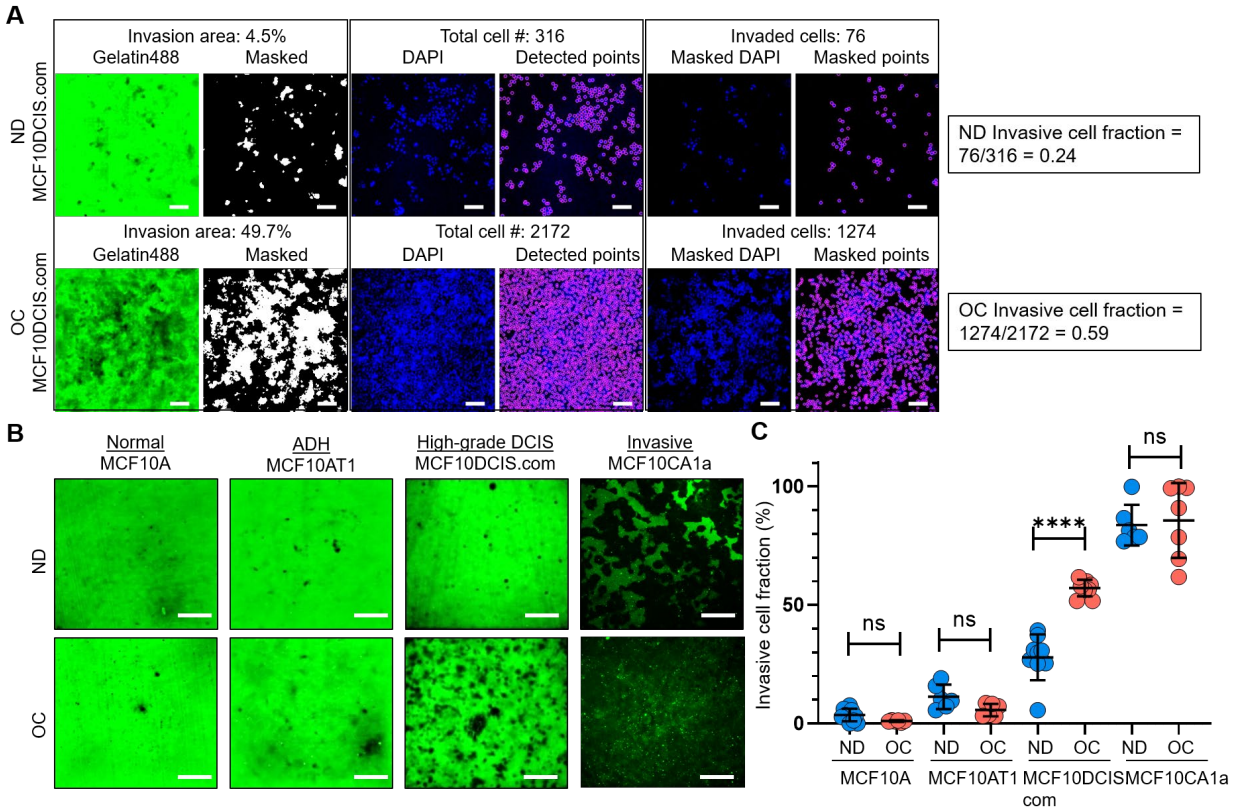

Figure 1. Cell crowding selectively increases invasiveness in high-grade DCIS cells.

(A) We used a collagen-crosslinked polyacrylamide hydrogel matrix-based invasion assay to assess the effect of cell crowding on invasiveness. Representative images show gelatin-Alexa488 conjugates, where dark areas indicate cell invasion through degradation (green; Gelatin488), and DAPI staining marks cell locations (blue; DAPI) in a two-day invasion assay of MCF10DCIS.com cells under normal density (ND; upper panel) and overconfluent (OC; lower panel) conditions. "Masked" images are thresholded to produce positive masks applied to the “DAPI” images. Individual cell locations detected in “DAPI” images are marked with purple circles in “Detected points” images. The total number of cells within the field of view is counted from these points. By overlaying the mask and DAPI images, “Masked DAPI” images are obtained, and invaded cells

are detected and represented by purple circles in “Masked points” images. The invasive cell fraction is calculated by the ratio of the number of invaded cells to the total number of cells (0.24 for ND and 0.59 for OC MCF10DCIS.com cells). These data show that cell invasiveness is enhanced by cell crowding. Scale bar = 100 μm. **(B)** Comparison of “Gelatin488” images of MCF10A (normal breast epithelial cells), MCF10AT1 (ADH-mimicking cells), MCF10DCIS.com (high-grade DCIS mimic), and MCF10CA1a (invasive breast cancer cells) between ND and OC conditions. MCF10DCIS.com cell invasion is significantly higher under cell crowding than under ND conditions. **(C)** Invasive cell fractions of these cells between ND (blue circles) and OC (red circles) conditions are compared, showing that cell crowding-induced increases in invasiveness are notable only in MCF10DCIS.com cells. We used the two-tailed Mann-Whitney U test, a nonparametric and unpaired statistical method, to compare differences between groups. ****: $p < 0.0001$, ***: $p < 0.001$, **: $p < 0.01$, *: $p < 0.05$, ns: $p > 0.05$, throughout the manuscript.

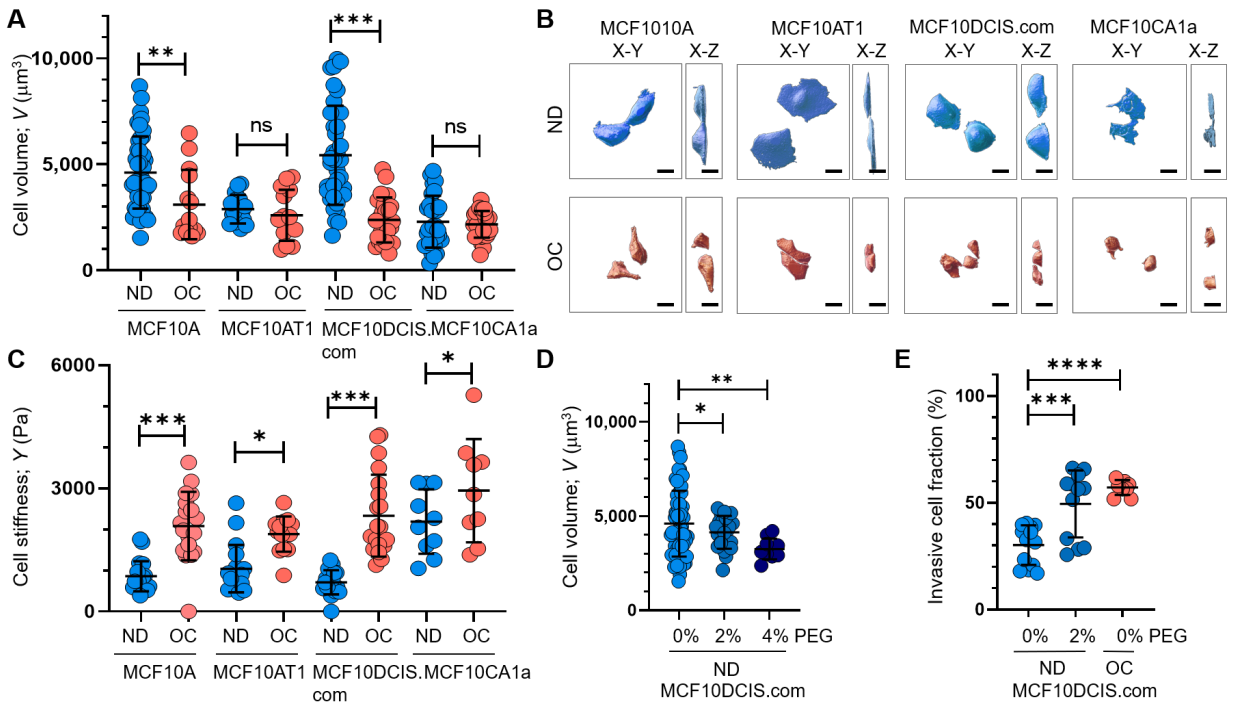

Figure 2. Cell Crowding induces significant cell volume reduction and stiffening in High-Grade DCIS Cells.

(A) Cell volume (*V*; mean and SD) differences between ND (blue circles) and OC (red circles) conditions of MCF10A, MCF10AT1, MCF10DCIS.com, and MCF10CA1a cells are plotted. The high-grade DCIS cell mimic, MCF10DCIS.com, shows a large volume reduction due to cell crowding. **(B)** Representative confocal microscopy images of RFP-coexpressing cells of the four cell types in ND and OC conditions. The images include x-y (left) and x-z (right) views, with scale bar = 10 μm. The large volume reduction of MCF10DCIS.com cells is evident. **(C)** Plots showing changes in cortical stiffness (mean and SD) measured by Young's modulus (*Y*) using a nanoindenter, displaying significant cell stiffening of MCF10DCIS.com cells due to cell crowding. **(D)** Hyperosmotic conditions induced by PEG 300 treatment (darker blue circles for 2% = 74.4 mOsm/Kg; navy circles for 4% = 148.8 mOsm/kg) lead to dose-dependent cell volume reduction. **(E)** Treatment with 2% PEG 300 (darker circles) for two days significantly increased the

invasiveness (mean and SD) of MCF10DCIS.com cells, similar to the OC case (red circles). ****: $p < 0.0001$, ***: $p < 0.001$, **: $p < 0.01$, *: $p < 0.05$, ns: $p > 0.05$.

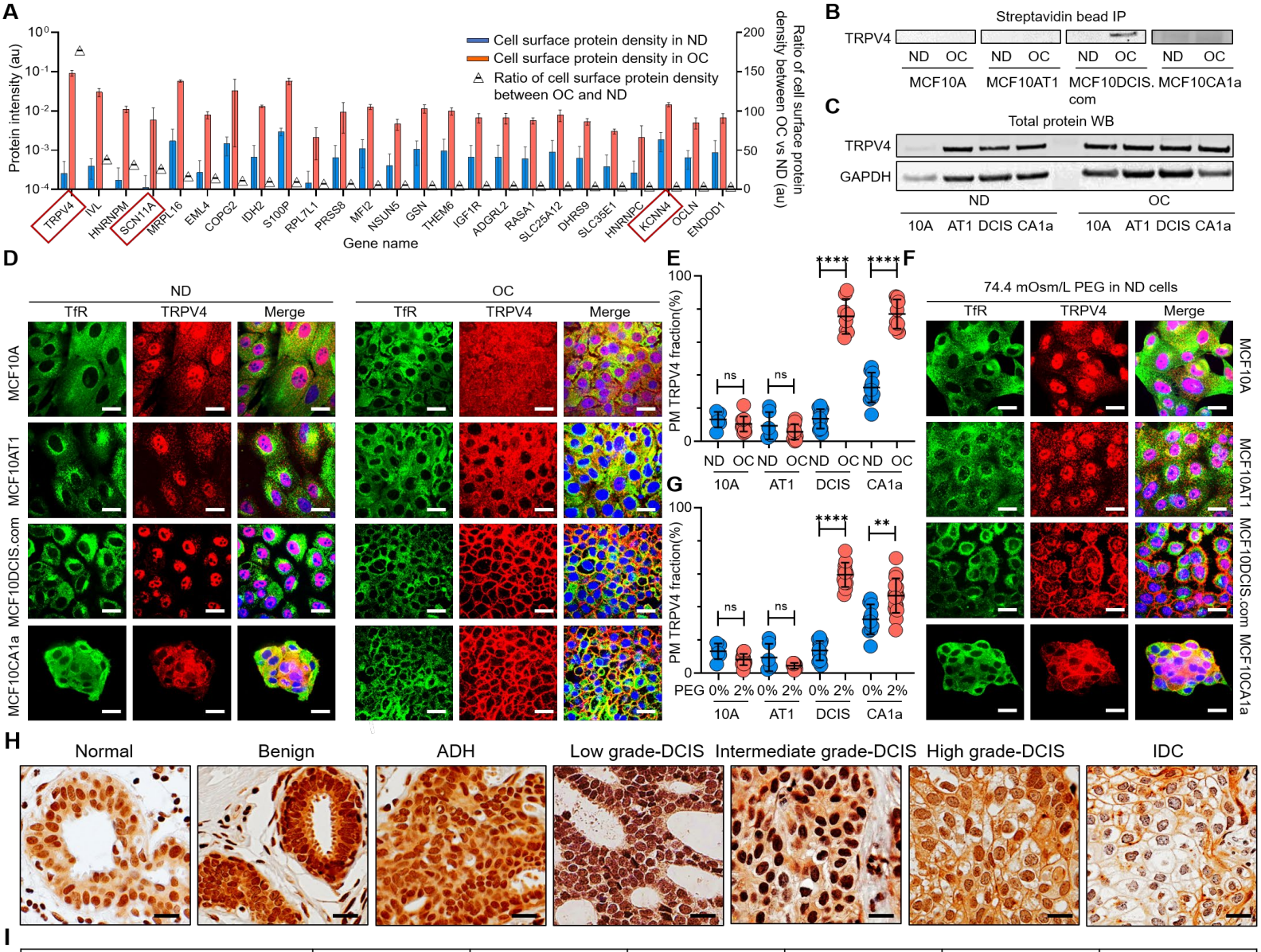

Breast pathology duct phenotypes	Normal			Benign			ADH			LG/IM-DCIS			HG-DCIS			IDC		
Total number of ROIs	14			32			9			7			20			15		
# ROIs featuring PM TRPV4	**Y**	**N**	**E**	**Y**	**N**	**E**	**Y**	**N**	**E**	**Y**	**N**	**E**	**Y**	**N**	**E**	**Y**	**N**	**E**
	0	14	0	0	4	0	0	9	0	0	6	1	15	1	4	11	1	3
% ROIs featuring PM TRPV4	0			0			0			0			75%			73%		

Figure 3. Cell crowding induces TRPV4 relocation to plasma membrane in MCF10DCIS.com cells. (A) Mass spectrometry data showing proteins enriched in the plasma membrane (PM) >5-fold (fold changes represented using triangle plots; OC/ND ratio on the right axis) when cells are under OC (red bars) relative to ND conditions (blue bars). Ion channels are

marked with red boxes, where TRPV4 shows about a 160-fold increased association with the plasma membrane under OC conditions. **(B)** Proteins near and on the plasma membrane were pulled down after cell surface biotinylation with streptavidin beads and immunoblotted for TRPV4. TRPV4 is significantly associated with the plasma membrane in OC MCF10DCIS.com cells. In MCF10CA1a cells, TRPV4 appears to be associated with the plasma membrane under both ND and OC conditions, with a slight increase under OC conditions. **(C)** Immunoblots of whole-protein lysates demonstrate similar overall TRPV4 protein levels across MCF10A cell derivatives, regardless of cell density. This indicates that the differing plasma membrane association of TRPV4 is due to trafficking changes, not expression level changes. GAPDH is used as a loading control. **(D)** Representative IF images by confocal microscopy show TRPV4 (red) localization compared to the control protein transferrin receptor (TfR; green) in MCF10A, MCF10AT1, MCF10DCIS.com, and MCF10CA1a cells under ND and OC conditions. DAPI (blue) staining was used for visualizing the nuclei. As observed in the biochemical data in (**B-C)**, cell crowding induces the relocation of TRPV4 to the plasma membrane in MCF10DCIS.com cells. TRPV4 is associated with the plasma membrane in ND MCF10CA1a cells, with a clear elevated association in OC cells. Scale bar = 10 μm. **(E)** Plasma membrane-associated TRPV4 (%) is quantified for the four cell lines under ND and OC conditions by line analysis, showing a significant increase in both MCF10DCIS.com cells and MCF10CA1a cells due to cell crowding. **(F)** IF images showing that hyperosmotic conditions induced by PEG 300 (74.4 mOsm/Kg) treatment also relocate TRPV4 (red) to the plasma membrane in MCF10DCIS.com cells. TfR localization remains intact under hyperosmotic conditions. Increased relocation is also observed in MCF10CA1a cells. Scale bar = 10 μm. **(G)** The increased plasma membrane association of TRPV4 due to hyperosmotic stress is quantified by line analysis. Scale bar = 10 μm. **(H)** Representative regions of interest (ROIs) of TRPV4-stained immunohistochemistry (IHC) images in different pathology phenotypes. High-grade DCIS and invasive ductal cancer (IDC) ROIs clearly exhibit plasma membrane association of TRPV4. Two high-grade DCIS IHC images were acquired by two different people and both

show plasma membrane-associated TRPV4. Scale bar = 20 μm. **(I)** Statistical results from independent histological evaluations of pathologies and TRPV4 distributions of 97 ROIs from 39 patient specimens indicate a high correlation (>70%) of plasma membrane association of TRPV4 with high-grade DCIS or IDC pathologies. Y/N: Yes/no, indicating both pathologists agreed that PM ion channels were present/absent. E: Equivocal, indicating only one pathologist agreed. Significantly high proportions of high-grade DCIS (75%) and IDC (73%) ROIs exhibited plasma membrane TRPV4 association, which was not observed in lower-risk cases.

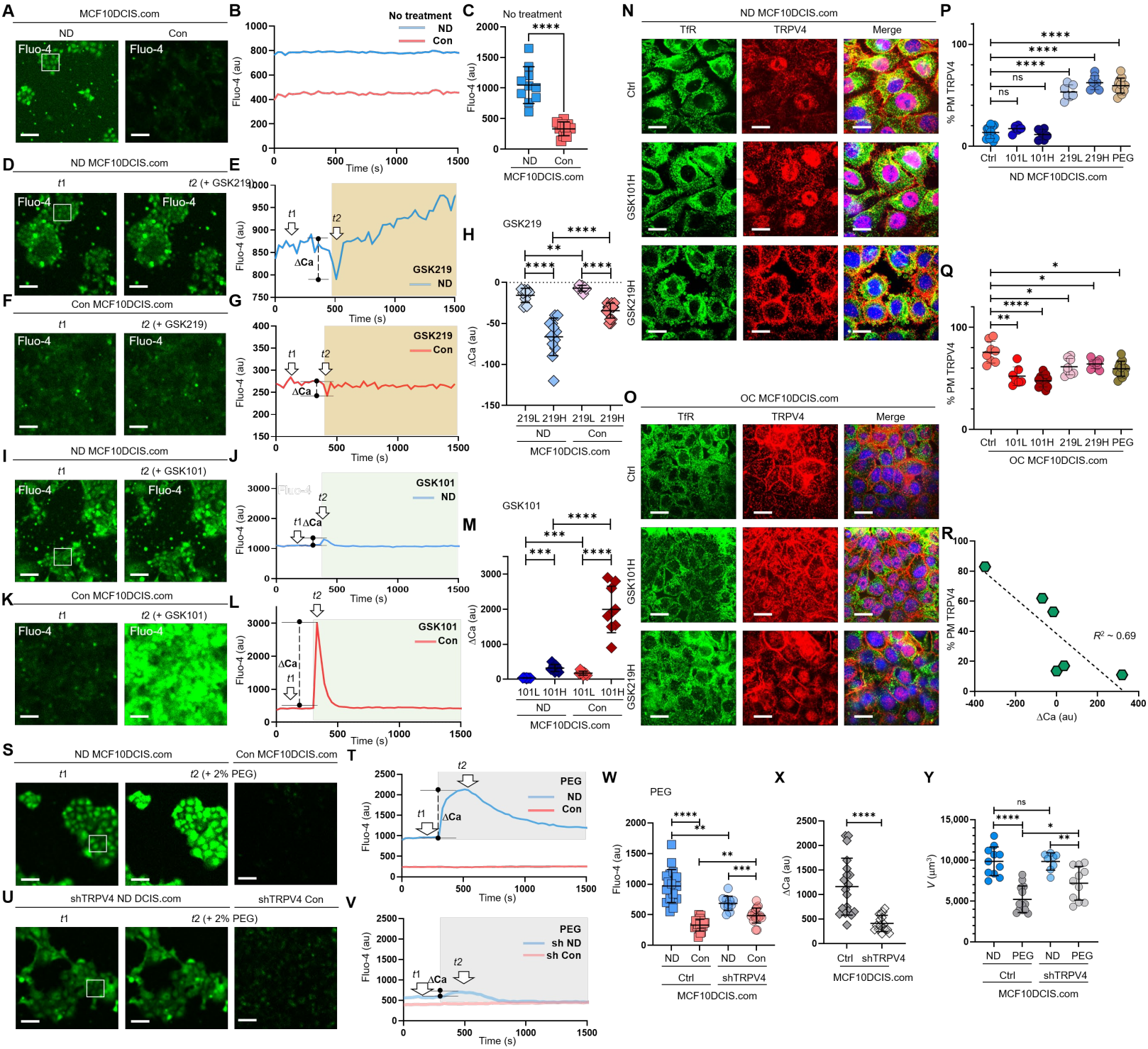

Figure 4. Cell crowding inhibits ion channels and triggers their plasma membrane relocations. (A) To compare intracellular calcium (Ca^{2+}) levels, we used a Fluo-4 AM assay,

where green fluorescence intensity increases with higher intracellular Ca^{2+} levels. Calcium levels are significantly lower in confluent (Con) MCF10DCIS.com cells. **(B)** The temporal progression of averaged Fluo-4 intensity in ND MCF10DCIS.com cells (blue curve) in the box shown on the left image is compared with that of Con cells (red curve). Fluo-4 intensity is consistently lower in Con cells than in ND cells for approximately 25 minutes (200 ms acquisition time and 1 s time interval). **(C)** Fluo-4 intensity reduction due to cell crowding is significant in MCF10DCIS.com cells. **(D-H)** Pharmacological inhibition of TRPV4 with 1 nM GSK219 generates dips in the Fluo-4 signal. Fluo-4 images at the baseline (t_1) and the dip (t_2) post 1 nM GSK219 are compared in MCF10DCIS.com cells between ND **(D)** and Con **(F)** conditions. The Fluo-4 intensity time traces are compared between ND (blue; **E**) and Con (red; **G**) conditions, showing that the magnitude of the dip (marked as ΔCa) is significantly lower in Con cells, where TRPV4 activity is largely inhibited under cell crowding conditions. Notably, ΔCa increased with higher GSK219 doses (1 nM vs. 0.2 nM), but remained significantly lower in Con MCF10DCIS.com cells, with smaller changes observed under the 0.2 nM GSK219 condition. **(I-M)** TRPV4 activation with 0.2 pM GSK101 leads to a small spike in ND cells **(I, J)**. However, in Con cells, the same GSK101 treatment leads to a notable spike in Fluo-4 intensity, indicating that TRPV4 inhibition and subsequent relocation to the plasma membrane by cell crowding primes the ion channels for activation. GSK101 treatment also leads to a dose-dependent increase in the spike magnitude with higher GSK101 concentrations (0.05 pM: 101L; 0.2 pM: 101H), which is strikingly high in Con MCF10DCIS.com cells. **(N-Q)** TRPV4 activation status-dependent intracellular localization changes. **(N)** IF images of TRPV4 (red) and TfR (green) in ND MCF10DCIS.com cells show that GSK101 does not increase plasma membrane association of TRPV4. However, GSK219 significantly relocates TRPV4 to the plasma membrane in a dose-dependent manner, similar to ND cells treated with 74.4 mOsm/Kg PEG 300. **(O)** In OC cells, while GSK219 does not significantly alter TRPV4 association with the plasma membrane, GSK101 depletes plasma membrane TRPV4 in a dose-dependent manner, suggesting that TRPV4 activation status affects its trafficking. Relative plasma membrane associations with different treatments are quantified for ND **(P)** and OC **(Q)** cells using line analysis. **(R)** The magnitudes of Fluo-4 spikes by GSK101 and dips by GSK219 show a linear relationship (R^2 ~ 0.69), indicating a negative correlation between them. This reinforces the

observation that TRPV4 inhibition increases its association with the plasma membrane, while activation shows the reverse effect. **(S-V)** Compared to the Fluo-4 intensity in control MCF10DCIS.com cells **(S, T)**, shRNA showed similar Fluo-4 levels **(U, V)**. However, hyperosmotic stress by 74.4 mOsm/Kg PEG 300 (light gray box) led to a noticeable spike only in control ND cells. Additionally, cell crowding conditions (Con) led to a decreased Fluo-4 level (at t_1 baseline in the image in **S** and red time trace in **T**) and a reduction in Fluo-4 level in shRNA-treated MCF10DCIS.com cells (*t*1; **U**) compared to control cases (S, T), as shown in the image and time trace (*t*1; V). **(W)** Relative Fluo-4 time-averaged intensities are plotted for individual control ND (blue) vs. Con (red) cells, and shRNA-treated ND (semi-transparent blue) vs. Con (semi-transparent red) cells. Intracellular calcium levels in shRNA ND cells are lower than those in control ND cells, reflecting the reduced number of TRPV4 channels. The decrease in calcium levels by crowding (Con) in shRNA cells is clearly lower than in control cells, reflecting the importance of TRPV4 in mechanosensing cell volume reduction. **(X)** PEG 300-induced calcium spikes are significantly lower in shRNA cells (semi-transparent gray) than in control cells (gray), reinforcing TRPV4's crucial role in MCF10DCIS.com mechanotransduction. **(Y)** TRPV4 silencing significantly reduced the mechanosensing cell volume reduction effect. Control ND cells underwent a 48% volume reduction in response to 74.4 mOsm/Kg PEG 300, whereas TRPV4-silenced cells reduced their volume by only 27%.

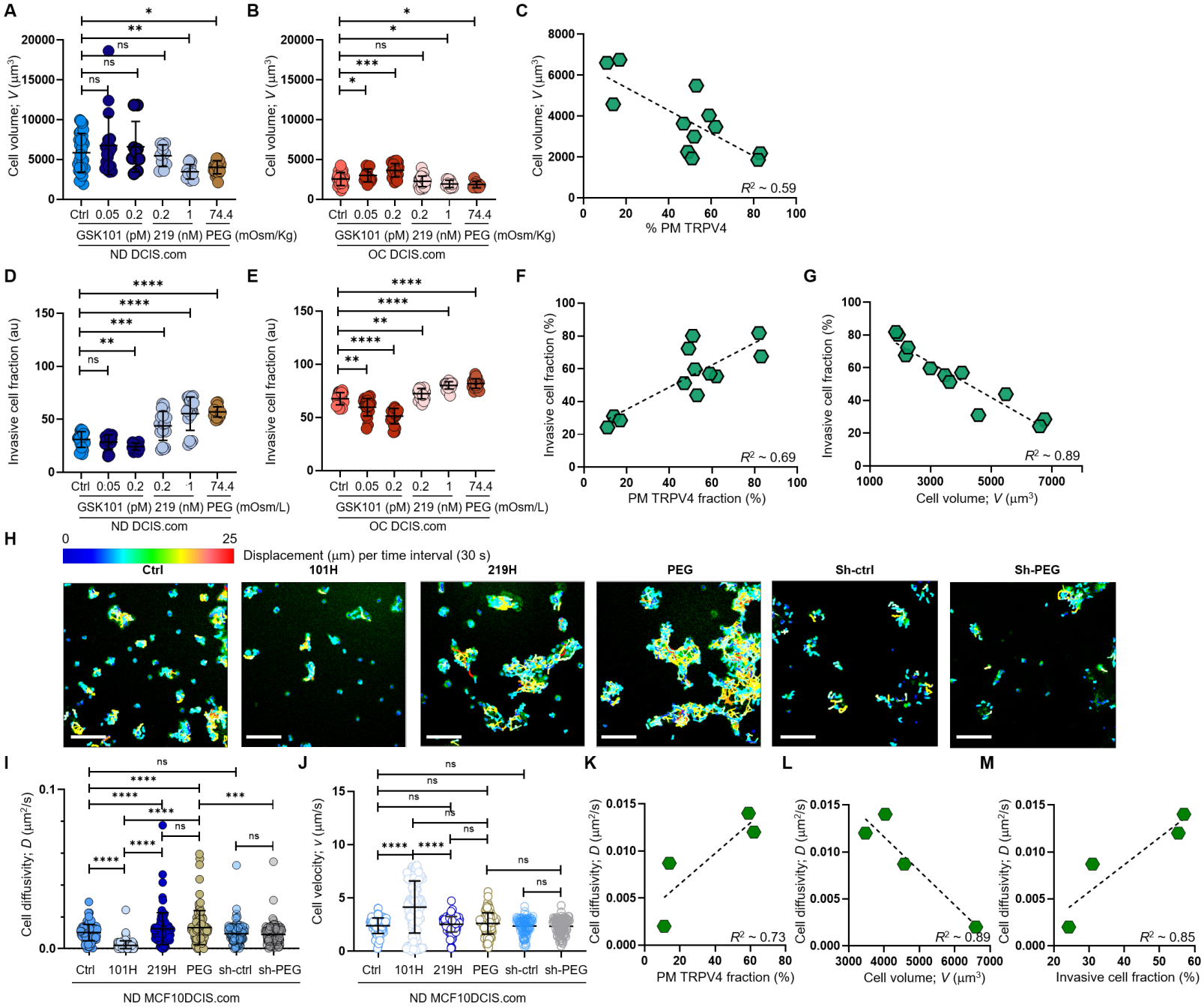

Figure 5. Cell crowding-induced plasma membrane TRPV4 association scales with cell volume reduction and increases in invasiveness and motility

A-C. MCF10DCIS.com cell volume changes with TRPV4 inhibition and activation. **(A)** In ND MCF10DCIS.com cells, GSK101, which did not alter plasma membrane association of TRPV4,

did not affect cell volume. Conversely, GSK219, which increased such association in a dose-dependent manner, reduced cell volume, with the effect of 1 nM GSK219 (219H) being similar to that of 74.4 mOsm/Kg PEG 300. **(B)** Under OC conditions, GSK101, which leads to significant Fluo-4 spikes, increased cell volume in a dose-dependent manner, while GSK219 and PEG only mildly reduced cell volume. **(C)** Cell volume changes in MCF10DCIS.com cells show an inverse relationship with plasma membrane association of TRPV4, reflecting the activation status of the channel (R^2 = 0.59). **(D-F)** Cell invasiveness increases with cell volume reduction and greater plasma membrane association of TRPV4. **(D)** Cell invasiveness significantly increases with GSK219 under ND conditions. **(E)** GSK101 under OC conditions shows a notable decrease in cell invasiveness in a dose-dependent manner. **(F)** Plasma membrane association of TRPV4 predictably reports cell invasiveness (R^2 ~ 0.69), while cell invasiveness and cell volume are inversely related, reinforcing our observation that cell volume reduction promotes cell invasiveness. **(H-M)** To assess if cell motility also follows the trend of cell invasiveness, we performed a single-cell motility assay by tracking nuclear WGA in individual live cells every 5 s for 25 min. **(H)** Representative trajectories of individual cells are color-coded to reflect displacement at each time interval. Compared to untreated ND cells, 0.2 pM GSK101 treatment slowed overall cell diffusion, while 1 nM GSK219 and 74.4 mOsm/Kg PEG 300 treatments increased cell diffusion. ShRNA TRPV4 (Sh-ctrl) had no effect on cell motility under ND conditions. Furthermore, treatment with 74.4 mOsm/Kg PEG 300 failed to increase cell diffusivity (D) in shRNA-treated cells (Sh-PEG). Scale bar = 200 μm. Using single-cell analysis, we quantified cell diffusivity (D) and speed (v; movement directionality). **(I)** GSK101 treatment significantly reduced D, while GSK219 and PEG 300 notably increased D. ShRNA TRPV4 did not alter ND cell D. **(J)** GSK101 treatment increased v, while GSK219 and PEG treatments significantly increased D but those did not affect directionality. ShRNA ND cell directionality remained similar to that of control cells and was unchanged by PEG treatment. **(K)** Like cell invasiveness, cell motility (D) positively scales with plasma membrane association of TRPV4 (R^2 ~ 0.73). **(L)** Cell motility (D) inversely

relates to cell volume ($R^2 \sim 0.89$). **(M)** Cell motility (*D*) and cell invasiveness show a strong linear relationship ($R^2 \sim 0.85$), enabling the use of cell motility measurements to assess overall cell invasiveness.

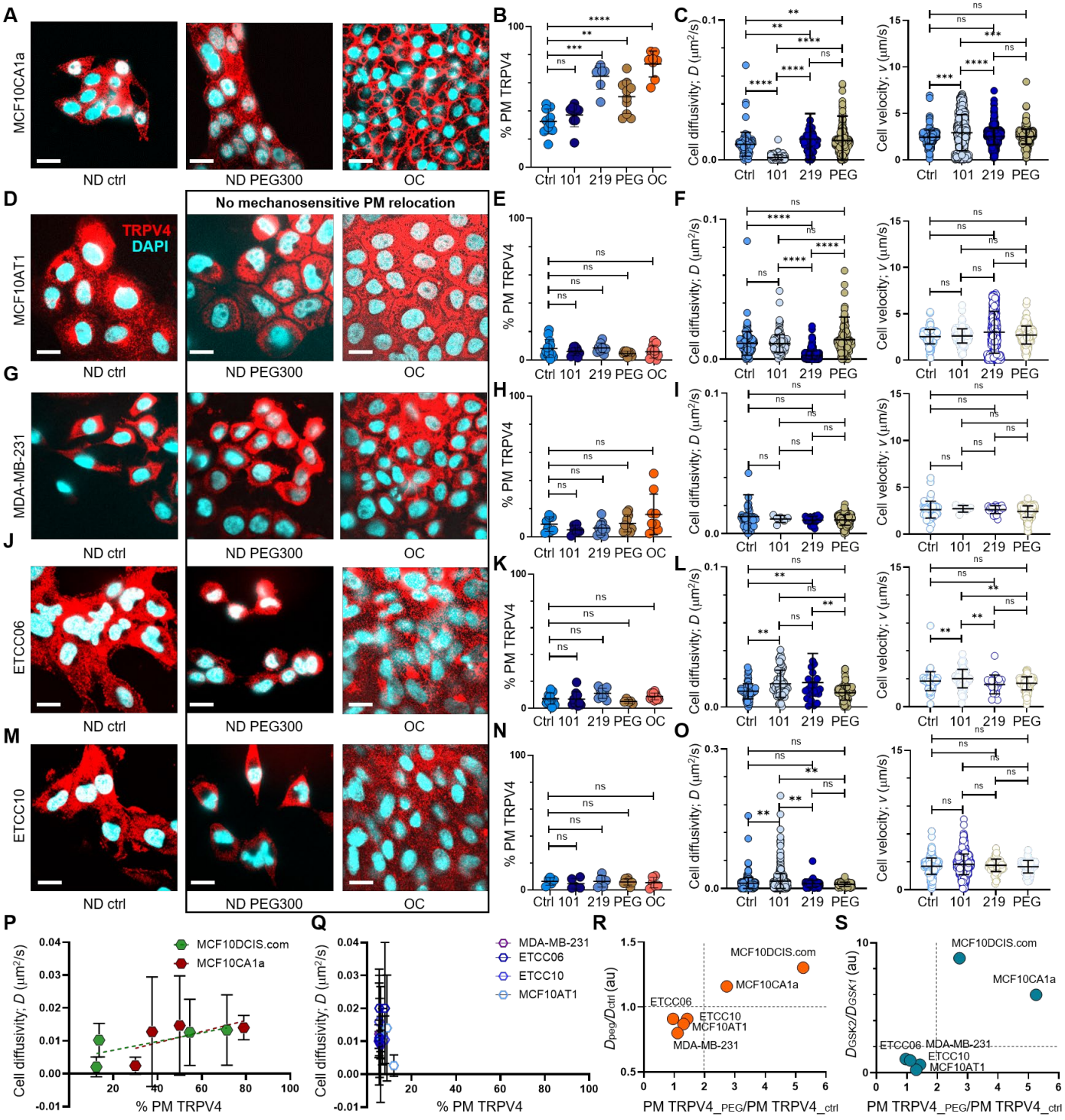

Figure 6. Pro-invasive cell volume reduction mechanotransduction pathway is indicated by TRPV4 inhibition and hyperosmotic stress-driven increases in TRPV4 association with the plasma membrane and cell motility, as well as TRPV4 activation-induced decreases in

cell motility. (A) MCF10CA1a cells respond to 15 minutes of PEG 300 (74.4 mOsm/kg) and OC conditions by relocating TRPV4 to the plasma membrane, increasing the channel's association with the membrane. IF images show a predominantly intracellular TRPV4 (red) distribution in the ND control MCF10CA1a cells, whereas plasma membrane association of TRPV4 occurs in response to PEG 300 and OC. DAPI (blue) staining indicates the nucleus. Scale bars throughout Fig. 6 = 10 μm. **(B)** Line analysis results of plasma membrane-associated TRPV4 (%) show significant increases in plasma membrane TRPV4 (PM TRPV4) with 1 hour of GSK219 (1 nM), 15 minutes of 74.4 mOsm/kg PEG 300, and OC conditions. **(C)** Cell movement diffusivity (*D*) increases with GSK219 and PEG treatments, while movement directionality (*v*) increases with GSK101 (0.2 pM) but shows no other effects. **(D-O)** MCF10AT1 **(D, E)**, MDA-MB-231 **(G, H)**, ETCC-06 **(J, K)**, and ETCC-10 **(M, N)** do not relocate TRPV4 to the plasma membrane in response to TRPV4 inhibition by GSK219, hyperosmotic conditions by PEG-300, or OC conditions, as evidenced by IF images (TRPV4: red; DAPI: blue) and line analysis results for plasma membrane associations of TRPV4. **(F)** None of these cells' motility responded to PEG 300. However, their responses to TRPV4 activation (GSK101) and inhibition (GSK219) varied, suggesting different roles of TRPV4 in their cancer biology. MCF10AT1 diffusivity (*D*) significantly reduced with GSK219, while the rest of the conditions did not affect *D*. Movement directionality (*v*) was not affected by any treatment conditions. **(G)** MDA-MB-231 cell *D* or *v* did not alter with any treatment conditions, suggesting an insignificant role of TRPV4 in their cell motility. **(L, M)** Both ETCC-06 and ETCC-10 *D* increased with GSK101, but GSK219 also increased ETCC-06 diffusivity, while not altering ETCC-10 diffusivity. ETCC-06 directionality (*v*) increased with GSK101, but ETCC-10 directionality remained unchanged. **(P)** Plasma membrane association of TRPV4 (% PM TRPV4) positively scalex with cell movement *D* over a larger range for MCF10DCIS.com cells than for MCF10CA1a, reflecting the high cell volume plasticity observed in MCF10DCIS.com cells. This result suggests that both cell types have a pro-invasive mechanotransduction pathway. **(Q)** Such scaling is absent in MCF10AT1, MDA-MB-231, ETCC-

06, and ETCC-10 cells. **(R)** The presence of such a mechanotransduction pathway is observed for MCF10CA1a and MCF10DCIS.com cells from the plot of greater than 2-fold increase in plasma membrane association of TRPV4 (x-axis; PM TRPV4_peg/PM TRPV4_ctrl) and greater than 1-fold increase in diffusivity (y-axis; *D*peg/*D*ctrl) by PEG-300. **(S)** Cell volume reduction-mediated mechanotransduction pathway can be clearly observed from plotting plasma membrane association of TRPV4 (x-axis) and relative increase in diffusivity with GSK101 versus GSK219 (y-axis), which are significantly greater than 2 for MCF10CA1a and MCF10DCIS.com cells.

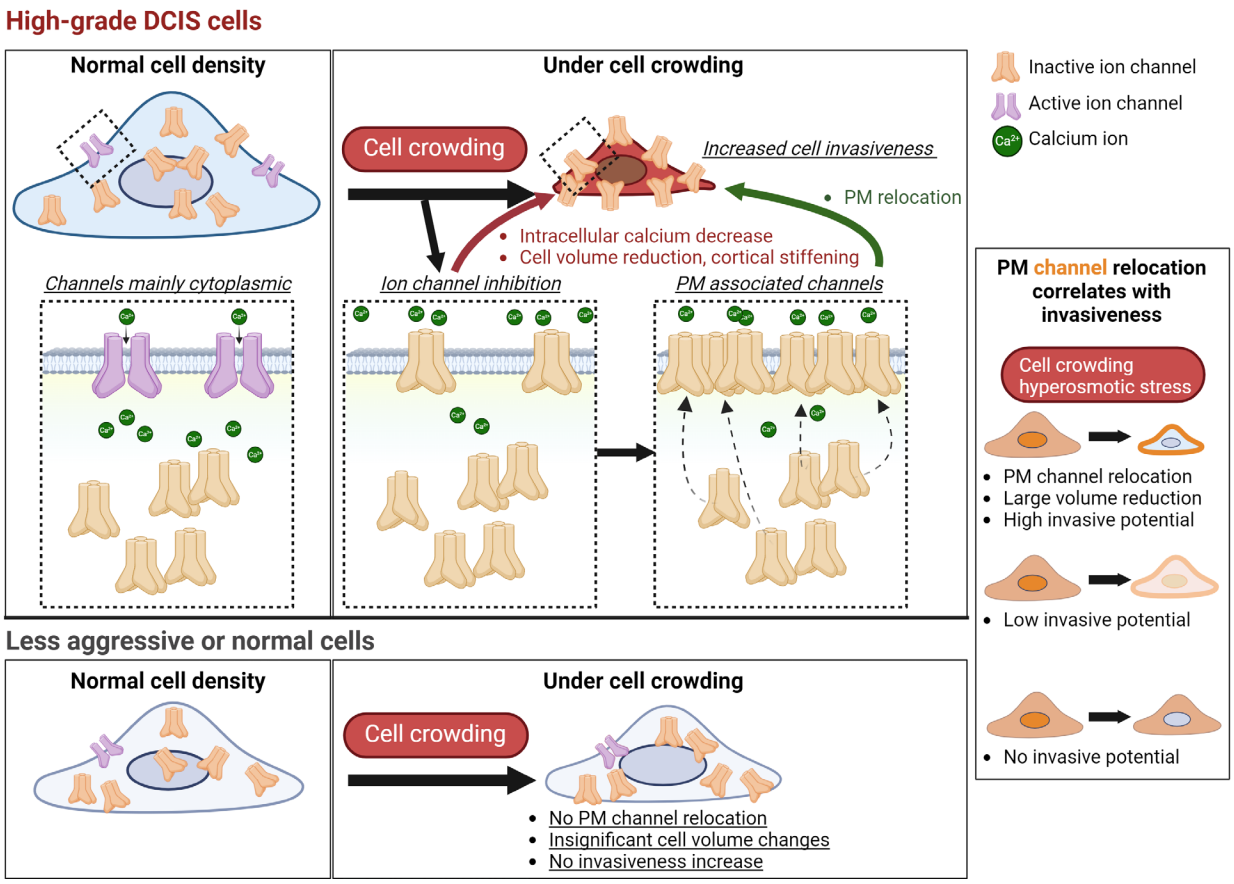

Figure 7. Cell crowding triggers the activation of a pro-invasive mechanotransduction pathway in high-grade DCIS cells but not in less aggressive or normal cells. This pro-invasive mechanotransduction pathway involves cell volume reduction and cortical stiffening driven by ion channel inhibition. Ion channel inhibition leads to the relocation of ion channels to the plasma membrane (PM). Under ND conditions, ion channels are mainly cytoplasmic in both high-grade DCIS and less aggressive/normal cells. However, high-grade DCIS cells have a larger cell volume under ND conditions. Cell crowding induces ion channel inhibition, leading to decreased intracellular calcium and subsequent cell volume reduction, which correlates with increased invasiveness. In contrast, less aggressive and normal cells do not exhibit this response. The inset image shows that mechanosensitive plasma membrane relocation of ion channels (orange) scales with increased invasiveness due to the activation of the cell volume reduction

mechanotransduction pathway, while the absence of relocation indicates no mechanosensitive invasive increase.

Cell crowding induces TRPV4 inhibition and its relocation to plasma membranes, implicating pro-invasive cell volume reduction mechanotransduction pathway

Xiangning Bu[1], Nathanael Ashby[1], Teresa Vitali[1], Sulgi Lee[1], Ananya Gottumukkala[1,2], Kangsun Yun[1], Sana Tabbara[3,†], Patricia Latham[3], Christine Teal[4], Inhee Chung[1,5*]

Affiliations:

1 Department of Anatomy and Cell Biology, School of Medicine and Health Sciences, George Washington University, Washington, DC, USA

2 Thomas Jefferson High School for Science and Technology, Alexandria, VA, USA

3 Department of Pathology, George Washington Medical Faculty Associates, Washington, DC, USA

4 Department of Surgery, George Washington Medical Faculty Associates, Washington, DC, USA

5 Department of Biomedical Engineering, GW School of Engineering and Applied Science, George Washington University, Washington, DC, USA

† Current address: Department of Pathology, H. Lee Moffitt Cancer Center and Department of Oncologic Sciences, University of South Florida Morsani College of Medicine, Tampa, FL, USA

* Correspondence to: inheec@gwu.edu

Supplementary information

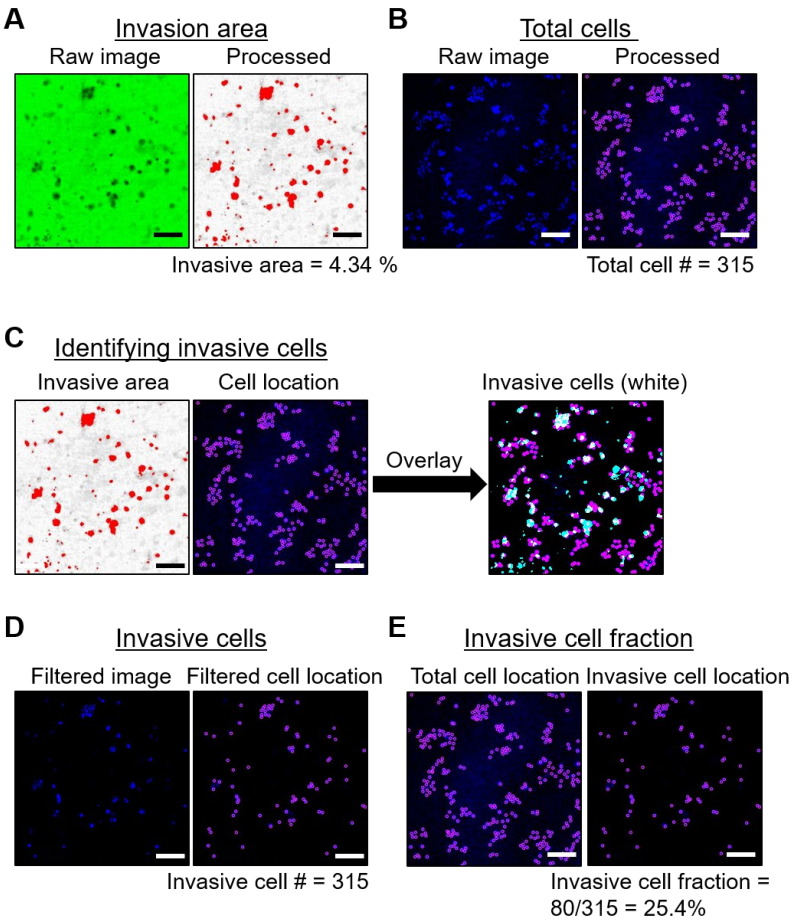

Supplementary Figure 1. Quantifying the Invasive cell fraction using a 2D polyacrylamide hydrogel-based invasion assay. (A) Green fluorescent gelatin images were thresholded to highlight invasion areas (in red) due to degradation (visible as dark regions in the original image). Here, 4.34% of the total area indicated cell invasion. **(B)** DAPI images (in blue, showing nuclei locations) were processed with the Trackmate plugin in Image J to detect individual DAPI spots (displayed in purple). The total cell count in this instance was estimated at 315. **(C)** The highlighted invasive areas from **(A)** served as masks for the DAPI locations, selecting only the invasive cells (those in the white regions resulting from the overlay between cell positions in purple and invasive zones in cyan). **(D)** The resultant images display the locations of invasive cells in purple. The invasive cell count from this image was 80. **(E)** The fraction of invasive cells was determined by

comparing the number of invasive cells (from **D**) with the overall cell count (from **B**). Thus, the invasive cell fraction was 25.4% (80 out of 315). Scale bar = 100 μm.

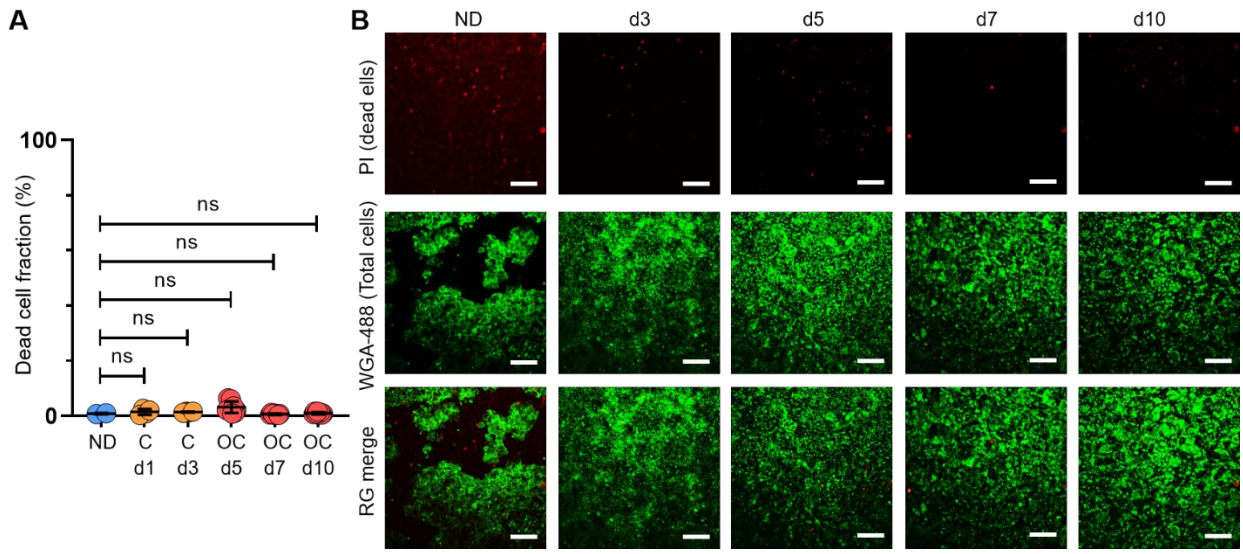

Supplementary Figure 2. MCF10DCIS.com cells exhibited comparable viability under OC conditions to those under ND conditions. (A-B) Live cells seeded at ND (~70%) (n=2) were cultured for 1 (n=4), 3 (n=4), 5 (n=8), 7 (n=8), and 10 (n=8) days post-confluence (denoted as "d"). Cells were stained with propidium iodide (PI, red) to mark dead cells, followed by WGA-488 (green) to label nuclei. After staining, cells were fixed and imaged using confocal microscopy (4X), with red and green signals quantified via the TrackMate plugin in ImageJ. The percentage of dead cells, based on PI-positive signals, is presented in **A**. Both confluent (day 1 and day 3) and OC (day 5–10) MCF10DCIS.com cells showed similar viability to ND cells, with less than 1% cell death (0.85 ± 0.25%). On average, the fraction of dead cells was 1.58 ± 0.98%, confirming that cell crowding does not additionally induce cell death. Representative PI/WGA-488/merged images from days 1, 3, 5, 7, and 10 are shown in **B.** Scale bar = 100 μm. For the t-test, we employed a nonparametric approach using the Mann-Whitney test with a two-tailed p-value, which was used throughout the manuscript. The statistical significance levels are denoted as follows: ****: $p < 0.0001$, ***: $p < 0.001$, **: $p < 0.01$, *: $p < 0.05$, ns: $p > 0.05$.

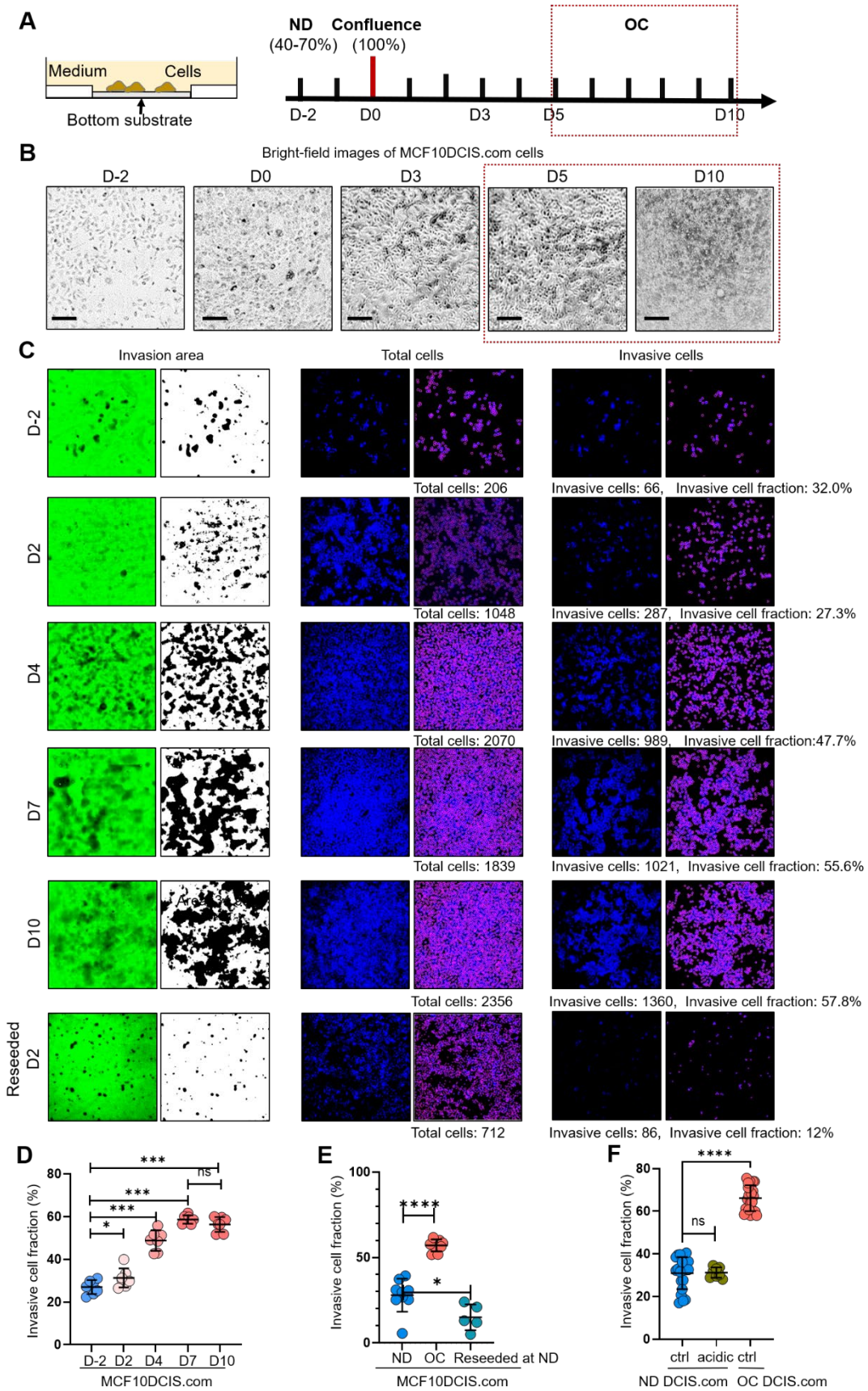
A
Medium
Cells
Bottom substrate
ND
(40-70%)
Confluence
(100%)
OC
D-2
D0
D3
D5
D10
B
Bright-field images of MCF10DCIS.com cells
D-2
D0
D3
D5
D10
C
Invasion area
Total cells
Invasive cells
D-2
Total cells: 206
Invasive cells: 66, Invasive cell fraction: 32.0%
D2
Total cells: 1048
Invasive cells: 287, Invasive cell fraction: 27.3%
D4
Total cells: 2070
Invasive cells: 989, Invasive cell fraction:47.7%
D7
Total cells: 1839
Invasive cells: 1021, Invasive cell fraction: 55.6%
D10
Total cells: 2356
Invasive cells: 1360, Invasive cell fraction: 57.8%
Reseeded D2
Total cells: 712
Invasive cells: 86, Invasive cell fraction: 12%
D
Invasive cell fraction (%)
D-2 D2 D4 D7 D10
MCF10DCIS.com
E
Invasive cell fraction (%)
ND OC Reseeded at ND
MCF10DCIS.com
F
Invasive cell fraction (%)
ctrl acidic ctrl
ND DCIS.com OC DCIS.com

Supplementary Figure 3. Time window for cell crowding conditions in vitro. (A) MCF10DCIS.com cells were grown to: normal density (ND; 40%–70%), confluence (100%), and overconfluence (OC). The time points for these growth stages were two days before confluence (D-2) for ND, day 0 (D0) for confluence, and days 5–10 after confluence (D5) for OC. We selected the cell crowding condition (OC conditions) during days 5–10 as cell morphology (**B**) and invasiveness (**C**) reached equilibrium after day 5. **(B)** Brightfield microscopy images of MCF10DCIS.com cells on the indicated days. Cells exhibited significant compaction starting from day 5. Scale bar = 100 μm. (**C-D**) Time-dependent invasiveness of MCF10DCIS.com cells as they progressed to OC. The cell invasiveness increased until day 5 and plateaued between days 5 and 10. When these cells were reseeded at normal density on day 2 (reseeded D-2), their invasiveness decreased to levels similar to the original ND cells. **(E)** Formerly OC cells reseeded at ND showed a slight reduction in the fraction of invasive cells (light teal circles) to approximately 15%, comparable to ND cells (blue circles) before exposure to OC conditions. These results suggest that the OC-induced increase in invasiveness is largely reversible. **(F)** To test if acidity of OC cell media, despite frequent changing, contributed to increased invasiveness of DCIS.com cells, we used acidic OC media (day 7) to treat ND DCIS.com cells for two days. Conditioned media did not alter invasiveness of ND DCIS.com cells. For the t-test, we employed a nonparametric approach using the Mann-Whitney test with a two-tailed p-value, which was used throughout the manuscript. The statistical significance levels are denoted as follows: ****: $p < 0.0001$, ***: $p < 0.001$, **: $p < 0.01$, *: $p < 0.05$, ns: $p > 0.05$.

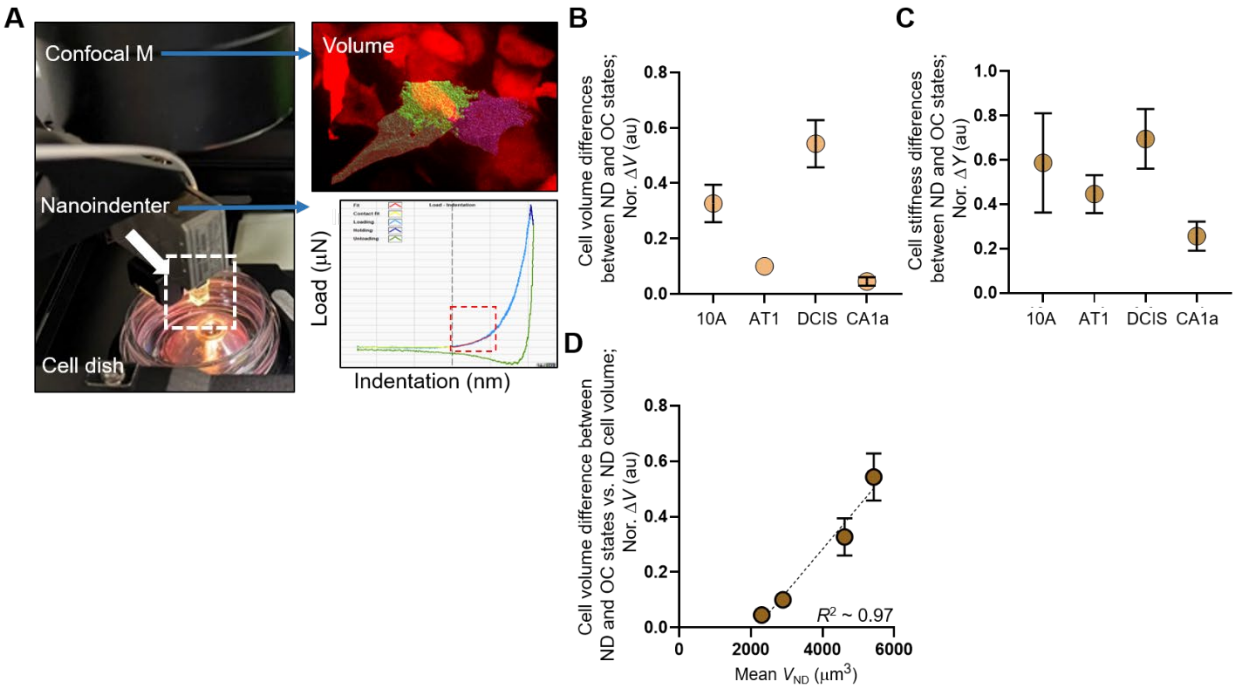

Supplementary Figure 4. Increased invasiveness of MCF10DCIS.com cells correlates with cell volume plasticity, not the acidity of cell media. (A) Cell crowding induced cell volume and stiffness changes assessed by our confocal microscope, which captures 3D volume of single RFP-expressing cells (right image) and includes a nanoindenter device (Chiaro, Optics11life) that can indent a single cell (load vs indentation curve) to extract Young's modulus in the elastic regime (red dashed box) using a Hertzian model. The indentation probe has a spring constant and tip diameter of ~0.24 N/m and 10 μm, respectively. We confirmed that RFP expression did not alter cell volume. **(B-C)** Cell volume and stiffness differences between ND and OC conditions calculated using the cell volume and stiffness data in Fig. 2A and 2C were normalized to the ND cell volume **(B)** or stiffness **(C)**, with the highest changes observed in high-grade MCF10DCIS.com cells. **(D)** Normalized volume change (Nor. Δ*V*) linearly scaled with ND cell volume (mean V_{ND}), with an R^2 value of approximately 0.97, signifying a highly linear relationship. ****: $p < 0.0001$, ***: $p < 0.001$, **: $p < 0.01$, *: $p < 0.05$, ns: $p > 0.05$.

Gene names MCF10DCIS.com cells	Protein Name	OC/ND ratio
TRPV4	Transient Receptor Potential Vanilloid 4	153.01
IVL	Involucrin	55.35
SCN11A;SCN5A;SCN10A;SCN9A	Sodium Voltage-Gated Channel Alpha Subunit 11; Sodium Voltage-Gated Channel Alpha Subunit 5; Sodium Voltage-Gated Channel Alpha Subunit 10; Sodium Voltage-Gated Channel Alpha Subunit 9	41.82
HNRNPM	Heterogeneous Nuclear Ribonucleoprotein M	26.91
COPG2	Coatomer Protein Complex Subunit Gamma 2	18.33
S100P	S100 calcium-binding protein P	18.01
MRPL16	Mitochondrial Ribosomal Protein L16	14.43
IDH2	Isocitrate Dehydrogenase [NADP] Mitochondrial	8.68
EML4	Echinoderm Microtubule-Associated Protein-Like 4	7.94
GSN	Gelsolin	7.89
CKAP4	Cytoskeleton-Associated Protein 4	7.82
PRSS8	Serine Protease 8	6.93
MFI2	Melanotransferrin	6.85
CEACAM1	Carcinoembryonic Antigen-Related Cell Adhesion Molecule 1	6.84
ADGRL3;LPHN3	Adhesion G protein-coupled receptor L3; Latrophilin-3	6.82
HNRNPC	Heterogeneous Nuclear Ribonucleoprotein C	6.78
RPL7L1	Ribosomal Protein L7-Like 1	6.54
NDUFV1	NADH:Ubiquinone Oxidoreductase Core Subunit V1	6.19
HIST1H2AJ;HIST1H2AH;H2AFJ;HIST1H2AD;HIST1H2AG;HIST2H2AC;HIST2H2AA3;H2AFX	Histone H2A family	6.07
GTF2I	General Transcription Factor II-I	5.88
ERP44	Endoplasmic Reticulum Protein 44	5.81
KCNN4	Potassium Intermediate Conductance Calcium-Activated Channel 4	5.61
NDUFB9	NADH:Ubiquinone Oxidoreductase Subunit B9	5.59
RPL32	Ribosomal Protein L32	5.47

Supplementary Table 1. Gene and protein names that showed more than a 5-fold increase in plasma membrane association under OC conditions relative to ND conditions in MCF10DCIS.com cells were identified by mass spectrometry. Ion channels among these are highlighted in yellow.

Gene MCF10A cells	Protein Name	OC/ND ratio	Gene MCF10AT1 cells	Protein Name	OC/ND ratio	Gene	Protein Name	OC/ND ratio
SCEL	Sciellin	5318.644	HTRA2	High temperature requirement A2	7.36	ACAA2	Acetyl-CoA acyltransferase 2	82.61
ALDH7A1	Aldehyde dehydrogenase 7 family member A1	3111.331	PMPCB	Peptidase (mitochondrial processing) beta	5.86	ATP2B4	Plasma membrane calcium-transporting ATPase 4	37.51
ECH1	Enoyl CoA hydratase 1	2711.839	CLPP	ATP-dependent Clp protease proteolytic subunit	5.58	LETM1	Leucine zipper-EF-hand containing transmembrane protein 1	33.35
TRAP1	TNF Receptor Associated Protein 1	1730.727				PCCB	Propionyl CoA carboxylase beta chain	33.2
ACAA2	Acetyl-CoA acyltransferase 2	1220.093				CEACAM5	Carcinoembryonic antigen-related cell adhesion molecule 5	31.27
AK3	Adenylate kinase 3	981.9458				PTPRF	Protein tyrosine phosphatase, receptor type F	24.58
UQCRC1	Ubiquinol-cytochrome c reductase core protein I	854.6939				MST1R	Macrophage stimulating 1 receptor	21.94
DCXR	Dicarbonyl/L-xylulose reductase	819.9886				CNNM3	Cyclin and CBS domain divalent metal cation transport mediator 3	21.13
SSBP1	Single-stranded DNA-binding protein 1	806.0719				SLC27A4	Fatty acid transporter 4	16.02
NDUFB6	NADH dehydrogenase [ubiquinone] 1 beta subcomplex 6	757.2265				CD70	CD70 molecule	14.53
S100A14	S100 calcium-binding protein A14	725.0331				ST14	Suppression of tumorigenicity 14 (serine peptidase)	14.45
S100A9	S100 calcium-binding protein A9	680.5115				ECHS1	Enoyl-CoA hydratase, short chain 1	13.58
S100A8	S100 calcium-binding protein A8	621.9725				PVRL4	Poliovirus receptor-related protein 4	13.28
CYB5R1	Cytochrome b5 reductase 1	583.0517				PTPRK	Protein tyrosine phosphatase, receptor type K	13.12
EPHX1	Epoxide hydrolase 1	581.6061				SPINT1	Serine peptidase inhibitor, Kunitz type 1	12.76
NDUFV1	NADH dehydrogenase [ubiquinone] flavoprotein 1	558.1863				ROBO1	Roundabout Guidance Receptor 1	12.69
COX5A	Cytochrome c oxidase subunit 5A	514.8118				NIPSNAP1	Nipsnap homolog 1	12.38
SOD2	Superoxide dismutase 2	458.5207				ITGA5	Integrin subunit alpha 5	9.31
GRHPR	Glyoxylate reductase/hydroxypyruvate reductase	440.284				ITGAV	Integrin subunit alpha V	9.23
SDHA	Succinate dehydrogenase complex, subunit A	393.8786				GOT2	Glutamate oxaloacetate transaminase 2	8.62
CS	Citrate synthase	381.1608				ALCAM	Activated leukocyte cell adhesion molecule	8.54
HSD17B10	Hydroxysteroid (17-beta) dehydrogenase 10	369.7964				TUBB2B;TUBB2A	Tubulin beta 2B class IIb; Tubulin beta 2A class IIa	7.74
ETFB	Electron transfer flavoprotein subunit beta	332.8283				PSAP	Prosaposin	7.7
NDUFA10	NADH dehydrogenase [ubiquinone] 1 alpha subcomplex 10	312.1642				SLC27A1	Fatty acid transporter 1	7.51
GOT2	Glutamate oxaloacetate transaminase 2	311.9957				KIRREL	Kin of IRRE like (Drosophila)	7.22

Supplementary Table 2. Top 25 gene and protein names that showed more than a 100-fold increase (MCF10A; light blue header) and 5-fold increases (MCF10AT1; blue header and MCF10CA1a; violet header) in plasma membrane association under OC conditions relative to ND conditions in MCF10A (left), MCF10AT1 (middle), and MCF10CA1a (right) cells were identified by mass spectrometry. One ion transporter demonstrating this behavior in MCF10CA1a cells is highlighted in yellow.

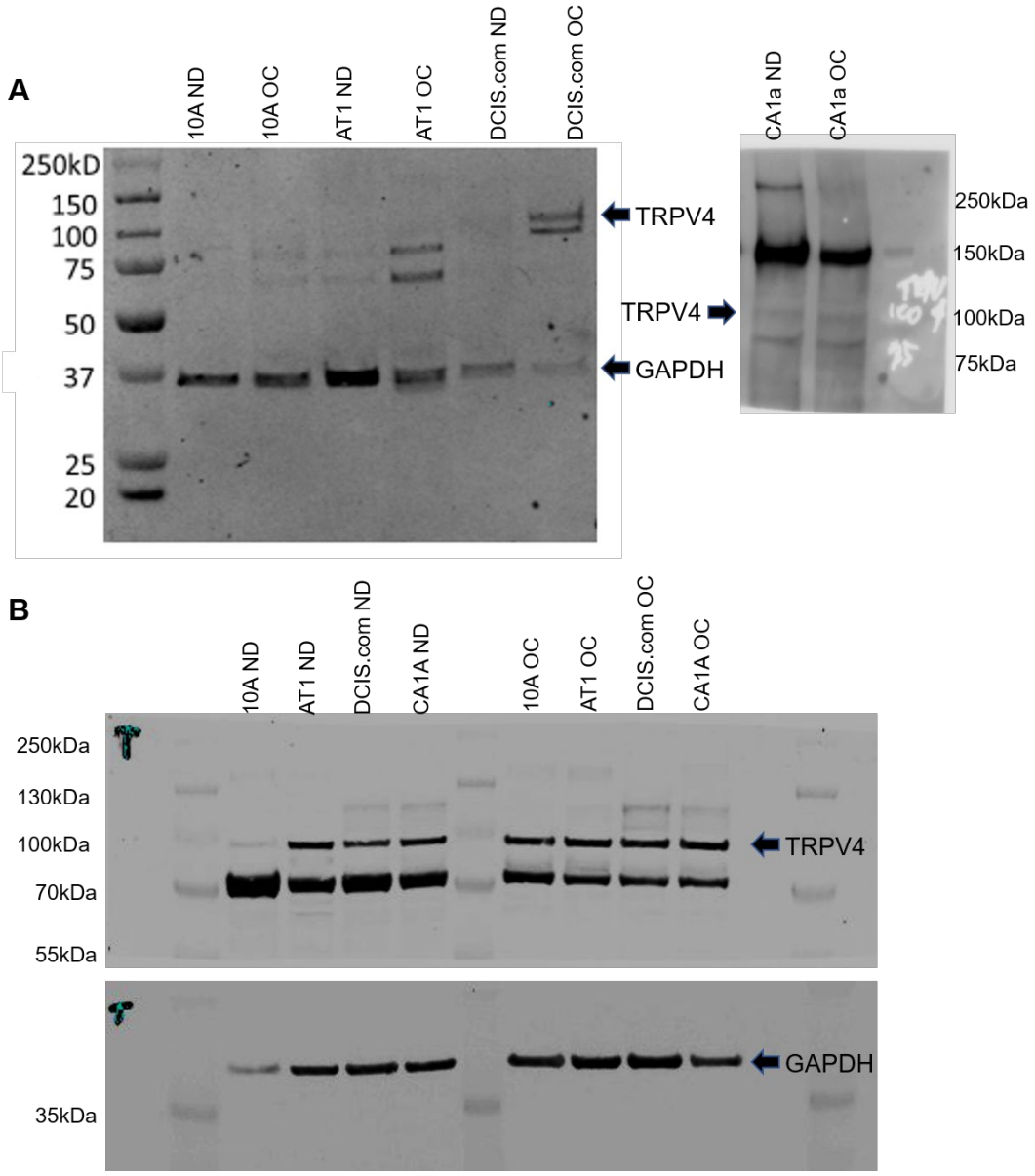

Supplementary Figure 5. Original immunoprecipitation and western blot images. (A) Left: Plasma membrane proteins pulled down after cell surface biotinylating with streptavidin beads and immunoblotted for TRPV4 and GAPDH (loading control) for ND vs OC cells of MCF10A (10A), MCF10AT1 (AT1), and MCF10DCIS.com (DCIS.com). Right: The same procedure was performed to compare PM TRPV4 between ND vs OC MCF10CA1a cells. (**B)** Overall TRPV4 protein levels from whole-cell lysates from four 10A cell derivatives. GAPDH was a loading control.

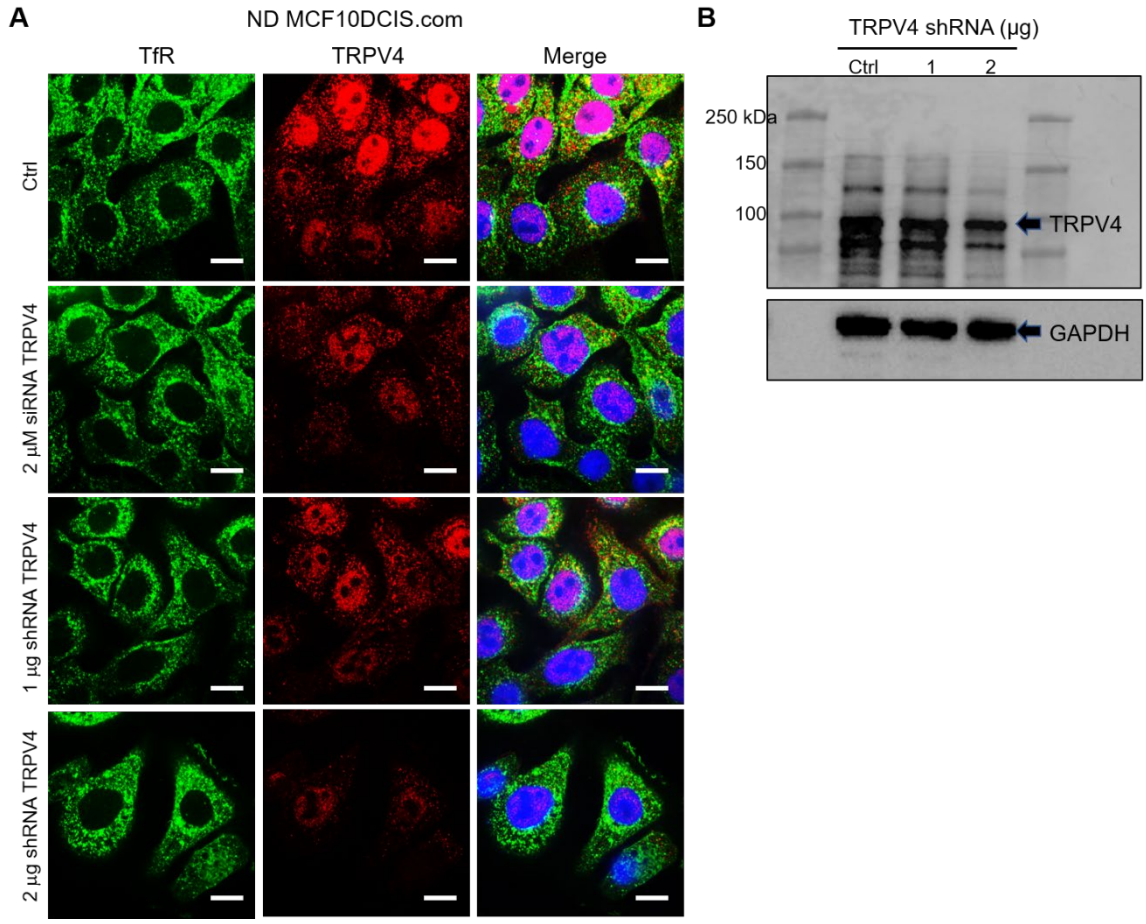

Supplementary Figure 6. Binding specificity of TRPV4 antibody. Immunofluorescence images (**A**) and immunoblots (**B**) verified the binding specificity of TRPV4 antibodies in control ND DCIS.com cells and TRPV4-depleted cells treated with either 2 μM siRNA (Dharmacon On Target Plus SMART Pool L-004195-00-0005) or 1 and 2 μg shRNA (shRNA pool, Santa Cruz sc-61726-SH) for 36 hr. (**A**) Compared to invariant transferrin receptor (TfR) staining (green), TRPV4 (red) depletion was 40% with 1 μg shRNA and 80% with 2 μg shRNA, as quantified by intensity measurements. DAPI (blue) is also shown in the merged images. All images were visualized using the same intensity settings. Scale bar = 20 μm. (**B**) Immunoblot results confirmed this dose-responsive depletion of TRPV4, with 33% reduction observed at 1 μg shRNA and 51% at 2 μg.

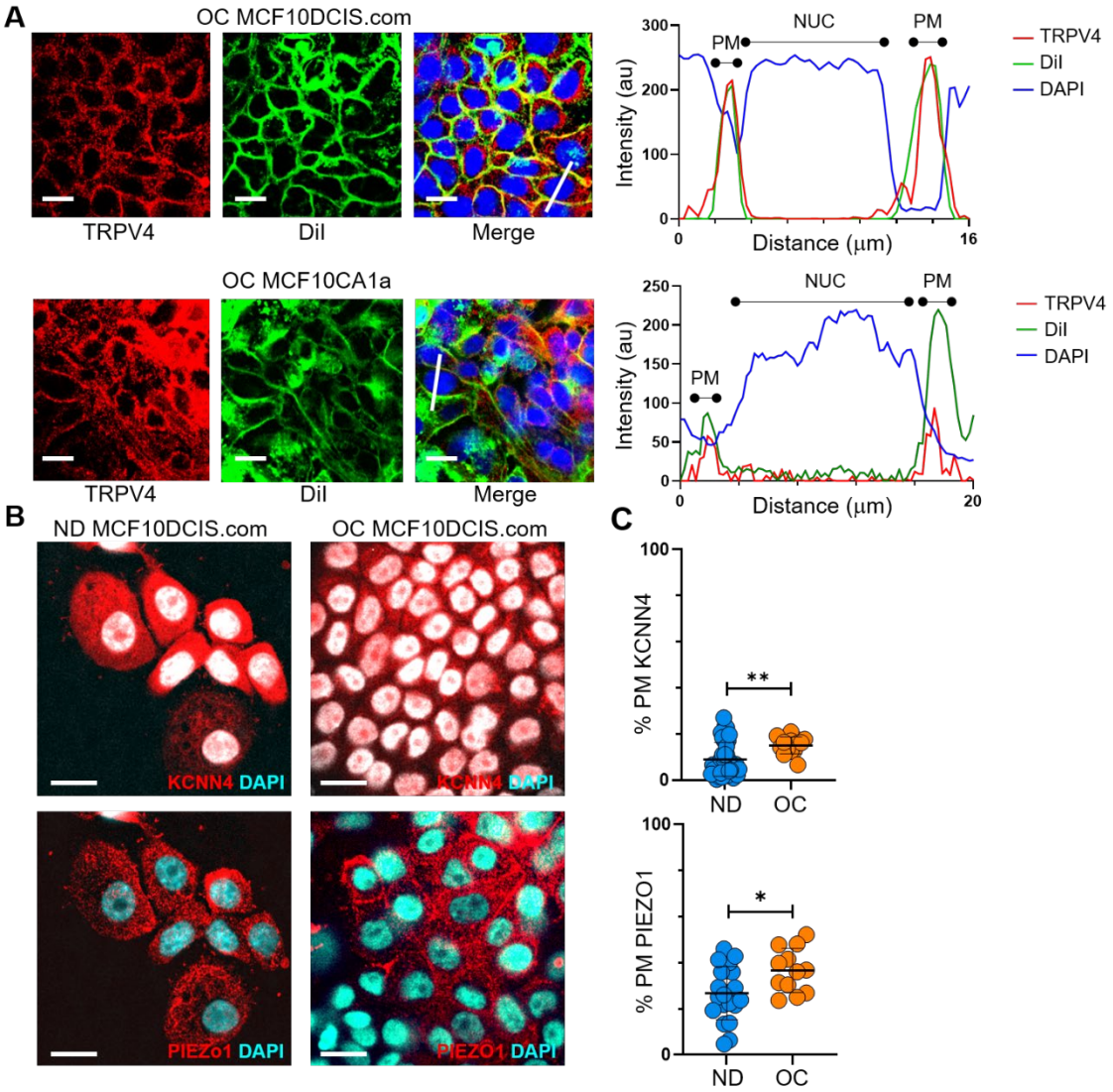

Supplementary Figure 7. Various ion channels are relocated to the plasma membrane under cell crowding conditions. (A) We used the plasma membrane marker DiIC18(3) to confirm the association of TRPV4 with the plasma membrane in MCF10DCIS.com and MCF10CA1a cells under OC conditions. As described in the Methods section, we stained DiIC18(3) in live cells and co-stained TRPV4 and DAPI in fixed and permeabilized cells. The IF images show TRPV4 (red), DiIC18(3) (DiI, green), and DAPI (blue). The line profile plots on the right demonstrate colocalization of TRPV4 with DiIC18(3) at the plasma membrane (PM), marked by the green DiIC18(3) signal, which overlaps with the red TRPV4 signal. The nucleus location (NUC) is indicated by the blue DAPI signal. Scale bar = 20 μm. (B) We examined the relocation of KCNN4

and PIEZO1 to the plasma membrane in response to cell crowding. Mass spectrometry showed a slight increase in KCNN4 at the plasma membrane under OC conditions. In ND MCF10DCIS.com cells, KCNN4 was predominantly cytosolic, whereas PIEZO1 showed some plasma membrane association. Under OC conditions, both KCNN4 and PIEZO1 showed a modest relocation to the plasma membrane. (C) Line analysis confirmed a slight increase in plasma membrane association for both KCNN4 and PIEZO1 under OC conditions compared to ND conditions. Scale bar = 20 μm. For the statistical analysis, we employed a nonparametric approach using the Mann-Whitney test with a two-tailed p-value. The levels of statistical significance are denoted as follows: **** indicates $p < 0.0001$, *** indicates $p < 0.001$, * indicates $p < 0.1$, and "ns" indicates $p > 0.05$.

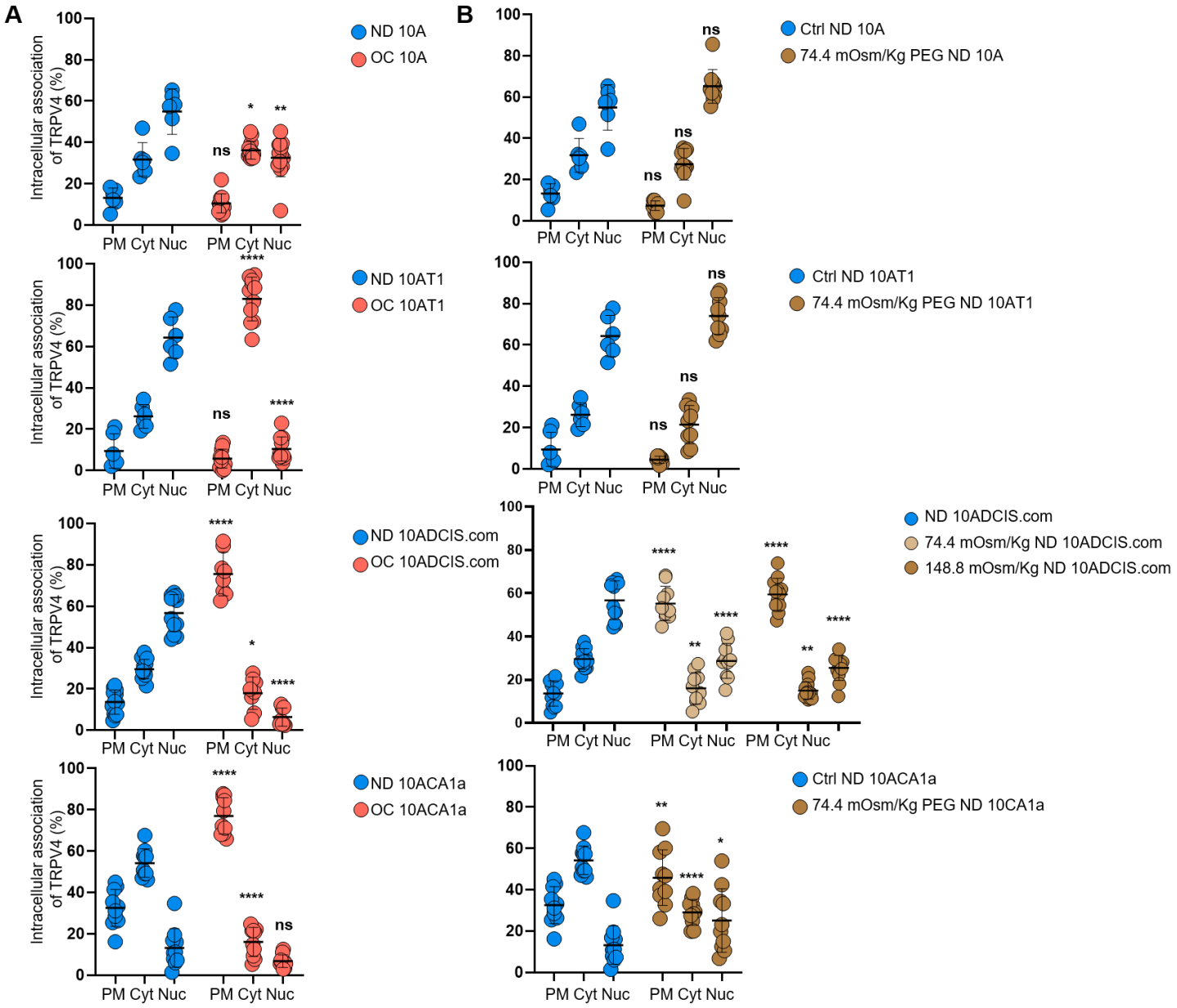

Supplementary Figure 8. Plots of the relative intracellular TRPV4 associations between ND and OC or hyperosmotic conditions in all four cell types. (A) Relative TRPV4 associations with the plasma membrane (PM), cytoplasm (Cyt), and nucleus (Nuc) are plotted for ND versus OC conditions in MCF10A (10A), MCF10AT1 (10AT1), MCF10DCIS.com (10DCIS.com), and MCF10CA1a (10CA1a) cells. **(B)** Similar analyses were performed to compare the intracellular TRPV4 associations in PM, Cyt, and Nuc between control ND and 74.4 or 148.8 mOsm/kg

PEG300 treatment groups. We employed a nonparametric approach using the Mann-Whitney test with a two-tailed p-value for the statistical analysis. The levels of statistical significance are denoted as follows: **** indicates $p < 0.0001$, *** indicates $p < 0.001$, * indicates $p < 0.1$, and "ns" indicates $p > 0.05$.

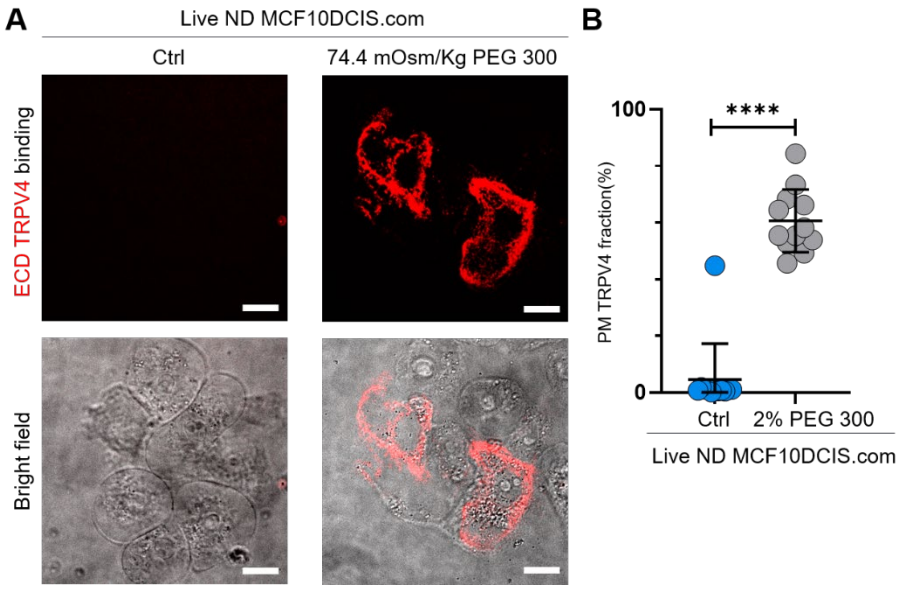

Supplementary Figure 9. Validation of mechanosensitive relocation of TRPV4 to the plasma membrane in MCF10DCIS.com cells. (A) To determine whether the seemingly plasma membrane-associated TRPV4 under hyperosmotic conditions was indeed localized at the plasma membrane of live cells, we used an extracellular domain (ECD) TRPV4 antibody. See the Methods section for sample preparation details. Live-cell imaging with 60X confocal microscopy revealed distinct binding of the ECD TRPV4 antibodies (red) exclusively in MCF10DCIS.com cells treated with 74.4 mOsm/kg PEG 300 for 15 minutes. No binding was observed in the untreated control group. Brightfield images are shown below the fluorescence images. **(B)** Line analysis demonstrated that ~60% of TRPV4 was plasma membrane-associated under 2% (74.4 mOsm/kg) PEG 300 conditions, compared to ~0% in untreated cells. Statistical analysis was conducted using a nonparametric Mann-Whitney test with two-tailed p-values. Statistical significance levels are indicated as follows: **** $p < 0.0001$, *** $p < 0.001$, * $p < 0.1$, and "ns" denotes $p > 0.05$.

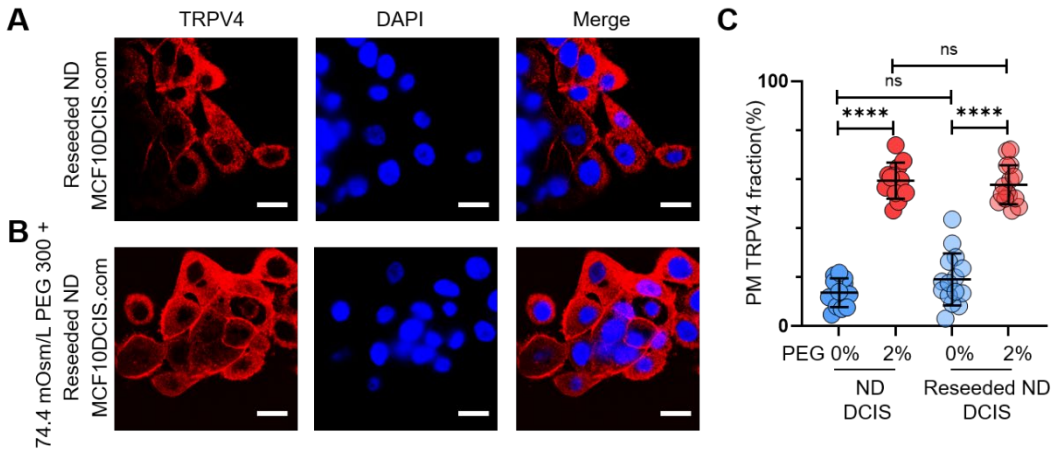

Supplementary Figure 10. Reversibility of cell-crowding-driven mechanosensing effects in MCF10DCIS.com cells. (A) Previously OC MCF10DCIS.com cells were trypsinized and reseeded under ND conditions. These cells were fixed and stained for TRPV4 (red) and DAPI (blue) for IF imaging. While TRPV4 was elevated at the plasma membrane under OC conditions, it redistributed to the cytoplasm after the cells were reseeded under ND conditions. **(B)** The reseeded ND cells responded similarly to hyperosmotic stress (74.4 mOsm/Kg PEG 300 for 15 min), with TRPV4 relocating to the plasma membrane. **(C)** Line analysis demonstrated that the reseeded ND cells exhibited a TRPV4 distribution pattern comparable to their initial ND counterparts without (blue circles) and with (red circles) hyperosmotic conditions. Statistical analysis was performed using a nonparametric Mann-Whitney test with two-tailed p-values. Statistical significance levels are denoted as follows: **** $p < 0.0001$, *** $p < 0.001$, * $p < 0.1$, and "ns" indicates $p > 0.05$.

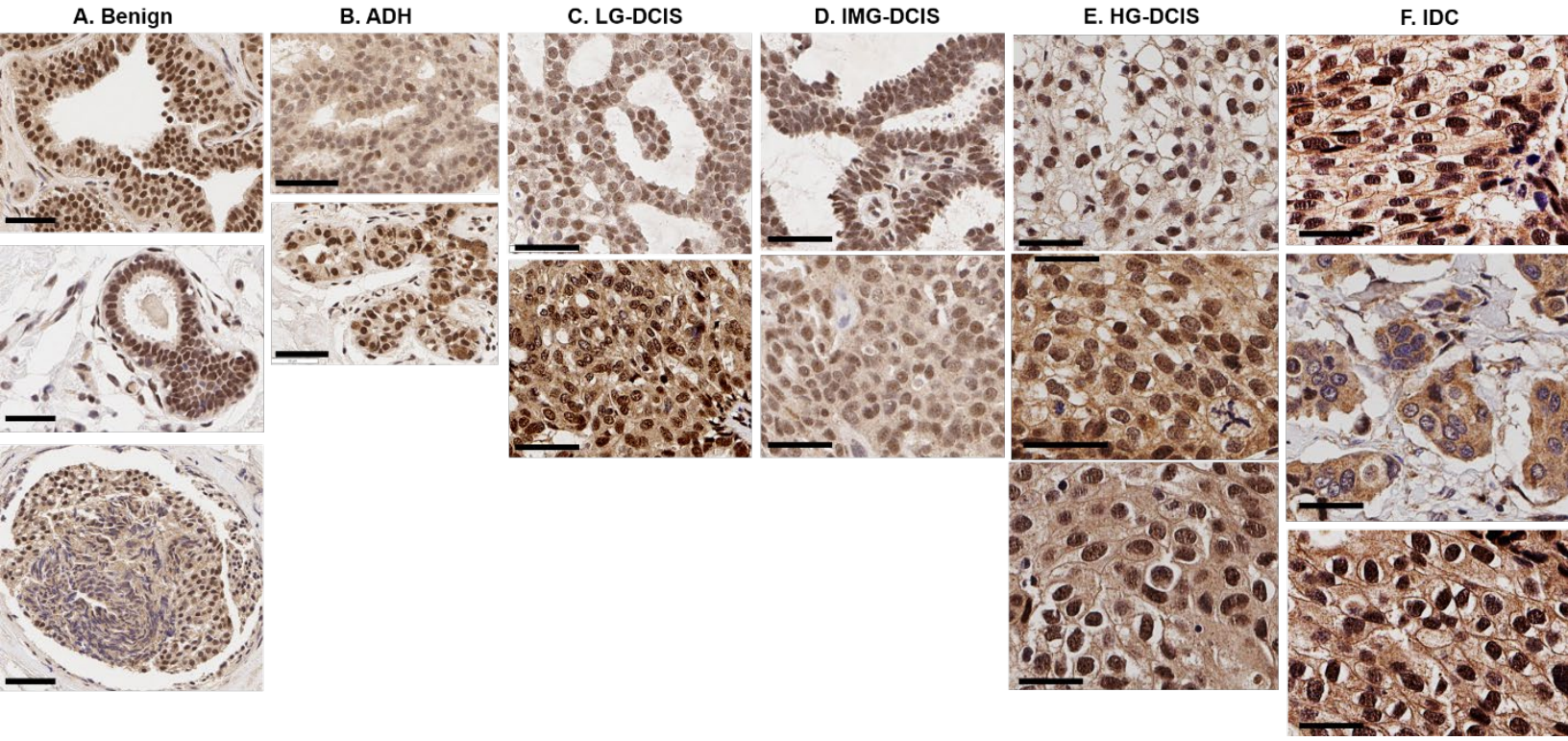

Supplementary Figure 11. Pathology-dependent differential TRPV4 distributions in patients' IHC images. Representative IHC images for each pathology from different patients are displayed. A selective presence of TRPV4 pools in the plasma membrane was mainly observed in high-grade DCIS and IDC lesions. Two pathologists independently conducted annotations. When a consensus was not reached, the case was labeled "equivocal." The cases were categorized according to the subsequent criteria:

Case 1: Absence of TRPV4.

Case 2: Intracellular TRPV4 localization.

Case 3: Presence of TRPV4 in the plasma membrane, with or without intracellular TRPV4.

A. Benign cases.

IHC images (Top): Pathology: UDH: usual ductal hyperplasia; protein distribution: case 2;

(Middle): Pathology: benign (columna); protein distribution: case 2;

(Bottom): Pathology: benign (papilloma); protein distribution: case 2.

Scale bars = 30 μm.

B. Atypical ductal hyperplasia (ADH) cases.

IHC images (Top): Pathology: ADH: usual ductal hyperplasia; protein distribution: case 2;

(Middle): Pathology: ADH: usual ductal hyperplasia; protein distribution: case 2.

Scale bars = 50 μm.

C. Low-grade (LG) DCIS cases.

IHC images (Top): Pathology: low-grade DCIS; protein distribution: case 2;

(Middle): Pathology: low-grade DCIS; protein distribution: case 2.

Scale bars = 50 μm.

D. Intermediate-grade (IMG) DCIS cases.

IHC images (Top): Pathology: intermediate-grade DCIS; protein distribution: case 2;

(Middle): Pathology: intermediate-grade DCIS; protein distribution: case 2.

Scale bars = 50 μm.

E. High-grade (HG) DCIS cases.

IHC images (Top): Pathology: high-grade DCIS; protein distribution: case 3;

(Middle): Pathology: high-grade DCIS; protein distribution: the distinction between case 2 and case 3 is equivocal;

(Bottom): Pathology: high-grade DCIS; protein distribution: case 3.

Scale bars = 50 μm.

F. Invasive ductal carcinoma (IDC) cases.

IHC images (Top): Pathology: IDC; protein distribution: case 3;

(Middle): Pathology: IDC; protein distribution: case 2.

(Bottom): Pathology: IDC; protein distribution: case 3.

Scale bars = 50 μm.

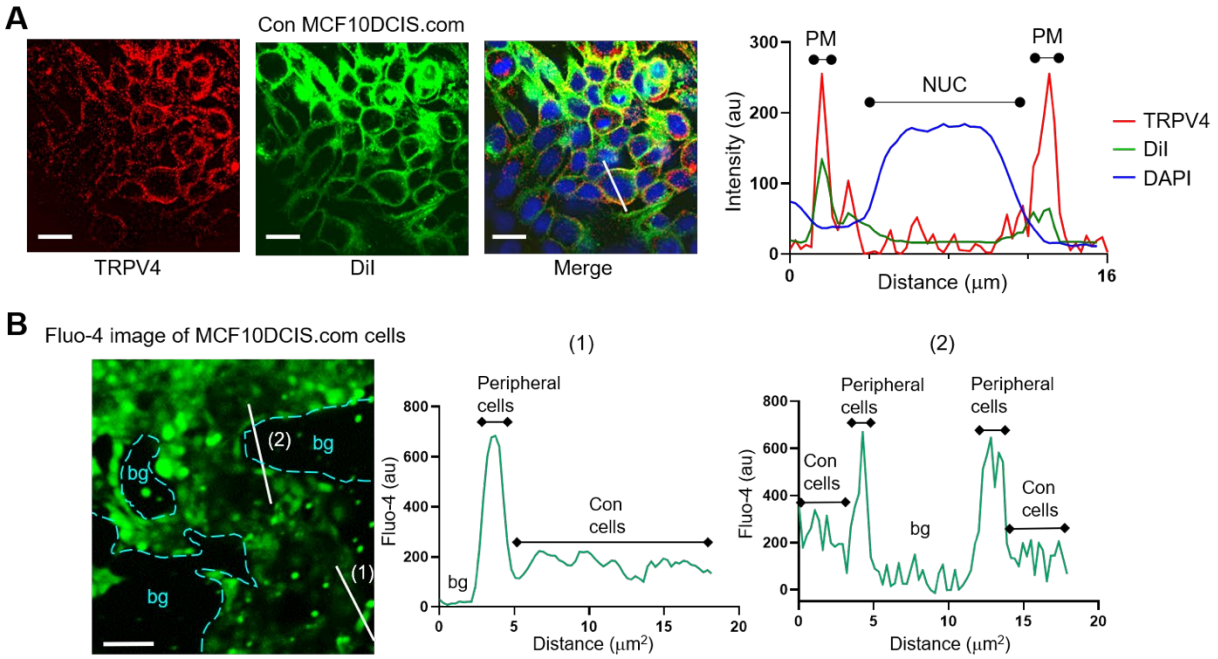

Supplementary Figure 12. Peripheral cells within MCF10DCIS.com cell clusters exhibit higher calcium levels due to reduced cell crowding effects. (A) Confluent cell density (Con) also triggered the relocation of TRPV4 (red) to the plasma membrane, similar to OC conditions, as shown in IF image (left). We used DiIC18(3) to indicate the plasma membrane location (green; DiI; middle image), and the merged image (right) of TRPV4 and DiIC18(3) shows excellent overlay at the plasma membrane (PM), as illustrated in the line profile plots from our line analysis. DAPI (blue) staining was used to locate the nucleus (NUC). Scale bar = 20 μm. **(B)** Confluent cell density resulted in lower intracellular calcium levels compared to less confluent cells. Live MCF10DCIS.com cells stained with Fluo-4 were imaged using confocal microscopy at 488 nm. Two line profiles (1, 2) crossing peripheral cells (less confluent than confluent cells) and adjacent confluent cells within the clusters clearly showed that the peripheral cells have a higher Fluo-4 signal (700 au) compared to the confluent cells within the cluster (200 au), highlighting the crowding-induced intracellular calcium reduction. Background regions (bg) were noted in cyan in the fluorescent image and in the plots. Scale bar = 100 μm.

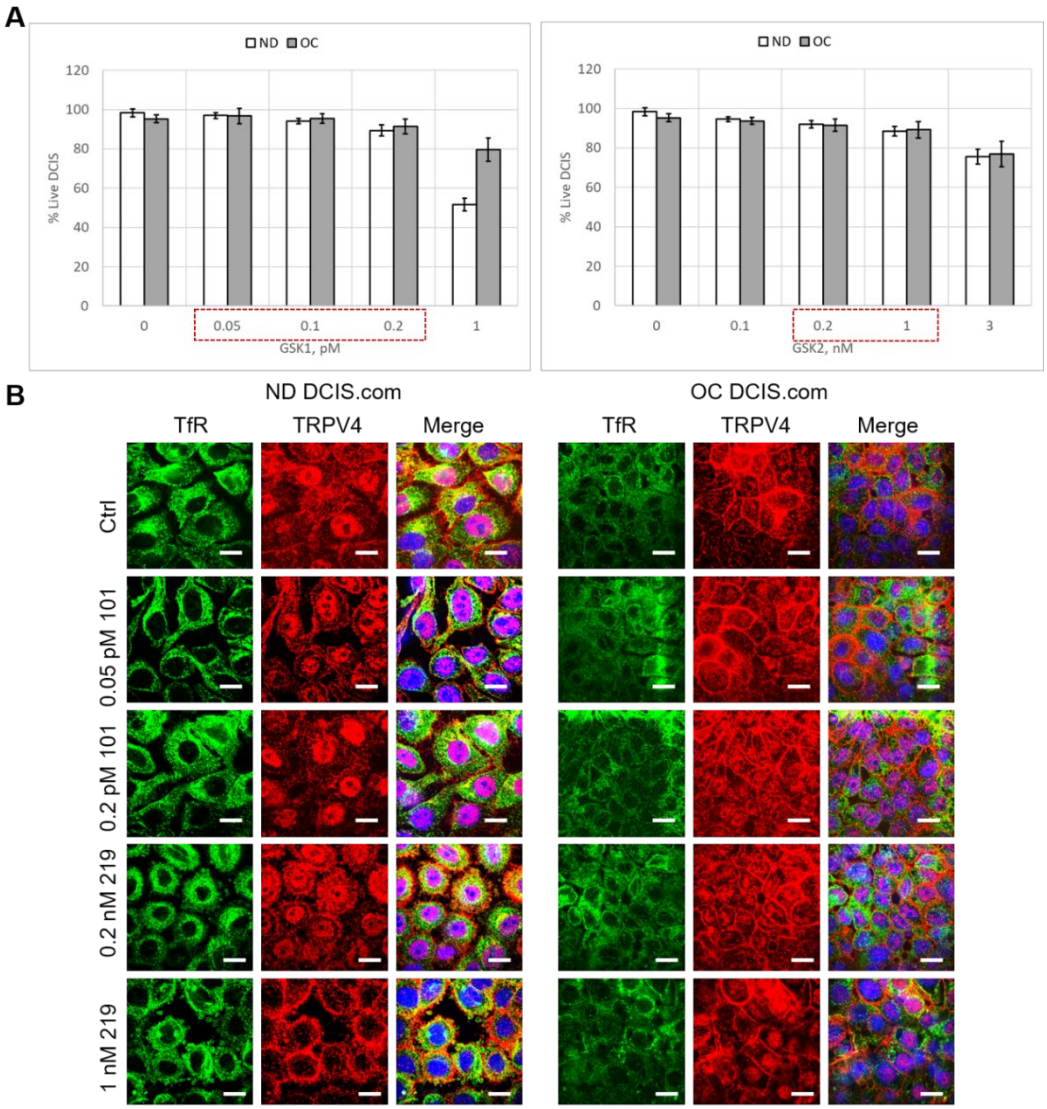

Supplementary Figure 13. Determination of treatment concentration ranges for TRPV4 activator (GSK101) and inhibitor (GSK219). (A) Cell viability assays in which viable cells were counted based on trypan blue staining after two days of GSK101 or GSK219 treatment in the specified concentration ranges of DCIS in ND (white bars) and OC (gray bars) conditions. Treatment ranges were selected so that cell viability was >90%. Concentrations used for dose-dependent assays were 0.05 and 0.2 pM for GSK101, and 0.2 and 1 nM for GSK219 (marked by dotted red boxes). **(B)** Representative confocal microscopy immunofluorescence images showed effects of GSK101 (0.05 and 0.2 pM) or GSK219 (0.2 and 1 nM) treatment for two days on TRPV4

(red) and control transferrin receptor (TfR; green) distributions in ND and OC cells in a dose-dependent manner. DAPI (blue) signal is shown in the merged images. Scale bar = 20 μm.

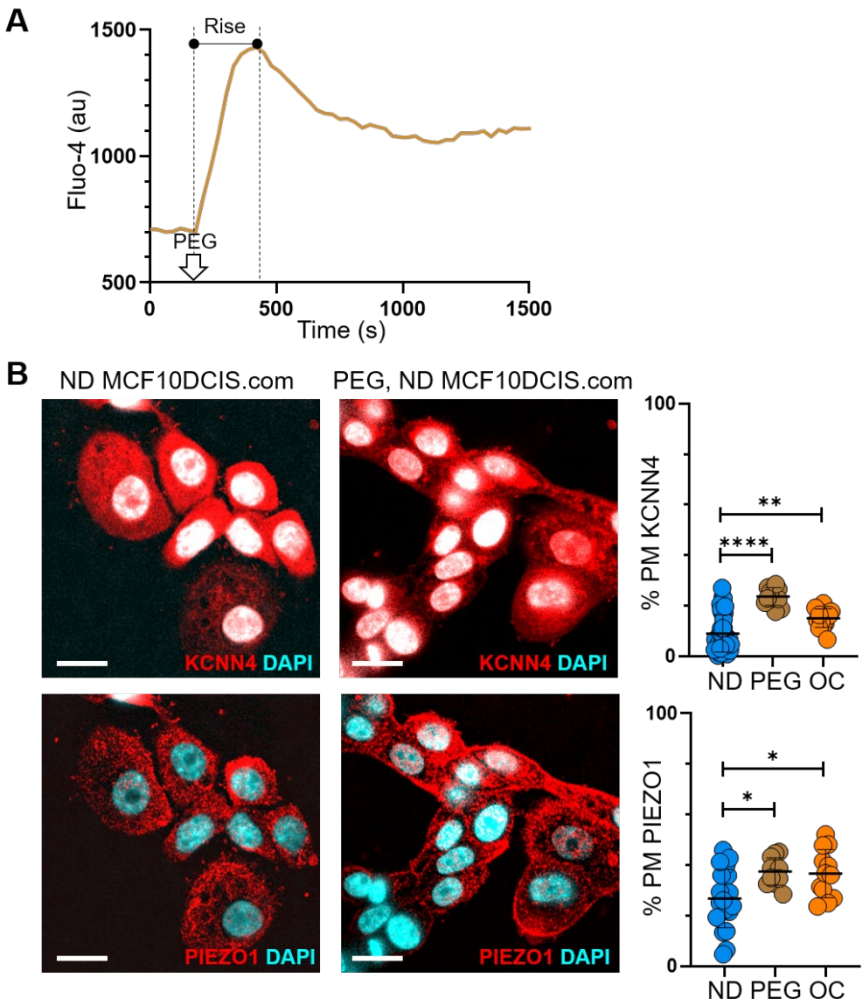

Supplementary Figure 14. Hyperosmotic stress also induces plasma membrane relocation of ion channels, similar to cell crowding. (A) Using the Fluo-4 assay, we observed an initial calcium spike (marked as "Rise") in ND MCF10DCIS.com cells in response to 74.4 mOsmol/kg PEG 300, due to osmotic water outflow. This was followed by a homeostatic relaxation, aimed at restoring calcium levels, which likely involved the inhibition of ion channels like TRPV4, leading to their plasma membrane relocation. Scale bars = 20 μm. **(B)** The same hyperosmotic condition (74.4 mOsm/Kg PEG 300 for 15 min) led to the relocation of KCNN4 and PIEZO1 to the plasma membrane, similar to the relocations observed under OC conditions. Line analysis results showed

the relative relocations of each channel in response to hyperosmotic (PEG) and cell crowding (OC) stresses, compared to ND conditions.

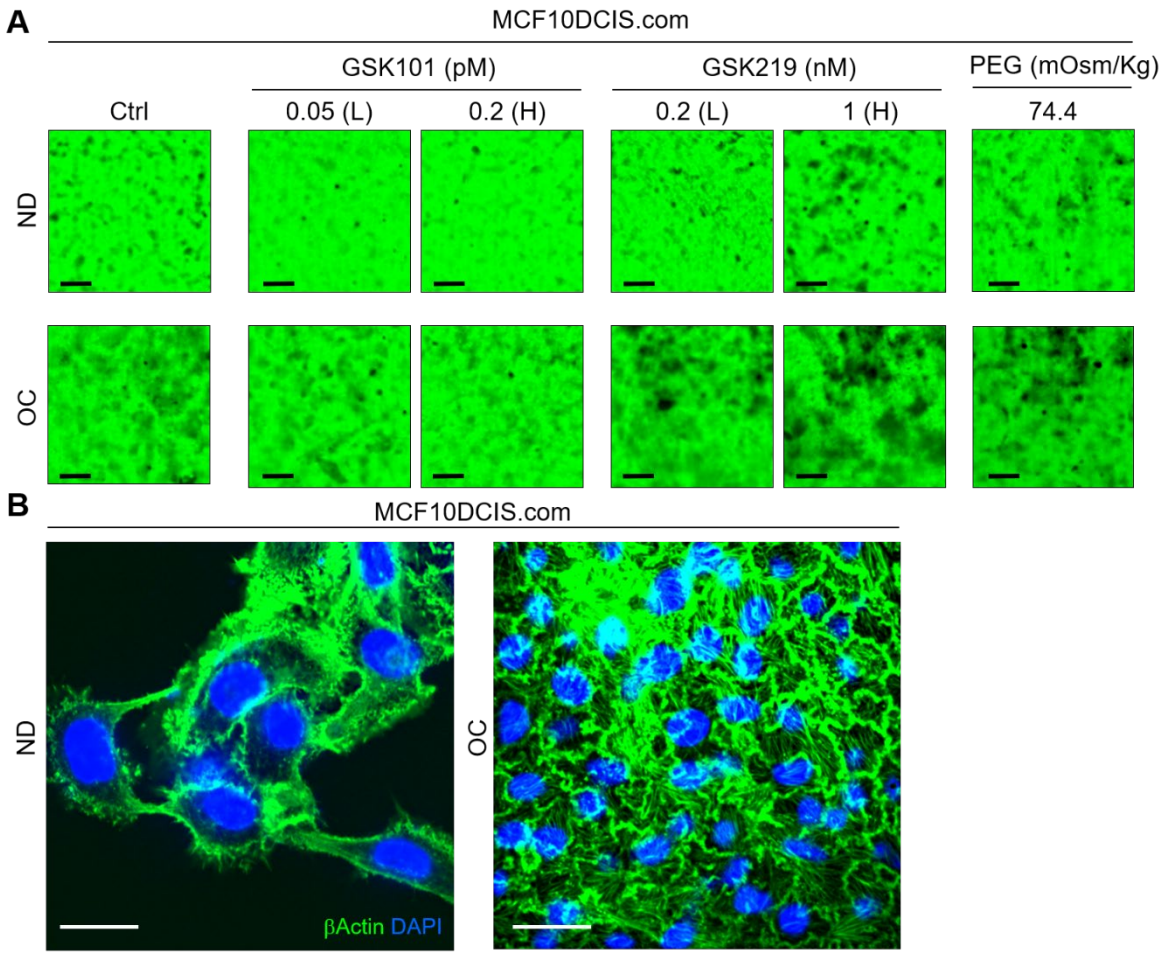

Supplementary Figure 15. Mechanical stresses and TRPV4 activation status affect MCF10DCIS.com cell invasiveness. (A) The effects of 2 days of treatment with GSK101 (0.05 and 0.2 pM), GSK219 (0.2 and 1 nM), and PEG 300 (74.4 mOsm/kg) on the invasiveness of MCF10DCIS.com cells under ND and OC conditions. Gelatin488 images demonstrated the dose-dependent negative effects of GSK101 and positive effects of GSK219 on cell invasiveness. Similar to GSK219, PEG 300 also increased cell invasiveness. Scale bar = 100 μm. **(B)** IF images of βactin (green) and DAPI (blue) in MCF10DCIS.com cells under ND (left) and OC (right) conditions. Strong stress fiber formation was observed in OC cells, while it was absent in ND cells, which was reflected by the increased stiffness of OC cells (**Fig. 2C**). This suggests that cell crowding may enhance cell motility. Scale bar = 20 μm.

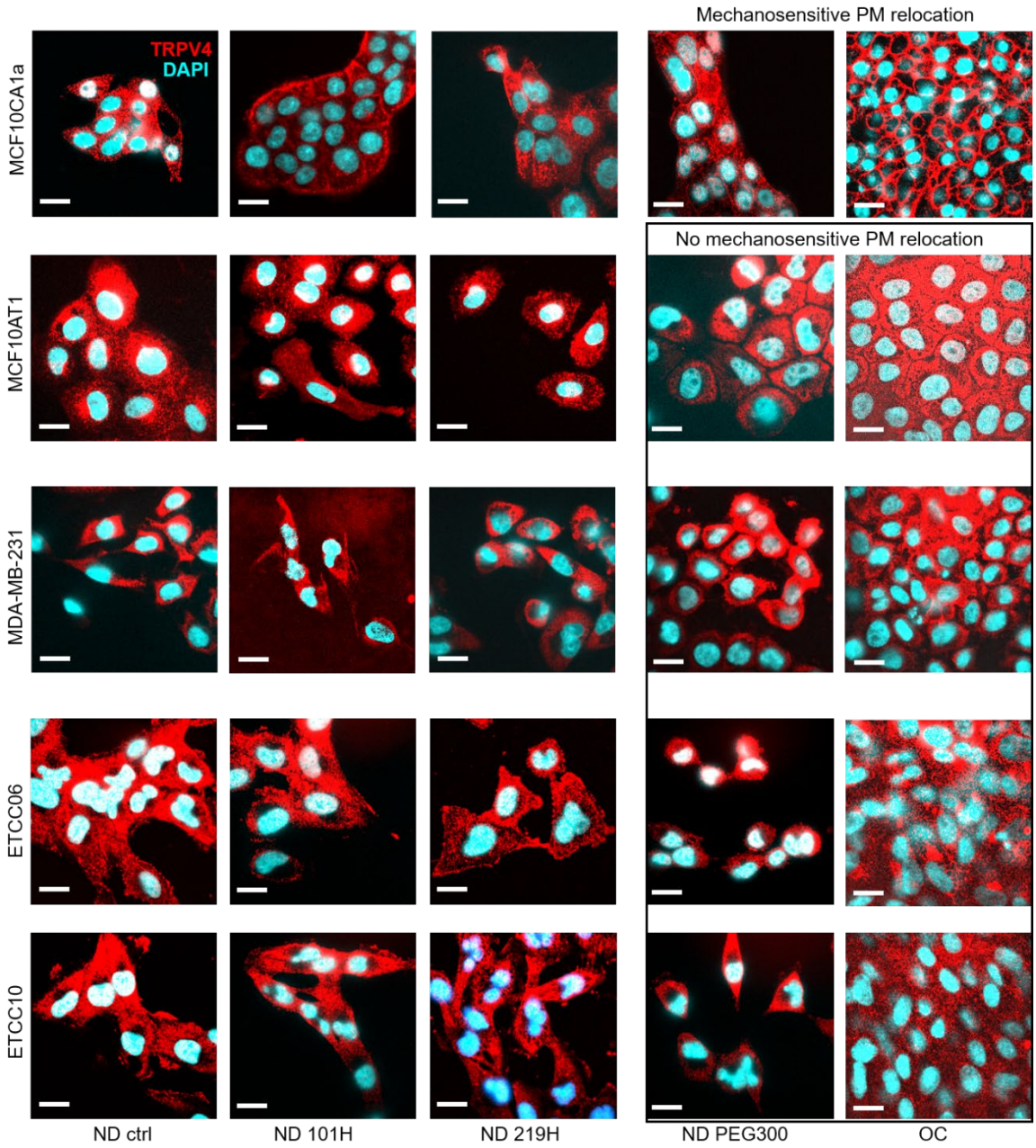

Supplementary Figure 16. Cells lacking the capability for activating pro-invasive mechanotransduction pathway via TRPV4 inhibition-induced cell volume reduction do not relocate TRPV4 to the plasma membrane under TRPV4 inhibition and mechanical stresses. The effects of 2 days of treatment with GSK101 (0.2 pM), GSK219 (1 nM), and PEG 300 (74.4 mOsm/kg) on cells under ND or OC conditions revealed differences in TRPV4 localization (red) in the immunofluorescence (IF) images (cyan: DAPI). Only MCF10CA1a cells show GSK219,

PEG 300, and OC-induced TRPV4 relocation to the plasma membrane. Other cell types, including MCF10AT1, MDA-MB-231, ETCC-06, and ETCC-10, did not exhibit this translocation. Scale bar = 20 μm.